LIGHT NON-AQUEOUS PHASE LIQUID MIGRATION IN FROZEN HETEROGENEOUS POROUS MEDIA

LE MOUVEMENT DE LIQUIDE NON AQUEUX LÉGER DANS LES MILIEUX POREUX HÉTÉROGÈNES GELÉS

A Thesis Submitted to the Division of Graduate Studies
of the Royal Military College of Canada
by

Alex L.Lefebvre
Major

In Partial Fulfillment of the Requirements for the Degree of
Master of Applied Science

August, 2022

For my partner, friends, and family

ACKNOWLEDGEMENT

I'd like to thank both my supervisors, Dr. Ryley Beddoe and Dr. Kevin Mumford, for their mentorship throughout my research. Your interest in my research subject and your enthusiasm towards my experimental results was a real source of motivation. You both are highly competent in what you do, and you inspire others with your professionalism, critical thinking, and meticulous work. I am proud of the work presented in this thesis. It would not be the quality that it is today without your continued help and support.

I'd like to also thank Marina Sergina and Kristine Mattson for your assistance in the lab. Finally, a special thanks to Madeline Calvert for all of the valuable time you spent helping me set myself up at the beginning of my research as well as your assistance in assembling my 3D printed sand packs.

ABSTRACT

Permafrost strongly affects the movement, storage, and exchange of surface and subsurface fluids, including light non-aqueous phase liquids (LNAPLs), which once released into the subsurface pose significant risks to ecosystems and human health. Moreover, climate warming is expected to modify permafrost conditions, which will, in turn, affect LNAPL migration. Laboratory studies are required to investigate LNAPL migration in freezing and frozen soils to protect the environment in a changing climate. Previous laboratory studies mainly focused on the isolated effects of pore ice and freezing temperatures on LNAPL migration by spilling into frozen homogeneous soils. In an attempt to reproduce field conditions, a series of intermediate-scale laboratory experiments were conducted to investigate LNAPL dynamics in the presence of heterogeneity in geology and water/ice contents. The light transmission method (LTM), traditionally used in unfrozen soils, was adapted for use in frozen soils and was used to track LNAPL spills in sand packs with various degrees of heterogeneity in both unfrozen and frozen conditions.

Results demonstrated that while LNAPL's response to heterogeneity in frozen soils differ in comparison to unfrozen soils, heterogeneity remains a critical component for accurate predictions of the extent of a spill. Engineers working to remediate LNAPL spills in frozen conditions should perform a detailed soil characterization to locate heterogeneities in both grain size and distribution as well as ice contents. In the experiments conducted in this study, LNAPL was very sensitive to such ground features and results suggest that the heterogeneity effect seen in unfrozen soils may be enhanced in frozen soils at high ice saturation, including thin layers of fine grains which may become impermeable once frozen. Moreover, in addition to buoyancy and capillary forces, viscous forces need to be considered when it comes to LNAPL migration in frozen soils. Spills in these experiments were observed to migrate as wider masses in frozen conditions in comparison to unfrozen soils, including in zones of residual ice saturation. LNAPL penetration rates also diminished in frozen soils, which was attributed to an increase in the LNAPL viscosity at low temperatures as well as partial blockage of pore space by ice causing LNAPL to spread laterally. Unlike in unfrozen conditions, when LNAPL reached the top of the frozen capillary fringe, it was completely contained above the ice. Finally, the permafrost table should not automatically be associated to impermeable barriers to LNAPL migration since it describes the thermal behaviour of the ground rather than the freeze-thaw state of water and ice. Results demonstrated that only layers of high ice saturation may completely block LNAPL vertical migration. Combining findings from this research as well as knowledge acquired in previous studies, a new conceptual model for LNAPL migration in frozen soils is proposed at the end of this study.

RESUME

Le pergélisol affecte fortement le mouvement, l’accumulation et l'échange des fluides de surface et souterrains, y compris les liquides non aqueux légers (LNAL), qui, une fois rejetés dans le sol, posent des risques importants pour les écosystèmes et la santé humaine. De plus, on estime que le réchauffement climatique va modifier les conditions du pergélisol, ce qui, à son tour, affectera la migration des LNALs. Des études en laboratoire sont nécessaires pour étudier la migration des LNALs dans les sols gelant et gelés afin de protéger l'environnement dans un climat changeant. Les études antérieures en laboratoire se sont principalement concentrées sur les effets isolés de la glace remplissant les pores et des températures de congélation sur la migration des LNALs par des déversements dans des sols homogènes gelés. Dans une tentative de reproduire les conditions de terrain, une série d'expériences de laboratoire à échelle intermédiaire ont été menées pour étudier les dynamiques des LNALs en présence d'hétérogénéité dans la géologie et les contenus d’eau ou de glace. La méthode de transmission de la lumière (MTL), traditionnellement utilisée dans les sols non gelés, a été adaptée pour une utilisation dans les sols gelés et a été utilisée pour étudier la migration de LNALs dans des couches de sable avec divers degrés d'hétérogénéité dans des conditions non gelées et gelées.

Les résultats ont démontré que même si la réponse des LNALs à l'hétérogénéité dans les sols gelés diffère de celle des sols non gelés, l'hétérogénéité reste un élément essentiel pour des prédictions précises de l'étendue d'un déversement. Les ingénieurs travaillant à remédier aux déversements de LNALs dans des conditions de gel doivent effectuer une caractérisation détaillée du sol pour localiser les hétérogénéités dans la taille et la distribution des grains ainsi que dans la teneur en glace. Dans les expériences menées dans cette étude, les LNALs étaient très sensibles à ces caractéristiques du sol et les résultats suggèrent que l'effet d'hétérogénéité observé dans les sols non gelés peut être intensifié dans les sols gelés à saturation de glace élevée, incluant les fines couches de grains fins qui peuvent devenir imperméables une fois gelés. De plus, en plus des forces capillaires et de flottabilité, les forces visqueuses doivent être prises en compte lorsqu'il s'agit de la migration des LNALs dans les sols gelés. En effet, les déversements dans ces expériences ont migré sous forme de masses plus larges dans des conditions gelées par rapport aux sols non gelés, y compris dans les zones de saturation résiduelle de glace. Les taux de pénétration du LNAL ont également diminué dans les sols gelés, ce qui a été attribué à une augmentation de la viscosité du LNAL à basse température ainsi qu'au blocage partiel de l'espace poreux par la glace, provoquant la propagation latérale du LNAL. Contrairement aux conditions non gelées, lorsque les LNALs ont atteint le sommet de la zone capillaire gelée, elles étaient complètement contenues au-dessus de la glace. Engin, la limite du pergélisol ne devrait pas être automatiquement associée à des barrières imperméables à la migration des LNALs puisqu'elle décrit le comportement thermique du sol plutôt que l'état de gel-dégel de l'eau et de la glace. Les résultats ont démontré que seules les couches de saturation élevée en glace peuvent complètement bloquer la migration verticale des LNALs. Combinant les résultats de cette recherche ainsi que les connaissances acquises dans des études antérieures, un nouveau modèle conceptuel pour la migration des LNALs dans les sols gelés est proposé à la fin de cette étude.

CO-AUTHORSHIP STATEMENT

This thesis document is written in an article-based format as laid out in the Royal Military College of Canada Thesis Preparation Guidelines, dated May 2015. The author of this thesis document, Alex L.Lefebvre, was the main author for both articles contained within this document; however, R. Beddoe and K.G. Mumford provided guidance and feedback throughout the writing process. As the author plans to submit both articles contained in this document for publication in peer-reviewed journals, each individual article will have both supervisors noted as co-authors.

TABLE OF CONTENT

CHAPTER 1 INTRODUCTION 1
1.1 Fluids in Permafrost 1
1.2 LNAPL 3
1.2.1 Overview 3
1.2.2 LNAPL Migration in Unfrozen Soils 3
1.2.3 LNAPL Contamination 5
1.3 LNAPL in Permafrost 6
1.3.1 Fuel Spills in the Canadian Arctic 6
1.3.2 LNAPL Migration in Frozen Soils 8
1.3.2.1 LNAPL Experiments in Frozen Homogeneous Soils 8
1.3.2.2 LNAPL Experiments in Frozen Heterogeneous Soils 9
1.4 Research Needs and Objectives 9
1.5 Thesis Organization 10
1.6 References 11
CHAPTER 2 ICE QUANTIFICATION USING THE LTM 14
2.1 Introduction 14
2.2 Methodology 15
2.2.1 Light Transmission Method 15
2.2.2 Experimental Set-up 18
2.2.3 Sand Packing 19
2.2.4 Unfrozen and Frozen Experiments 20
2.2.5 Targeted Saturation and Image Capture 20
2.2.6 Image Processing 21
2.3 Results and Discussion 21
2.3.1 Captured Images 21
2.3.2 Calibration 23
2.3.3 Validation of S-I/I_s Relationships 24
2.3.4 Saturation Maps and Profiles 26
2.4 Conclusion 28
2.5 References 29
CHAPTER 3 LNAPL SPILL IN FROZEN HETEROGENEOUS POROUS MEDIA 32
3.1 Introduction 32
3.2 Methodology 36

3.2.1 Experimental Set-Up 36
3.2.2 Sand Packing 38
3.2.3 Unfrozen and Frozen Experiments 40
3.2.4 Initial Water Conditions 40
3.2.5 Chosen LNAPL, Spill and Tracking 41
3.2.6 Image Processing 42
3.3 Results and Discussion 43
3.3.1 Captured Images 43
3.3.2 LNAPL Distribution during Migration 44
3.3.3 Depth and Width of LNAPL Migration 48
3.3.4 Observation of Halo in Frozen Tests 51
3.3.5 Towards an Improved Conceptual Model of LNAPL Migration in Frozen Soil 53
3.4 Summary and Conclusions 54
3.5 References 56
CHAPTER 4 CONCLUSION AND RECOMMENDATIONS 60
4.1 Conclusion 60
4.2 Recommendations 61
APPENDICES 64
Appendix A: 64
A.1 Precision / Resolution Analysis 64
Appendix B 66
Appendix C 72
Appendix D 75
Appendix E 76
Appendix F 77
Appendix G 85
Appendix H 91
Appendix I 92
Appendix J 93
Appendix K 94
Appendix L 97

LIST OF TABLES

TABLE 2.1: List of tests and their respective captured water positions in the cell. U and F stands for unfrozen and frozen respectively. U1, U2 and U4 were also performed in frozen conditions (referred to as F1, F2, and F4 respectively). 22

TABLE 2.2: Test U3 known and calculated water volumes in the cell. 23

TABLE 3.1: List of tests performed in both unfrozen and frozen conditions including sand mixtures and packing configurations. 39

TABLE 3.2: Hue* ranges used per test to extract spill coordinates from selected images. 43

TABLE C.1: Test U1 known and calculated water volumes in the cell. 72

TABLE C.2: Test U2 known and calculated water volumes in the cell. 72

TABLE C.3: Test U3 known and calculated water volumes in the cell. 72

TABLE C.4: Test U4 known and calculated water volumes in the cell. 73

TABLE C.5: Test U5 known and calculated water volumes in the cell. 73

TABLE C.6: Test F1 known and calculated ice volumes in the cell. 73

TABLE C.7: Test F2 known and calculated ice volumes in the cell. 73

TABLE C.8: Test F4 known and calculated ice volumes in the cell. 74

LIST OF FIGURES

FIGURE 1.1: Definition of permafrost and associated features (modified after Woo, 2012). 1

FIGURE 1.2: Predicted changes in hydrogeologic conditions due to thaw in discontinuous permafrost for (a) present climate and (b) warmer climate. For the warmer climate (b), existing closed taliks may become open, facilitating groundwater (GW) movement to subpermafrost aquifers and thereby drain lakes (left). Increased recharge and enhanced GW discharge through newly activated aquifers can lead to expanding lakes or river (right) (Walvoord and Kurylyk, 2016). 2

FIGURE 1.3: A cartoon of an air-LNAPL-water system in porous media showing free LNAPL (light pink color), entrapped LNAPL (dark pink color) and residual LNAPL (red color), which consist of continuous thin LNAPL films and relatively immobile LNAPL in wedges, with mobile (light blue) and residual water (dark blue) (Mumford et al., 2022). 5

FIGURE 1.4: Contaminated sites in Northwest Territories, Canada (Explore North, 2006). 7

FIGURE 1.5: Abandoned cache sites on Ellesmere Island, Nunavut (Nadeau, 2019)..... 7

FIGURE 2.1: Experimental set-up showing the (a) light transmission and data acquisition system and (b) example of a light transmission image. 17

FIGURE 2.2: Flow cell image showing the cell frame, glass panels, bottom ports, and flexible transparent tubes. Each port is topped with a water-wet net filter. 19

FIGURE 2.3: Example of light transmission images from test U3 prior to image processing showing (a) saturated conditions followed by unsaturated conditions with water positions at approximately (b) 75 %, (c) 50 %, and (d) 25 % of the cell height, as well as (e) residual saturation and (f) following water imbibition to create trapped gas. 22

FIGURE 2.4: Calculated versus known volumes of water and ice in the cell from all tests..... 24

FIGURE 2.5: Relationship between *I/Is* and *S* for both unfrozen and frozen experiments with trapped gas images from tests U1, U3 and U4..... 25

FIGURE 2.6: Water distribution in two zones of interest (dashed rectangles) in both unfrozen (U4) and frozen (F4) conditions shown as (a) unfrozen grayscale image, (b) unfrozen saturation map, (c) frozen grayscale image, (d) frozen saturation map. 26

FIGURE 2.7: Intensity and saturation profiles versus height showing both unfrozen and frozen (a) residual saturation intensities, (b) 100 % saturation intensities, (c) evaluated images intensities, (d) evaluated images saturations. 27

FIGURE 3.1: Conceptual model of water circulation in permafrost conditions, modified after Woo (2012)..... 32

FIGURE 3.2: Conceptual model of LNAPL release in the subsurface in unfrozen conditions from Rivett et al. (2014). 33

FIGURE 3.3: Light transmission experimental set-up including data acquisition system..... 37

FIGURE 3.4: Flow cell details showing a heterogeneous sand pack. 38
FIGURE 3.5: Flow cell set-up and sand pack configurations: (a) homogeneous sand pack (H3040), (b) heterogeneous cross-bedded sand packs (CB3040 and CB4070), and (c) spill tube set-up. 39
FIGURE 3.6: Initial water or ice saturation conditions (pre-spill) for each pack configuration in unfrozen conditions (a) H3040U, (b) CB3040U and (c) CB4070U as well as in frozen conditions (d) H3040F, (e) CB3040F, (f) CB4070F. 42
FIGURE 3.7: Test CB4070U images tracking spill progression in space at (a) 10 sec, (b) 41 sec, (c) 3 min, (d) 9 min, (e) 21 min, (f) 50 min, (g) 2 h 41 min, (h) 4 h 18 min and (i) 2 d 5 h 20 min. 44
FIGURE 3.8: Spill progression map in space and time for all tests (a) H3040U, (b) CB3040U, (c) CB4070U, (d) H3040F, (e) CB3040F and (f) CB4070F. 46
FIGURE 3.9: Depth versus time for all spills with (a) final spill image in CB4070F showing the position of the capillary barriers in the cell, which are extended in (b) the depth versus time for CB4070F and (c) the depth versus time for all six tests. 49
FIGURE 3.10: Width versus time for all spills with (a) an image from the spill in CB4070U to define total and maximum width, (b) total width versus time for all tests, (c) maximum width versus time for all tests and (d) depth versus maximum width for all tests. 50
FIGURE 3.11: Difference between back lit (left side) and front lit (right side) images. 52
FIGURE 3.12: Conceptual model for LNAPL migration in (a) temperate region terrain and (b) permafrost terrain. 53
FIGURE A.1: Standard deviation versus block size. 64
FIGURE A.2: Resolution resulting from the four following different block sizes (a) 0.35 mm, (b) 1 mm (c) 5 mm, and (d) 10 mm. 65
FIGURE B.1: Example of light transmission images from test U1 prior to image processing showing (a) saturated conditions followed by unsaturated conditions with water positions at approximately (b) 75 %, (c) 50 %, and (d) 25 % of the cell height, as well as (e) residual saturation and (f) following water imbibition to create trapped gas. 66
FIGURE B.2: Example of light transmission images from test F1 prior to image processing showing unsaturated conditions with water positions at approximately (a) 75 %, (b) 50 %, and (c) 25 % of the cell height, as well as (d) residual saturation. 67
FIGURE B.3: Example of light transmission images from test U2 prior to image processing showing (a) saturated conditions followed by unsaturated conditions with water positions at approximately (b) 75 %, and (c) 50 % of the cell height, as well as (d) residual saturation. 68
FIGURE B.4: Example of light transmission images from test F2 prior to image processing showing unsaturated conditions with water positions at approximately (a) 75 %, and (b) 50 % of the cell height, as well as (c) residual saturation. 68
FIGURE B.5: Example of light transmission images from test U3 prior to image processing showing (a) saturated conditions followed by unsaturated conditions with

water positions at approximately (b) 75 %, (c) 50 %, and (d) 25 % of the cell height, as well as (e) residual saturation and (f) following water imbibition to create trapped gas. 69

FIGURE B.6: Example of light transmission images from test U4 prior to image processing showing (a) saturated conditions followed by unsaturated conditions with water positions at approximately (b) 75 %, (c) 50 %, (d) 40 %, and (e) 25 % of the cell height, as well as (f) residual saturation and (g) following water imbibition to create trapped gas. 70

FIGURE B.7: Example of light transmission images from test F4 prior to image processing showing unsaturated conditions with water positions at approximately (a) 75 %, (b) 50 %, (c) 40 %, and (d) 25 % of the cell height, as well as (e) residual saturation. 70

FIGURE B.8: Example of light transmission images from test U5 prior to image processing showing (a) saturated conditions followed by unsaturated conditions with water positions at approximately (b) 75 %, (c) 50 %, and (d) 25 % of the cell height, as well as (e) residual saturation. 71

FIGURE D.1: Freezing cell images in the following conditions (a) unfrozen, (b) partially frozen, (c) partially frozen, (d) partially frozen, (e) partially frozen, and (f) frozen. 75

FIGURE E.1: (a) z vs I and (b) z vs S profiles using measured I_r/I_s for test U4. 76

FIGURE F.1: Saturation profile versus height for test U1. 77

FIGURE F.2: Saturation profile versus height for test U2. 78

FIGURE F.3: Saturation profile versus height for test U3. 79

FIGURE F.4: Saturation profile versus height for test U4. 80

FIGURE F.5: Saturation profile versus height for test U5. 81

FIGURE F.6: Saturation profile versus height for test F1. 82

FIGURE F.7: Saturation profile versus height for test F2. 83

FIGURE F.8: Saturation profile versus height for test F4. 84

FIGURE G.1: H3040U spill progression in space at (a) 10 sec, (b) 40 sec, (c) 3 min, (d) 9 min, (e) 21 min, (f) 50 min, (g) 2 h 43 min, (h) 4 h 19 min and (i) 1 d 4 h 34 min. ... 85

FIGURE G.2: CB3040U spill progression in space at (a) 10 sec, (b) 41 sec, (c) 3 min, (d) 9 min, (e) 21 min, (f) 50 min, (g) 2 h 42 min, (h) 4 h 18 min and (i) 2 d 5 h 24 min. 86

FIGURE G.3: CB4070U spill progression in space at (a) 10 sec, (b) 41 sec, (c) 3 min, (d) 9 min, (e) 21 min, (f) 50 min, (g) 2 h 41 min, (h) 4 h 18 min and (i) 2 d 5 h 20 min. 87

FIGURE G.4: H3040F spill progression in space at (a) 11 sec, (b) 41 sec, (c) 3 min, (d) 9 min, (e) 24 min, (f) 49 min, (g) 2 h 40 min, (h) 4 h 21 min and (i) 2 d 5 h 17 min. ... 88

FIGURE G.5: CB3040F spill progression in space at (a) 10 sec, (b) 44 sec, (c) 3 min, (d) 9 89

min, (e) 21 min, (f) 50 min, (g) 2 h 43 min, (h) 4 h 19 min and (i) 1 d 19 h 56 min. 89

FIGURE G.6: CB4070F spill progression in space at (a) 10 sec, (b) 39 sec, (c) 3 min, (d) 9 min, (e) 21 min, (f) 43 min, (g) 2 h 41 min, (h) 4 h 18 min and (i) 2 d 5 h 19 min.... 90

FIGURE H.1: Halo in frozen spills for packs (a) H3040F, (b) CB3040F and (c) CB4070F respectively. 91

FIGURE H.2: Example of a spill image in H3040F where (a) a column was selected for an intensity analysis in (b) unfrozen conditions pre-spill, frozen conditions pre-spill, frozen conditions during the spill and in thawed conditions post spill. 91

FIGURE I.1: Fully saturated packs before water drainage (pre-spill) for test in the a) H3040U, (b) CB3040U, (c) CB4070U, (d) H3040F, (e) CB3040F and (f) CB4070F pack. 92

FIGURE J.1: Water imbibition post spills in the a) H3040U, (b) CB3040U, (c) CB4070U, (d) H3040F, (e) CB3040F and (f) CB4070F pack..... 93

FIGURE K.1: Macro pictures showing various zones with different degrees of heterogeneity in grain size and water content..... 94

FIGURE K.2: Macro picture of LNAPL spill in CB4070F. 95

FIGURE K.3: Macro pictures showing LNAPL spill in CB3040F..... 96

FIGURE L.1: Experimental set-up outside the freezer without the covering curtains..... 97

FIGURE L.2: Experimental set-up placed outside of the freezer with the covering curtains. 97

FIGURE L.3: Experimental set-up placed inside the freezer..... 98

FIGURE L.4: Freezer used for the experiments. 99

LIST OF SYMBOLS AND ABBREVIATIONS

Symbols and Abbreviations	Definitions
2D	Two-dimensional
ASTM	American Society for Testing and Materials
C	Optical geometric term, which corrects for the position of emitted and captured light
CB3040	Cross-bedded distribution with 20-30 + 30-40 mixture
CB3040F	Cross-bedded distribution with 20-30 + 30-40 mixture frozen
CB3040U	Cross-bedded distribution with 20-30 + 30-40 mixture unfrozen
CB4070	Cross-bedded distribution with 20-30 + 40-70 mixture
CB4070F	Cross-bedded distribution with 20-30 + 40-70 mixture frozen
CB4070U	Cross-bedded distribution with 20-30 + 40-70 mixture unfrozen
CFS Alert	Canadian Forces Station Alert
cm	Centimeter
cm^3	Centimeter cube
CO_2	Carbon Dioxide
d_{50}	Particle diameter
D_{60}/d_{10}	Uniformity coefficient
dia	Diameter
d_p	Thickness of a grain
EFS	Electro-focus short back focus
Eq.	Equation
F	Frozen
F1	Test # 1 Frozen
F2	Test # 2 Frozen
F4	Test # 4 Frozen
g	Gram
g (subscript)	Gas
h	Hour
H3040	Homogeneous distribution with 20-30 + 30-40 mixture
H3040F	Homogeneous distribution with 20-30 + 30-40 mixture frozen
H3040U	Homogeneous distribution with 20-30 + 30-40 mixture unfrozen
HSV	Hue-Saturation-Value color system
I	Transmitted light intensity
i (subscript)	Ice
I_0	Light source intensity

I_d	Light intensity through dry sand
I_n	Normalized light intensity
I_r	Light intensity through sand at residual saturation
I_s	Light intensity through saturated sand
ISO	International Organization for Standardization (Camera's sensitivity to light)
l	Liter
l (subscript)	Liquid
k	Number of particles or pores across the medium thickness
LED	Light emitting diode
LNAPL	Light non-aqueous phase liquid
LTM	Light transmission method
Mg	Mega gram
min	Minute
ml	Milliliter
mm	Millimeter
mm^2	Millimeter square
m^3	Meter cube
NAPL	Non-aqueous phase liquid
p (subscript)	Particle (grain)
PHCs	Petroleum hydrocarbons
RGB	Red-Green-Blue color system
RMC	Royal Military College
S	Degree of saturation
s	Second
S_e	Effective saturation
S_r	Residual saturation
S_w	Water saturation
TG	Trapped gas
U	Unfrozen
U1	Test # 1 Unfrozen
U2	Test # 2 Unfrozen
U3	Test # 3 Unfrozen
U4	Test # 4 Unfrozen
U5	Test # 5 Unfrozen
α_p	Absorbance coefficient of a grain
τ	Average transmittance of an interface
μm	micrometer
^oC	Degree Celsius

CHAPTER 1 INTRODUCTION

1.1 Fluids in Permafrost

Permafrost is ground that is at or below 0 °C for at least two consecutive years. It used to be conceived as perennially frozen ground (Muller, 1943), but the permafrost definition is currently based on temperature and not the freeze-thaw state of water in the host medium (Woo, 2012). The top boundary of permafrost is called the permafrost table, which can be as shallow as tens of centimeters or as deep as several meters from the ground surface (Walvoord and Kurylyk, 2016). The bottom boundary of permafrost is called the permafrost base and can be several meters to 10^3 m deep (Walvoord and Kurylyk, 2016). The active layer is the seasonally thawed surface layer of the ground in a permafrost area. Several factors may lead to a freezing point depression of water (i.e., solutes concentration), therefore, it is possible for the active layer to extend below the permafrost table (Figure 1.1) (Woo, 2012; Walvoord and Kurylyk, 2016). Furthermore, unfrozen zones, referred to as taliks, can also exist within permafrost (i.e., below water bodies due to the high heat capacity of water) (Walvoord and Kurylyk, 2016).

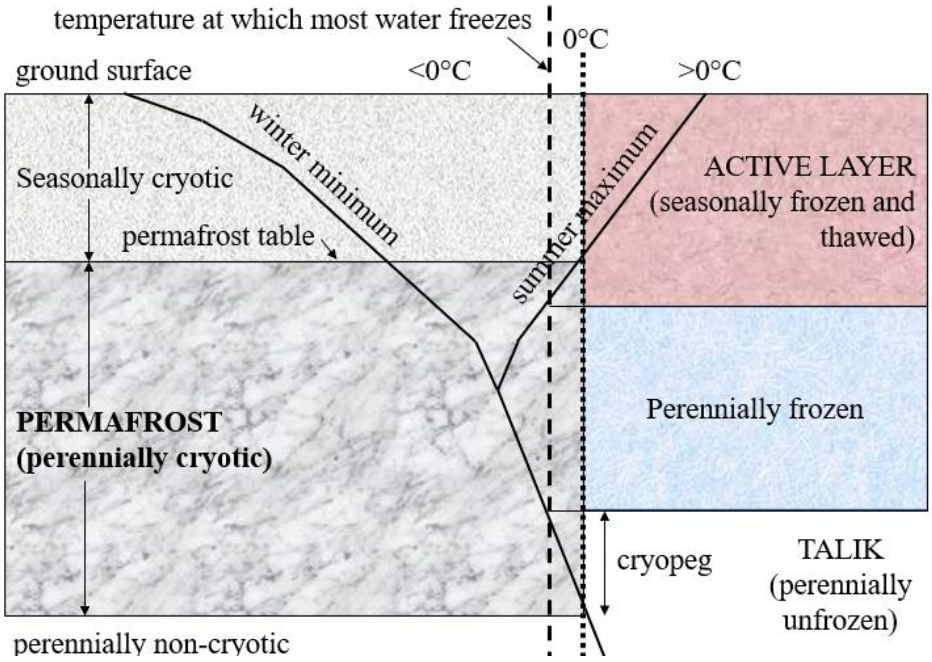

FIGURE 1.1: Definition of permafrost and associated features (modified after Woo, 2012).

Because the transition from unfrozen to frozen coincides with a considerable reduction in hydraulic conductivity for saturated porous media, frozen ground is often conceptualized as an impermeable barrier preventing infiltration, however, unsaturated frozen and partially frozen ground may allow for considerable flow through macropores (Walvoord and Kurylyk, 2016). Such variations in hydraulic conductivity in permafrost terrain strongly affects the movement, storage, and exchange of surface and subsurface water (Walvoord and Kurylyk, 2016). In turn, subsurface flow can affect permafrost distribution by increasing the transfer of thermal energy via heat

advection (de Grandpré et al., 2012; Sjöberg et al., 2016; Walvoord and Kurylyk, 2016). This interplay, along with physical, chemical, and biogeochemical processes, creates complex, and often nonintuitive, dynamics in permafrost regions (Walvoord and Kurylyk, 2016). Furthermore, groundwater dynamics in permafrost are expected to change as a result of climate warming. Climate warming is expected to modify the permafrost distribution, leading to changing hydrologic conditions, including variations in soil moisture, connectivity of inland waters (i.e., taliks), streamflow seasonality, and the partitioning of surface and subsurface water (Figure 1.2) (Walvoord and Kurylyk, 2016). To protect water resources and critical infrastructure, it is essential to understand groundwater behaviours in permafrost terrain in a changing climate, which requires multi-disciplinary studies including geotechnical and environmental engineering.

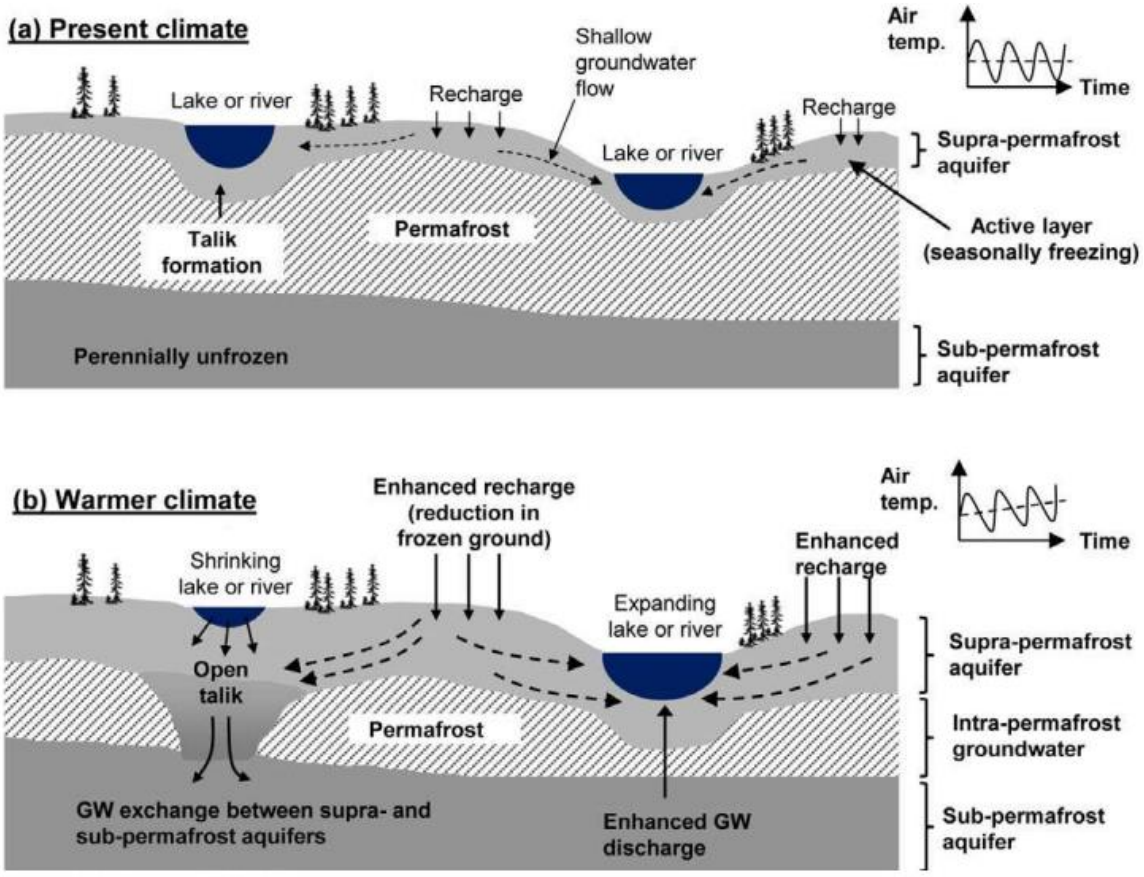

FIGURE 1.2: Predicted changes in hydrogeologic conditions due to thaw in discontinuous permafrost for (a) present climate and (b) warmer climate. For the warmer climate (b), existing closed taliks may become open, facilitating groundwater (GW) movement to subpermafrost aquifers and thereby drain lakes (left). Increased recharge and enhanced GW discharge through newly activated aquifers can lead to expanding lakes or river (right) (Walvoord and Kurylyk, 2016).

In addition to water, other fluids in permafrost terrain behave in a manner not found in temperate soils (soils that do not experience deep freezing) (Barnes and Chuvilin, 2009). The

presence of ice, the influence of seasonal freeze and thaw cycling, and the typically shallow active layers found in permafrost environments all impact the movement of fluids (Barnes and Chuvilin, 2009). This includes light non-aqueous phase liquids (LNAPLs), which include petroleum fuels such as gasoline, diesel, and jet fuel. As a result of climate warming, thaw-activated groundwater flow will open up new transport pathways, leading to alterations in terrestrial-to-aquatic exchanges of nutrients and contaminants (i.e., LNAPLs) and will pose new risks to Arctic water supplies, raising both human and ecosystem health concerns (McKenzie et al., 2021). To understand LNAPL movement through freezing and frozen soils, it is useful to review its fundamental migration principles through unfrozen soil (Barnes and Chuvilin, 2009).

1.2 LNAPL

1.2.1 Overview

A wide range of organic liquids are categorized as LNAPLs. LNAPLs typically comprise a complex mixture of primarily hydrocarbon organic chemicals with a wide range of physical-chemical and toxicological properties (Rivett et al., 2014). In the context of groundwater contamination, LNAPLs are most often associated with petroleum hydrocarbons (PHCs) such as gasoline, diesel fuel, heating oil, jet fuel, kerosene, and feedstock such as crude oil (Mumford et al., 2022). LNAPLs also include organic solvents such as alkanes and aromatics, including benzene and toluene, which can be found as components in fuels and as compounds used in chemical manufacturing (Mumford et al., 2022). LNAPLs are amongst the most frequently encountered organic contaminants in the ground due to their abundant use, accidental release and, perhaps, poor (historical) disposal (Rivett et al., 2014). LNAPL releases can be associated with a variety of storage and fluid transfer infrastructure, including above ground and underground storage tanks and pipelines, as well as fluid handling operations (i.e., manufacturing facilities, refineries, terminals, filling stations, airports, and military bases) (Rivett et al., 2014; Mumford et al., 2022).

1.2.2 LNAPL Migration in Unfrozen Soils

LNAPLs are hydrophobic organic chemicals that are immiscible with water and are less dense than water, hence making LNAPL exist as a separate organic liquid phase (when in contact with water) ‘floating’ upon that aqueous-phase liquid (Rivett et al., 2014). Once released to the subsurface, LNAPL migrates down through the strata as a two-phase flow (LNAPL-air) until it approaches the unsaturated zone above the water table where it becomes a three-phase flow (water-LNAPL-air). Once it reaches the top of the capillary fringe, some LNAPL migrates as a two-phase flow again (water-LNAPL). LNAPL subsurface transport is complex, due to its multi-phase flow nature, but it is often characterised by an accumulation of LNAPL in the vicinity of the water table that can migrate laterally or redistribute vertically due to natural or human-induced water table fluctuations (Rivett et al., 2014).

LNAPL migration is influenced by the size of the release and the fluid’s viscosity (Rivett et al., 2014). Low viscosity LNAPL releases (such as gasoline) may stabilise within weeks to months, whereas high viscosity LNAPLs (such as heating oil or crude oil) may require months to years to stabilise as they flow more slowly for longer periods (Rivett et al., 2014). LNAPL migration is very sensitive to both fluid properties (density, viscosity, solubility, vapour pressure, wettability, and interfacial tension) and porous media properties (porosity, intrinsic permeability, degree of

heterogeneity, and the presence of additional fluids) (Mercer and Cohen, 1990; Poulsen and Kueper, 1992; Newell et al., 1995; Montoro and Francisca, 2013; Mumford et al., 2022). Horizontal bedding in the formation results in lateral spreading and retention at textural interfaces (Kechavarzi et al., 2008). Further, Poulsen and Kueper (1992) reported that an extremely heterogeneous distribution of non-aqueous phase liquids (NAPLs) can result from NAPL migration through sands exhibiting only a moderate spatial variability in permeability and capillary characteristics (i.e., mild heterogeneity). Based on results obtained from a field experiment conducted on an old prograding shoreline deposit, Poulsen and Kueper (1992) noted that NAPL can migrate parallel to soil bedding and that certain laminations may or may not contain stringers of residual NAPL. Accurate predictions of the extent of a NAPL spill in the subsurface therefore rely on proper soil characterization that identifies local heterogeneities in geology.

Assuming that a porous medium is water-wet (water wets the solid surfaces), the wettability increases in the order air < LNAPL < water (Leverett, 1941). Consequently, when all three fluids are present, the smallest pores are occupied by water, the intermediate-size pores are occupied by LNAPL, and the largest pores are occupied by air (Schroth et al., 1998). However, it depends on the accessibility of air-LNAPL and LNAPL-water interfaces to pores (it is not uncommon for larger pores to be surrounded with smaller pores preventing a fluid from entering the larger pores unless the right capillary pressure is obtained to allow the fluid to first enter the smaller pores) (Mumford et al., 2022) (Figure 1.3). This concept is useful for the prediction of LNAPL behaviour in the vicinity of textural interfaces where variability in both permeability and water saturation (S_w) can occur (Schroth et al., 1998). For example, Schroth et al. (1998) demonstrated that LNAPL migrating in a fine-grained soil layer is diverted parallel to an interface with a layer of coarse-grained soil when both layers are at low water saturation (when $S_w \sim 0$, LNAPL is the wetting fluid and occupies the small pores, air is the non-wetting fluid and occupies the large pores, which causes LNAPL to be contained in the fine-grained soil layer). Further, Schroth et al. (1998) demonstrated that LNAPL is also diverted parallel to a textural interface in zones of high water saturation, however, in this case, rather than being diverted along the textural interface, LNAPL diversion occurs in the upper portion of the zone of high water saturation which supports the LNAPL. Schroth et al. (1998) demonstrated that only in zones of moderate water saturation does partial penetration of LNAPL into the coarse-grained layer occur (at the interface, water occupies the small pores and LNAPL is forced to move into larger pores than it previously occupied during vertical downward migration).

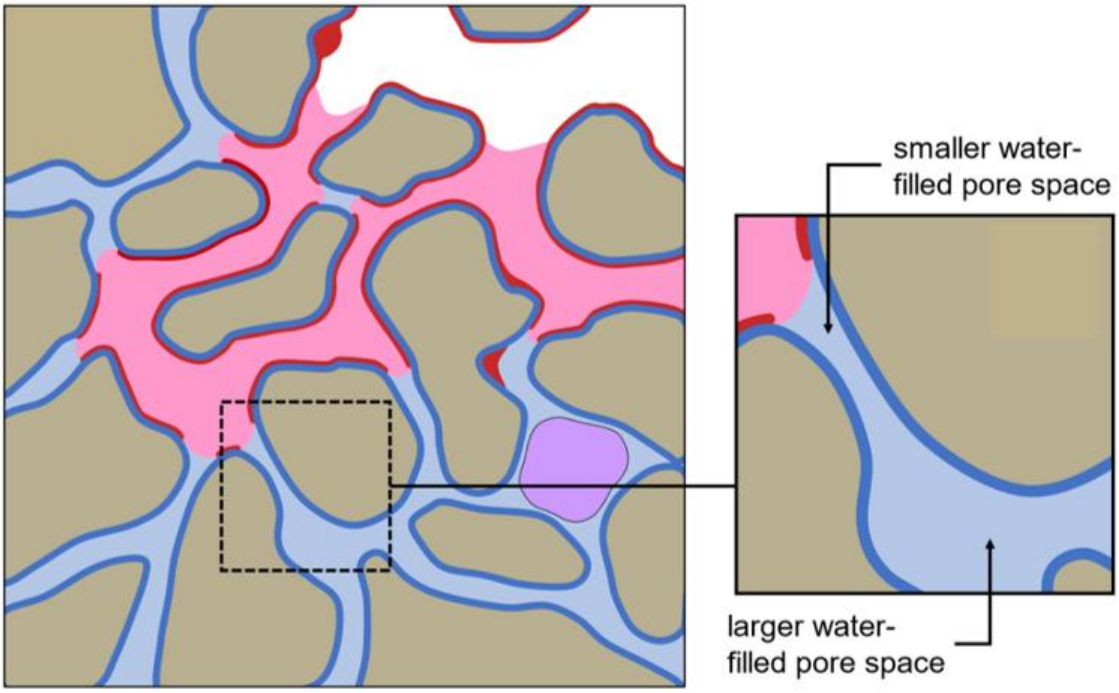

FIGURE 1.3: A cartoon of an air-LNAPL-water system in porous media showing free LNAPL (light pink color), entrapped LNAPL (dark pink color) and residual LNAPL (red color), which consist of continuous thin LNAPL films and relatively immobile LNAPL in wedges, with mobile (light blue) and residual water (dark blue) (Mumford et al., 2022).

1.2.3 LNAPL Contamination

LNAPL spills pose significant environmental risks (Domenico and Schwartz, 1998; Mercer and Cohen, 1990; Pankow and Cherry, 1996; Miller et al., 2004). The migration of LNAPL through the subsurface can affect surface water by creating oil sheens, impacting aquatic organisms, and compromising drinking water supplies (Mumford et al., 2022). Further risks include the partitioning of organic compounds from LNAPL to surrounding groundwater, creating a dissolved-phase plume that can be transported in the direction of groundwater flow towards drinking water wells or surface water (Rivett et al., 2014; Mumford et al., 2022). Natural attenuation processes such as biodegradation can contribute to the mitigation of the contamination (Rivett et al., 2014), however, biogeochemical reactions with the dissolved organic compounds in the plume can further reduce groundwater quality through reduction in dissolved oxygen and changes in metal and sulfur compound speciation (Mumford et al., 2022). In addition, volatile LNAPL constituents can partition from the LNAPL source zone and penetrate receptors at the ground surface (i.e., buildings) and reduce air quality (a process called vapor intrusion) (Rivett et al., 2014; Mumford et al., 2022).

Even when the bulk of a spill is removed, residual LNAPLs in the ground remain a safety concern for groundwater supplies. Despite the low aqueous solubilities of organic compounds found in LNAPLs, their solubilities can still exceed health advisory levels (Ewing and Berkowitz, 1998). Furthermore, the low solubility of LNAPL components contribute to making them long-

term sources of contamination for groundwater supplies. Recent events in Iqaluit provide an example of such long-term water contamination by LNAPLs. An old underground tank from 1962 buried next to the water treatment plant leaked fuel into the city's drinking water distribution system (Aziz, 2022). The city rapidly proceeded to remove the tank; however, despite the fact that the bulk of the fuel (the source) was removed from the site, the city still experienced issues later since residual PHCs in the ground entered the water distribution system again a few months after the initial event. Moreover, a do-not-consume order also went into effect on March 23rd, 2022, in Sachs Harbour, Northwest Territories after the Territory's chief public health officer reported a fuel smell and an oily sheen in water deliveries (cbc.ca, 2022). However, in this case, an oily container confused for a clean one is what left half of Sachs Harbour without usable tap water for a month (Carroll, 2022). Both Iqaluit and Sachs Harbour are located in the continuous permafrost zone, adding additional complexities affecting LNAPL migration. Future remediation plans will benefit from knowledge of the implications of those complexities on LNAPL migration in permafrost terrain.

1.3 LNAPL in Permafrost

1.3.1 Fuel Spills in the Canadian Arctic

There are several LNAPL-contaminated sites in the Canadian Arctic (e.g., Nadeau, 2019; Explore North, 2006). As an example, Figure 1.4 is a map highlighting a subset of contaminated sites in the Northwest Territories alone (Explore North, 2006). Many of those sites have been reported to have elevated levels of hydrocarbons in soil and groundwater. The list includes the old Colomac Mine site, which was heavily contaminated from multiple fuel spill incidents over the years during the mine's operating lifetime from 1989 to 1997 (Nadeau, 2019). It has since undergone an extensive cleanup and has been the location of several research studies on LNAPL migration in permafrost (e.g., Bickerton et al., 2007; Iwakun et al., 2007). In addition, there are arctic Canadian Forces establishments that have been identified as contaminated over the years. Historically, several barrel caches had been put on Ellesmere Island, Nunavut to supply fuel to military occupied sites. Over the years, many of those sites were abandoned, which left fuel barrels and the potential for leakage into the subsurface. For the past 30 years, the Canadian Forces has been relocating these barrels so that they could be safely and properly disposed of. A few barrel caches undergoing remediation as part of Operation Nevus can be seen in Figure 1.5. Operation Nevus is a yearly military operation mainly focused on the maintenance of remote satellite and communication sites carrying communication signals to Canadian Forces Station Alert (CFS Alert), but Operation Nevus also provides opportunities to perform concomitant tasks such as fuel barrel remediation since it brings resources on the ground. However, even though the contaminant source is being removed from the cache sites, the ground remains contaminated as spills were observed at most of the locations.

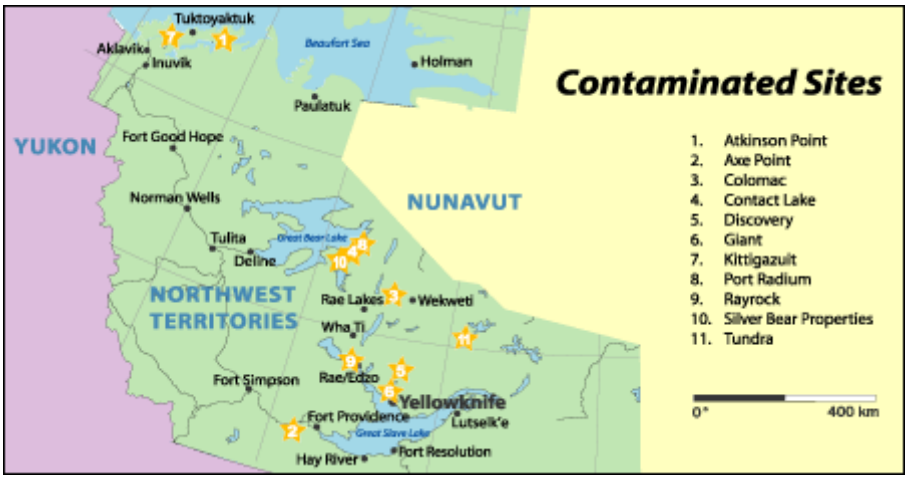

FIGURE 1.4: Contaminated sites in Northwest Territories, Canada (Explore North, 2006).

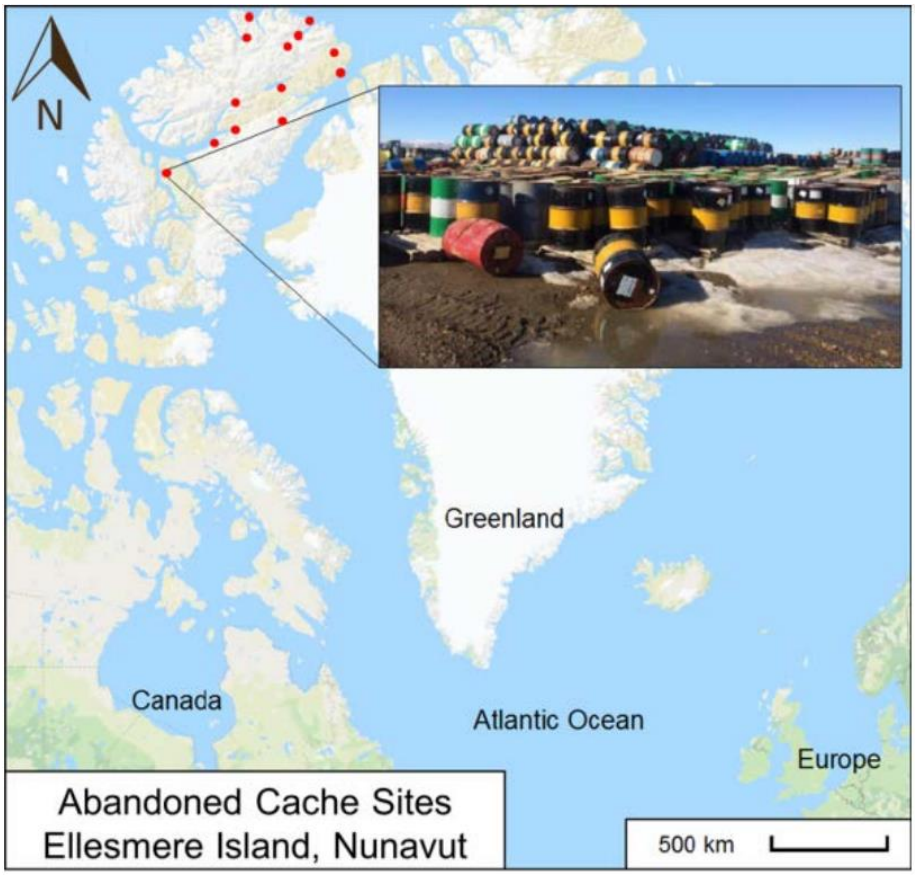

FIGURE 1.5: Abandoned cache sites on Ellesmere Island, Nunavut (Nadeau, 2019).

Today, accidental fuel spills can still occur even with proper preventative measures in place. For example, Biggar et al. (1998) performed a ground contamination assessment on an old tank

farm site at CFS Alert. The construction of the site included a horizontal foundation fill with exterior dikes around three sides of it, topped with a 0.9 mm polyester laminate geomembrane, which was covered with a 30 cm layer of gravel. Despite careful handling during the operational years, and containment barriers at the time of the berm construction, the investigation revealed contamination beneath the berm, as well as below the permafrost table. All past, present, and future anthropogenic activities in the Canadian Artic have risk for fuel spill events, therefore, understanding the migration of LNAPLs in a permafrost environment is important to protect arctic ecosystems and human health.

1.3.2 LNAPL Migration in Frozen Soils

In freezing and frozen soils where water turns to ice, LNAPLs behave differently. First, LNAPL penetration rates were reported to decrease in frozen soils due to an increase in the viscosity (Singh and Niven, 2013). In addition, using gravelly sands, Andersland et al. (1996) reported that dry unfrozen and frozen soils have similar hydraulic conductivities, however hydraulic conductivities decrease with an increase in ice content. Wiggert et al. (1997) performed tests to study the interaction between ice saturation and intrinsic permeability and reported that the permeability decreases nearly linearly with an increase in ice saturation. Consequently, LNAPL penetration rates also decrease with an increase in ice saturation (McCauley et al., 2002). In the extreme, high ice saturations may even result in a nearly impermeable ground surface, promoting surface spread (Barnes and Chuvilin, 2009).

1.3.2.1 LNAPL Experiments in Frozen Homogeneous Soils

To the author's knowledge, most laboratory experiments involving LNAPL migration in frozen soils to date were performed on frozen porous media with homogeneous grain distribution and water/ice contents. Those experiments were helpful in understanding the isolated effects of pore ice and freezing temperatures on LNAPL migration in different types of frozen homogeneous sands. For example, Biggar and Neufeld (1996) packed a 30-cm high saturated silty sand soil column with a layer of diesel-contaminated soil placed on top and performed freeze-thaw cycles such that the top of the cell could freeze and thaw (to mimic an active layer), while keeping the bottom part of the cell permanently frozen (to mimic a permafrost table). After eight freeze-thaw cycles, results showed considerable migration of diesel into the saturated uncontaminated soil subjected to cyclic freezing and thawing, however, the permanently saturated frozen soil showed no contamination. Ice lenses in the field have also been observed to be effective barriers to LNAPL vertical migration (Biggar et al., 1998). However, researchers have reported some evidence of the potential for LNAPL to move into small fissures and vertical cracks formed by thermal contraction in frozen saturated soils, suggesting that even a high ice saturation permafrost table can allow vertical LNAPL migration in certain conditions (Biggar and Neufeld, 1996; Biggar, n.d.; Biggar et al., 1998).

Ice acts as a solid in the ground, changing the pore geometry and capillarity of the soil (Barnes and Chuvilin, 2009). Barnes and Shur (2003) and Barnes and Wolfe (2008) investigated how pore ice impacts the migration of petroleum hydrocarbons (LNAPL) by spilling 100 ml of colored LNAPL in frozen laboratory soil flumes (at -5 ^{o}C) packed homogeneously with respect to both grain size and water saturations. Two different sand grain sizes were used (coarse sand: grain size of 0.6 mm, and medium sand: grain size of 0.212 mm) at two different uniform water saturations (resulting in ice saturations of 26 % and 54 % once frozen) for a total of four tests. The

tests conducted on the coarse sand showed that an increase in ice saturation can cause an increase in lateral movement of LNAPL due to restricted or blocked pore space by ice (LNAPL widths were 0.19 m at 26 % ice saturation, compared to 0.43 m at 54 % ice saturation). In addition, ponding of LNAPL occurred at 54 % ice saturation after being introduced into the flume, but not at 26 % ice saturation. The authors attributed the ponding effect to a decrease in permeability of the porous medium at higher ice saturation. Finally, the maximum depth of penetration was greater at 54 % ice saturation, which was attributed to the initial pressure head of LNAPL created as it was introduced into the flume (it ponded) and a decrease amount of pore space available to retain LNAPL causing deeper migration.

With respect to tests conducted on medium sand, LNAPL widths were similar at both ice saturations (0.28 m at 26 % ice saturation, compared to 0.30 m at 54 % ice saturation), which Barnes and Wolfe (2008) attributed to clusters of ice-saturated pores being approximately the same size in both packs, but possibly more numerous at 54 % ice saturation. According to Barnes and Wolfe (2008), and Fourie et al. (2007), it is possible that infiltrating liquid water in frozen soils (or water rearrangement in this case as the cell was freezing) may be retained by capillary forces, which once frozen might create dead-end pores resulting in ice-saturated pore space and the formation of preferential pathways around the blocked pore space. Additionally, the same initial ponding behaviour occurred in the medium sand at 54 % ice saturation. Finally, penetration was less in tests conducted on medium sand, which Barnes and Shur (2003) attributed to a greater decrease of pore channel diameters in finer sand resulting in an increase in capillary pressure and associated LNAPL lateral or restricted overall movement.

1.3.2.2 LNAPL Experiments in Frozen Heterogeneous Soils

To date, there is a very limited record of LNAPL experiments conducted in frozen heterogenous soils. It was reported by Barnes and Chuvilin (2009) that Barnes and Adhikari had completed an experiment to investigate petroleum migration into a frozen sand pack that contained a simple form of geological heterogeneity (a 1.3 cm thick fine-grained layer interbedded between coarse grain sand layers). For this investigation, the soil was thoroughly wetted by introducing water to the top of the flume, however water was allowed to drain through the sand layers (Barnes and Chuvilin, 2009). When water drainage ended (water in the pore space was held by capillary forces at some residual level, presumably with higher water content in the finer-grained layer), the flume was insulated on the sides and bottom and placed in a cold room at -5 ºC to induce a top-down freezing (Barnes and Chuvilin, 2009). Once frozen, colored jet fuel (JP2) chilled to -5 ºC was introduced to the top of the soil layer, and migration of the petroleum through the soil was tracked using time-lapse photography (Barnes and Chuvilin, 2009). The test was also repeated in the same manner, but in unfrozen condition. The authors reported that while LNAPL was able to breach through the fine-grained layer in the unfrozen condition, it was not able to do so in the frozen condition. The fine-grained layer retained enough water, which once frozen, was sufficient to create an impermeable barrier. To the authors knowledge, this unpublished study is the only experiment to explore the impact of heterogeneity on LNAPL migration through frozen soil.

1.4 Research Needs and Objectives

While it is understood that heterogeneity in geology (in unfrozen soils) and pore ice (in frozen soils) individually play an active role in LNAPL migration, the effects of those complexities combined together remains unknown. The goal of this research was to start closing that gap by

performing controlled laboratory investigations on LNAPL migration in frozen heterogeneous media with respect to both geology and water/ice contents. Specific objectives were to:

- Adapt an existing method traditionally used in unfrozen soils to frozen soils and validate its used through quantitative analysis of water and ice.

- Use the chosen method to perform a macroscopic analysis of LNAPL migration in three different sand packs with various degrees of heterogeneity and analyse the spill migration in these packs in both unfrozen and frozen conditions.

1.5 Thesis Organization

The thesis is organized in an article-based (manuscript) format. Chapters 2 and 3 were written as standalone research papers with the intent of publishing them in the near future. Chapter 2 focuses on the laboratory research technique employed in this study. The application, validation, and demonstration of the light transmission method (LTM) in frozen soils is discussed. Chapter 3 focuses on the study of the combined effects of heterogeneity in geology and ice content on LNAPL migration. Chapter 4 presents the conclusions of this research and recommendations for future work. Due to the nature of the article-based format, some elements in the thesis introduction are repeated in the introduction of both chapters 2 and 3.

1.6 References

Andersland, O., Wiggert, D., & Davies, S. (1996). Hydraulic conductivity of frozen granular soils. *J. Env. Eng.*

Aziz, S. (2022, Jan 23). *Fuel Contamination Concerns Continue to Cloud Iqaluit's Drinking Water. Here's Why.* Retrieved from Global News: https://globalnews.ca/news/8532174/iqaluit-water-fuel-contamination-problem/

Barnes, D., & Chuvilin, E. (2009). Migration of Petroleum in Permafrost-Affected Regions. In R. Margesin, *Permafrost Soils.* Springer.

Barnes, D., & Shur, Y. (2003). Investigation of Immiscible Fluid Movement Through Frozen Porous Media. *Water Resources Center*.

Barnes, D., & Wolfe, S. (2008). Influence of Ice on the Infiltration of Petroleum into Frozen Coarse-Grained Soil. *Petroleum Science and Technology*.

Bickerton, G., Van Stempvoort, D., & Voralek, J. (2007). Hydrogeological Setting of Petroleum Contamination at Colomac Mine, NWT; A Permafrost Region of the Canadian Shield. *OttawaGeo2007*.

Biggar, K. (n.d.). Contaminant Movement in Permafrost and Freezing Soils.

Biggar, K., & Neufeld, J. (1996). Vertical Migration of Diesel into Silty Sand Subject to Cyclic Freeze-Thaw. *8th Annual International Conference on Cold Regions Engineering*.

Biggar, K., Haidar, S., Nahir, M., & Jarrett, P. (1998). Site Investigations of Fuel Spill Migration into Permafrost. *Journal of Cold Regions Engineering*.

Carroll, L. (2022, June 15). *An Oily Plastic Container Was at the Heart of Sachs Harbour's Water Contamination this Spring*. Retrieved from CBC News: https://www.cbc.ca/news/canada/north/sachs-harbour-water-contamination-n-w-t-1.6488652

cbc.ca. (2022, Apr 20). *One Month Later, People in Sachs Harbour Still Avoiding Fuel-Contaminated Tap Water*. Retrieved from cbc.ca: https://www.cbc.ca/news/canada/north/sachs-harbour-water-update-1.6425449

de Grandpré, I., Fortier, D., & Sephan, E. (2012). Degradation of Permafrost beneath a Road Embankment Enhanced by Heat Advected in Groundwater. *Can. J. Earth Sci.*

Domenico, P., & Schwartz, F. (1998). Physical and Chemical Hydrogeology. *Wiley*.

Ewing, R., & Berkowitz, B. (1998). A Generalized Growth Model for Simulating Initial Migration of Dense Non-Aqueous Phase Liquids. *Water Resources Research*.

Explore North. (2006, April 2). *Contaminated Sites in the Northwest Territories*. Retrieved from Explore North, An Explorer's Guide to the North: https://explorenorth.com/library/mining/nwt-contaminated_sites.html#3

Fourie, W., Barnes, D., & Shur, Y. (2007). The Formation of Ice from the Infiltration of Water in Frozen Coarse Grain Soils. *Cold Regions Sci. Technol.*

Iwakun, O., Biggar, K., Van Stempvoort, D., Bickerton, G., & Voralek, J. (2007). Fuel Contamination Characterization in Permafrost Fractured Bedrock at the Colomac Mine Site. *Cold Regions Science and Technology*.

Kechavarzi, C., Soga, K., Illangasekare, T., & Nikopoulos, P. (2008). Laboratory Study of Immiscible Contaminant Flow in Unsaturated Layered Sands. *Vadose Zone Journal*.

Leverett, M. (1941). Capillary Behaviour in Porous Solids. *Trans. Am. Inst. Min. Metall. Pet. Eng.*

McCauley, C., White, D., Lilly, M., & Nyman, D. (2002). A Comparison of Hydraulic Conductivities, Permeabilities and Infiltration Rates in Frozen and Unfrozen Soils. *Cold Regions Science and Technology*.

McKenzie, J., Kurylyk, B., Walvoord, M., Bense, V., Fortier, D., Spence, C., & Grenier, C. (2021). Invited Perspective: What lies beneath a changing Arctic? *The Cryosphere*.

Mercer, J., & Cohen, R. (1990). A Review of Immiscible Fluids in the Subsurface: Properties, Models, Characterization and Remediation. *Journal of Contaminant Hydrology*.

Miller, C., Durnford, D., & Fowler, A. (2004). Equilibrium Nonaqueous Phase Liquid Pool Geometry in Coarse Soils with Discrete Textural Interfaces. *Journal of Contaminant Hydrology*.

Montoro, M., & Francisca, F. (2013). Digital Image Analysis of Distribution of Immiscible Fluids in Natural Porous Media. *Geotechnical Testing Journal*.

Muller, S. (1943). Permafrost or Permanently Frozen Ground and Related Engineering Problems. *U.S. Engineers Office, Intelligence Branch, Strategic Engineering Study Special Report 62*.

Mumford, K., Kueper, B., & Lenhard, R. (2022). Flow and Distribution of Non-Aqueous Phase Liquids. In *The Groundwater Project.* ISBN: 978-1-77470-069-3, 69 pages (In Press).

Nadeau, P. (2019). Geotechnical Centrifuge Modelling of Contaminant Transport Through Frozen Soil.

Newell, C., Acree, S., Ross, R., & Huling, S. (1995). Light Nonaqueous Phase Liquids. *EPA Ground Water Issue*.

Pankow, J., & Cherry, J. (1996). Dense Chlorinated Solvents and Other DNAPLs in Groundwater. *Waterloo Press*.

Poulsen, M., & Kueper, B. (1992). A Field Experiment to Study the Behaviour of Tetrachloroethylene in Unsaturated Porous Media. *Environ. Sci. Technol.*

Rivett, M., Tomlinson, D., Thornton, S., Thomas, A., Leharne, S., & Wealthall, G. (2014). An Illustrated Handbook of LNAPL Transport and Fate in the Subsurface. *CL:AIRE*.

Schroth, M., Istok, J., Selker, J., Oostrom, M., & White, M. (1998). Multifluid Flow in Bedded Porous Media: Laboratory Experiments and Numerical Simulations. *Advances in Water Resources*.

Singh, K., & Niven, R. (2013). Non-Aqueous Phase Liquid Spills in Freezing and Thawing Soils: Critical Analysis of Pore-Scale Processes. In L. Ma, *Critical Reviews in Environmental Science and Technology*. Taylor & Francis.

Sjoberg, Y., Coon, E., Sannel, A., Pannetier, R., Harp, D., Frampton, A., . . . Lyon, S. (2016). Thermal Effects of Groundwater Flow Through Subarctic Fens: A Case Study Based on Field Observations and Numerical Modeling. *Water Resources Research*.

Walvoord, M., & Kurylyk, B. (2016). Hydrologic Impacts of Thawing Permafrost – A Review. *Vadose Zone Journal*.

Wiggert, D., Andersland, O., & Davies, S. (1997). Movement of Liquid Contaminants in Partially Saturated Frozen Granular Soils. *Cold Regions Science and Technology*.

Woo, M.-k. (2012). *Permafrost Hydrology*. Springer.

CHAPTER 2 ICE QUANTIFICATION USING THE LTM

2.1 Introduction

The study of permafrost groundwater has been driven by the search for water supply, by problems associated with groundwater in mining and in construction of buildings, highways, railways, airfields and pipelines, and by encounters with ice features in the course of permafrost and geological mapping (Woo, 2012). Permafrost exerts a primary control on water fluxes, flow paths and distribution (Walvoord and Kurylyk, 2016). The presence of ice, the influence of seasonal freeze and thaw cycling, and the typically shallow active layers found in permafrost environments all impact the movement of fluids in a manner not found in temperate soils (soils that do not experience deep freezing) (Barnes and Chuvilin, 2009). Not only is groundwater movement affected by the current permafrost conditions, it also might be undergoing changes in the future. Climate warming is expected to modify the permafrost distribution, leading to alterations in hydrologic conditions, including variations in soil moisture, connectivity of inland waters (i.e., taliks), streamflow seasonality, and the partitioning of surface and subsurface water (Walvoord and Kurylyk, 2016). Understanding groundwater behaviours in permafrost terrain is essential for managing and protecting water resources and critical infrastructure in a changing climate and requires multi-disciplinary studies including geotechnical and environmental engineering.

Investigating water movement and distribution in soils, under both frozen and unfrozen conditions is often done using laboratory experiments (Goit et al., 1978; Spaans and Baker, 1995; Heller et al., 2009; Werth et al., 2010; Dobriyal et al., 2019). Many methods exist to measure water content in soil in time and space. They can generally be separated into direct and indirect measurement methods. The direct measurement method, also referred to as the gravimetric method, involves measuring the difference in weight of a soil sample before and after drying (Belfort et al., 2019). It is accurate and inexpensive, but it is also destructive, time consuming and does not allow for replications thereby having limited spatial and temporal coverage (Dobriyal et al., 2012). Non-destructive indirect measurement methods, such as time domain reflectometry and neutron probe techniques can deliver accurate soil moisture measurements (e.g., Dobriyal et al., 2012). However, these traditional indirect methods for measuring water content within laboratory test cells are limited in spatial and temporal resolution or require very specialized and expensive equipment (Tidwell and Glass, 1994). Imaging techniques are good non-destructive, non-invasive alternatives for measuring water content. They can lead to quantitative measurements without inserting (m)any probes in the porous media (Belfort et al., 2019). Imaging techniques also have advantages with respect to resolution in time and space. For example, in the time it takes to measure a single point by one of the traditional techniques, an entire image consisting of hundreds of thousands of points can be acquired by imaging light techniques (Tidwell and Glass, 1994). The resolution of imaging techniques allows for investigations of fast processes, such as rapid transient flow and preferential flow, which is key to understanding water dynamics typically found in the vadose zone (Darnault et al., 1998; Sills et al., 2017; Orozco-Lopez et al., 2021). The high spatial and temporal resolution needed to investigate water in unfrozen systems also applies to water and ice in frozen systems. For example, due to its low hydraulic conductivity, permafrost strongly affects the movement, storage, and exchange of surface and subsurface water (Walvoord and Kurylyk, 2016). In turn, subsurface flow can affect the distribution of permafrost by increasing the transfer of thermal energy via heat advection (de Grandpré et al., 2012; Sjöberg et al., 2016; Walvoord and Kurylyk,

2016). This interplay, along with physical, chemical, and biogeochemical processes, creates complex, and often nonintuitive, dynamics in permafrost regions (Walvoord and Kurylyk, 2016). As a result, there is a need to develop or modify a non-destructive high-resolution laboratory technique for application to frozen systems.

The light transmission method (LTM) is a non-destructive, non-invasive imaging technique that does not require specialized equipment and is, therefore, a low-cost method (Niemet and Selker, 2001). It has been used in a wide variety of two-dimensional (2D) laboratory studies to investigate water saturations in both stable and transient flow fields (Tidwell and Glass, 1994; Niemet and Selker, 2001; Orozco-Lopez et al., 2021), wetting and nonwetting fluid saturation in porous media (i.e., water and NAPL respectively) (Darnault et al., 1998; Glass et al., 2000; Darnault et al., 2001; Conrad et al., 2002; Zhang et al., 2021), and gas migration investigations (Van De Ven and Mumford, 2018; Van De Ven et al., 2020). The high resolution of the LTM coupled with the quality of data that it yields makes this technique a valuable tool for investigating unsaturated flow phenomena (Tidwell and Glass, 1994). The LTM stands out amongst other methods as it allows fluid mapping over an entire flow cell in a single image capture; however, it requires experiments to be performed in thin cells filled with translucent porous medium. Given the success of the LTM for the investigation of water distribution in laboratory experiments, and the need to investigate frozen soils at a high spatial resolution, there is an opportunity to adapt the LTM for use in frozen soils. To the author's knowledge, no attempts have been made to quantify ice using the LTM. Wang et al. (2021) successfully applied a modified version of the LTM to investigate the remobilization of light non-aqueous phase liquids in unsaturated porous media subject to freeze-thaw cycles, however they did not provide quantitative data on ice saturations.

This paper explores the application of the LTM on frozen porous media and its potential to differentiate air and ice in a partially saturated sand pack. Specific objectives of this work were to: 1) compare LTM images in frozen and unfrozen sand, 2) validate existing saturation-intensity relationships for use in frozen sand, and 3) investigate water and ice saturation maps and profiles. These objectives were addressed using a series of experiments conducted in an intermediate scale 2D flow cell. For an experiment to be classified as intermediate scale, the flow cell has to be small enough for its boundary conditions to be controlled and allow small scale processes to manifest themselves at a larger scale so they can be studied and quantified (Oostrom et al., 2007).

2.2 Methodology

2.2.1 Light Transmission Method

The LTM consists of placing a thin experimental flow cell between a light assembly and a digital camera to measure the intensity of light passing through the cell in space and time (Figure 2.1a). The cell is filled with translucent sand, which allows light to be transmitted and provide a two-dimensional representation that is integrated over the pack thickness (Figure 2.1b). This method was used by Tidwell and Glass (1994), who proposed a physical model and derived equations for determination of liquid saturation based on the attenuation of light by the sand grains and fluid-fluid interfaces. Niemet and Selker (2001) extended the method by developing five physically based relationships relating light transmission to liquid saturation based on different assumptions about pore geometry, wettability, and drainage characteristics. The light transmission method combines Beer's law (light passing through a homogeneous medium) and Fresnel's Law

(the refraction and absorbance of light passing through interfaces), described mathematically as (Tidwell and Glass, 1994; Niemet and Selker, 2001):

$$I = CI_0\tau_{pl}^{2kS}\tau_{pg}^{2k(1-S)}\exp\left(-\alpha_p d_p k\right) \tag{1}$$

where I is the transmitted intensity, C is an optical geometric term which corrects for the position of emitted and captured light, I_o is the light intensity of the light source, τ is the average transmittance of an interface and the subscripts p, l, and g refer to the grain (particle), liquid and gas, respectively, k is the number of particles or pores across the medium thickness, S is the degree of saturation averaged over the medium thickness, α_p is the absorbance coefficient of the grain and d_p is the thickness of a grain. τ is related to the refractive index of both media on either side of the interface, which may cause either light reflection and/or refraction. The normalized light intensity, I_n, is a measure of the relative degree of light transmission between saturated and dry conditions defined as (Selker et al., 1989):

$$I_n = \frac{I-I_d}{I_s-I_d} = \frac{\left(\frac{I}{I_s}\right)-\left(\frac{I_d}{I_s}\right)}{1-\left(\frac{I_d}{I_s}\right)} \tag{2}$$

where I_d and I_s are the light intensities transmitted through completely dry (S = 0) and completely saturated (S = 1) sand, respectively (Niemet and Selker, 2001). Substituting Eq. 1 into (2) and solving for S yields (Tidwell and Glass, 1994):

$$S = \frac{\ln\left(I_n\left[\left(\frac{\tau_{pl}}{\tau_{pg}}\right)^{2k}-1\right]+1\right)}{2kln\left(\frac{\tau_{pl}}{\tau_{pg}}\right)} \tag{3}$$

Using Eq. 1 and considering the ratio of saturated to dry condition intensities gives:

$$\frac{I_s}{I_d} = \frac{CI_0\tau_{pl}^{2k}\exp\left(-\alpha_p d_p k\right)}{CI_0\tau_{pg}^{2k}\exp\left(-\alpha_p d_p k\right)} = \left(\frac{\tau_{pl}}{\tau_{pg}}\right)^{2k} \tag{4}$$

Combining Eqs. (3) and (4) results in (Niemet and Selker, 2001):

$$S = \frac{\ln(I)-\ln\left(I_d\right)}{\ln(I_s)-\ln\left(I_d\right)} = 1-\frac{\ln\left(I/I_s\right)}{\ln\left(I_d/I_s\right)} \tag{5}$$

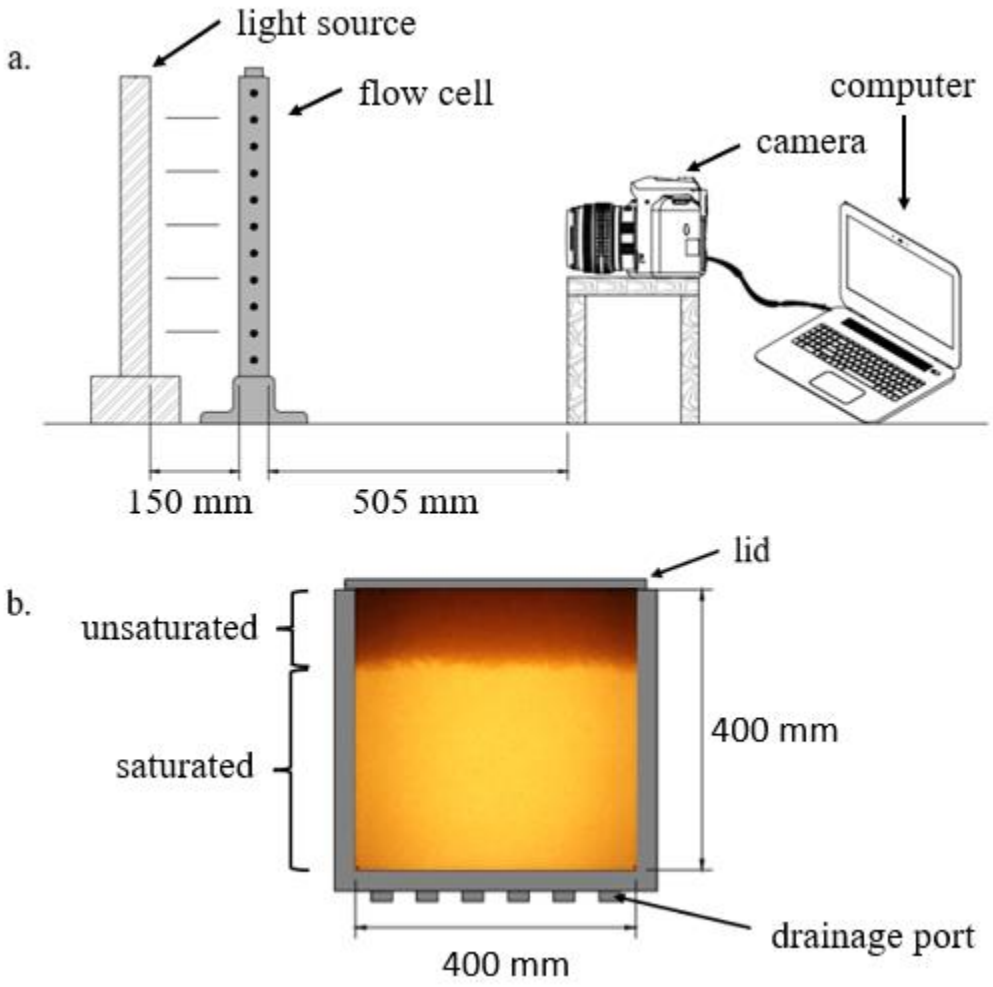

FIGURE 2.1: Experimental set-up showing the (a) light transmission and data acquisition system and (b) example of a light transmission image.

As an alternative to Eq. 5, Niemet and Selker (2001) proposed that an image at residual water saturation could be used instead of a dry image, assuming that a water film remains coated on the particles once they are wetted and drained, and that an effective pore space exists between liquid films instead of between sand grains. As a result, an effective saturation can be calculated as (Niemet and Selker, 2001):

$$S_e = 1 - \frac{\ln (I/I_s)}{\ln (I_r/I_s)} \tag{6}$$

where I_r is the light intensity transmitted through residual saturated sand. Absolute saturation is then related to effective saturation as (Niemet and Selker, 2001):

$$S = S_e(1 - S_r) + S_r \tag{7}$$

where S_r is the residual saturation, a measure of the total volume fraction of water held within the water films surrounding sand grains. The visual representation of saturation in a cell using the LTM is shown in Figure 2.1b. In this particular image, approximately 75 % of the cell is saturated, identified by the bright light intensity, while the top portion is unsaturated, identified by the much darker light intensity.

Pure ice and water have the same refractive indexes. The refractive indexes are just as different between water and a particle and between water and air as they are between ice and a particle and between ice and air. Therefore, differences in transmitted light intensity between air and water in an unfrozen sand pack are expected to be similar to differences between air and ice in a frozen sand pack. Furthermore, Eq. 1 could be rewritten by replacing τ_{pl}^{2kS} by $\tau_{pi}^{2kS}$where the subscript *i* would refer to ice. The mathematical development of Eq. 6 would be the same and Eq. 6 could be valid for use on frozen soil (the only difference would be that *S* would refer to ice saturation in frozen conditions). Eq. 7 would also remain the same, except that S_r would be the frozen S_r value for frozen experiments. Further, because pure ice and water have the same refractive indexes, it is hypothesized that $\tau_{pl}^{2kS} \cong \tau_{pi}^{2kS}$ suggesting that the S_{ice}-I/I_s relationship will be the same as S_{water}-I/I_s relationship.

2.2.2 Experimental Set-up

The experimental set-up used in this study is based on previous LTM studies by Tidwell and Glass (1994), Niemet and Selker (2001) and Davidson et al. (2022), with minor modifications to the size of the set-up to make it fit in a chest freezer. The RMC LTM flow cell (Figure 2.2) was built with two 6 mm glass panels sealed to an aluminum frame using a Neoprene O-ring, resulting in interior dimensions of 400 mm × 400 mm × 12 mm. The total volume of the cell was 1,925 ml, which accounts for the small cavities at each port. The cell was equipped with six bottom ports allowing for water drainage and imbibition. Each port was topped with a water-wet nylon net filter (Merck Millipore Ltd., 80 μm); a membrane allowing water to go through while preventing sand and air from escaping the cell during water drainage and imbibition, which allowed the entire cell to be drained under vacuum using flexible transparent tubes linking the bottom ports to the water table control beaker.

FIGURE 2.2: Flow cell image showing the cell frame, glass panels, bottom ports, and flexible transparent tubes. Each port is topped with a water-wet net filter.

The light panel assembly used was built with LEDs (Ledgo-LG-1200S) and placed 150 mm from the cell. Images were captured using either a Canon Rebel XSI or Canon Rebel T2i camera with an EFS 10-18 mm image stabilizer lens placed 505 mm in front of the cell (Figure 2.1a). The camera was set-up to manual focus with the following settings: 1/10 as the shutter speed, F16 as the aperture and ISO 1600. The settings were chosen manually in order to get high quality images (0.01695 mm^2/pixel) and maintain consistency between images. The light, cell and camera were affixed in place on a mobile testing platform so the entire set-up could be placed in a freezer for frozen experiments. Black-out black curtains were also used to cover the set-up to prevent errors in light intensity measurements due to ambient light or light reflection from the sides of the freezer.

2.2.3 Sand Packing

The sand used in this study was ASTM 20/30 silica sand, also referred to as Accusand, and was selected due to its previous use in LTM studies (e.g., Schroth et al., 1998; Davidson et al., 2022). The properties of the sand are a particle diameter (d_{50}) of 0.713 ± 0.023 mm, a uniformity coefficient (d_{60}/d_{10}) of 1.190 ± 0.028, particle sphericity of 0.9, and a particle density of 2.664 Mg/m^3 (Schroth et al., 1996). Before use, the sand was rinsed with deionized water to remove fines

and dust. The sand was then oven dried for 24 h at 110 °C. Each experiment required starting with dry sand for the calculation of porosity.

The flow cell was filled using the wet pack method (otherwise called slurry packing), a technique involving oversaturating the soil with water before letting it settle at the bottom of the flow cell. A fitted funnel was used to facilitate the procedure. A rubber mallet was also used to vibro compact the sand as it was settling into the flow cell for proper consolidation and distribution. Using the wet pack method resulted in a uniform, homogeneous saturated pack. The unused sand slurry was oven dried to determine its mass and subtracted from the initial amount of dried sand to calculate the total amount of sand in the pack. The porosity of each pack, which was calculated from the known volume of the cell and the amount of sand used to fill it ranged from 0.333 to 0.340.

2.2.4 Unfrozen and Frozen Experiments

Unfrozen experiments were performed at room temperature (~22 °C). To capture images of sand in frozen conditions, the entire set-up (light, cell, camera, and platform) was placed in a chest freezer (Frigidaire FFFC20M4TW, interior dimensions: 1702 mm long, 546 mm wide, 635 mm high) set to a temperature of approximately -28 °C. The mobile platform was built out of wood painted in mat black and had reference markers to ensure that all pieces of equipment were always installed in the same location. The light was kept on at all times in the freezer including while the cell was freezing. Doing so prevented the cell from freezing too fast, which would allow for frost to appear on the glass surfaces. Silica beads were also found to help minimize the humidity level in the freezer, keeping frost formation under control. A temperature probe (Traceable 4000 90080-09) was inserted in the top portion of the cell at the conclusion of two tests to measure the temperature of the frozen pack. This was completed at the end of the tests to avoid destructing the sand structure prior to, or during a test. With the light on, the cell temperature remained constant at -9 °C after a minimum of 18 h in the freezer. Once images of the frozen cell were captured, the set-up was taken out of the freezer and the cell was allowed to thaw for a minimum of 2.5 h with the light on. Images of a saturated cell were captured in the unfrozen state in both environments (in and out of the freezer). These were then compared to ensure that the intensities recorded were the same, and that any differences between intensities in unfrozen and frozen sand packs were not from the different imaging environments.

2.2.5 Targeted Saturation and Image Capture

Each water table adjustment was performed in slow increments by lowering (or increasing for “trapped gas” images) the water table control beaker by 10 mm every 5 min, keeping the cell in a quasi-static condition as it was draining. Once the water table control beaker had been set to the desired height in each drainage step, the cell was allowed to come to equilibrium for a minimum of 30 min before images were captured, with the exception of residual saturation, for which the cell was allowed to come to equilibrium for 2 h. The mass of water removed or added during each water table adjustment was tracked.

Images were captured at various water positions in the cell. The testing sequence first started with a saturated cell (to obtain I_s). The water table was then dropped so the water position in the cell (the top of the capillary fringe) was at approximately 75 % of the cell height. The cell was then frozen for a period of 18 h, after which the cell was thawed and the water position in the cell was

dropped to approximately 50 % of the cell height. This process of sequential drainage, freezing and thawing was repeated until the cell was drained to residual saturation (to obtain I_r), ensuring that each test included images captured at several different water positions in the cell (a minimum of three) in both unfrozen and frozen conditions. After the cell was drained to residual saturation, water was imbibed from the bottom tubes and images were captured to obtain "trapped gas" (TG) images (unfrozen state only).

2.2.6 Image Processing

Ten images were captured for each saturation condition (one image every 2-3 s). For unfrozen cells, the images of the saturated cell were used to obtain I_s, however, for the frozen cells, images of the cell where the water position was at approximately 75 % of the cell height in unfrozen conditions were used as I_s images (for ice quantification). This reduced water position ensured the cell would not overflow due to water expansion when freezing, thus ensuring proper tracking of water removed from the cell during drainage. All images were processed using MATLAB. The image processing steps first averaged the 10 images taken at each water position in the cell to obtain a single image. Using the average of 10 images minimized the effects of potential light intensity variations. All images were then converted to grayscale to eliminate the hue and saturation information and retain only the pixel light intensities. Images were also cropped to eliminate edge effects and the cell frame. Images were then upscaled to 1 mm^2 blocks by averaging all intensity values within a given 1 mm^2 block to ensure that each block was larger than a grain of sand and to reduce the noise created by darker pixels and minor variations in the incident light. A precision/resolution analysis determined that 1 mm^2 block size provided the least amount of noise in the pictures (low standard deviation in a zone of known consistent saturation), while still providing adequate visual saturation mapping. Details of the precision analysis can be found in Appendix A. Local water or ice saturations were calculated using Eqs. 6 and 7 and used to generate saturation maps, which were integrated to estimate volumes of water in the flow cell for comparison to the drainage measurements.

The mass of water removed from the cell at each water table adjustment was converted to total water volumes in the cell based on either a density of 1 g/ml for water or 0.917 g/ml for ice (i.e., a 9 % volume expansion during freezing). Rather than use a measured value of I_r/I_s, the value of that ratio was used as a calibration parameter such that the drainage-based water (ice) volumes matched the image-based water (ice) volumes. This fitting procedure has been used previously for unstable gas injection where the measured I_r image is not a suitable representation of local S_r conditions (Mumford et al., 2015; Van De Ven et al., 2020). More details on the fitting procedure can be found in Appendix F.

2.3 Results and Discussion

2.3.1 Captured Images

A total of 5 cell sand packs were poured, from which a total of 8 tests were conducted. Packs 1 through 5 all underwent an unfrozen test, and packs 1, 2 and 4 also underwent a frozen test. A complete list of tests, and their respective captured water positions in the cell (the top of the capillary fringe) is shown in Table 2.1.

TABLE 2.1: List of tests and their respective captured water positions in the cell. U and F stands for unfrozen and frozen respectively. U1, U2 and U4 were also performed in frozen conditions (referred to as F1, F2, and F4 respectively).

Tests	Water Positions in the cell
U1	Sr, 25 %, 50 %, 75 %, 100 %, TG
U2	Sr, 50 %, 75 %, 100 %
U3	Sr, 25 %, 50 %, 75 %, 100 %, TG
U4	Sr, 25 %, 40 %, 50 %, 75 %, 100 %, TG
U5	Sr, 25 %, 50 %, 75 %, 100 %
F1	Sr, 25 %, 50 %, 75 %
F2	Sr, 50 %, 75 %
F4	Sr, 25 %, 40 %, 50 %, 75 %

An example of the images captured at each water table position during test U3 is presented in Figure 2.3. The saturated image (Figure 2.3a) has a higher intensity throughout the flow cell because water-particle interfaces transmit more light than air-particle interfaces. As the water position in the cell was lowered (the top of the capillary fringe) and water drained from the flow cell (Figures 2.3b-d), a darker region appeared and expanded from the top of the flow cell until a residual saturation was reached (Figure 2.3e). Water imbibition to create trapped gas increased light intensity throughout the cell (Figure 2.3f), but not as high as under saturated conditions.

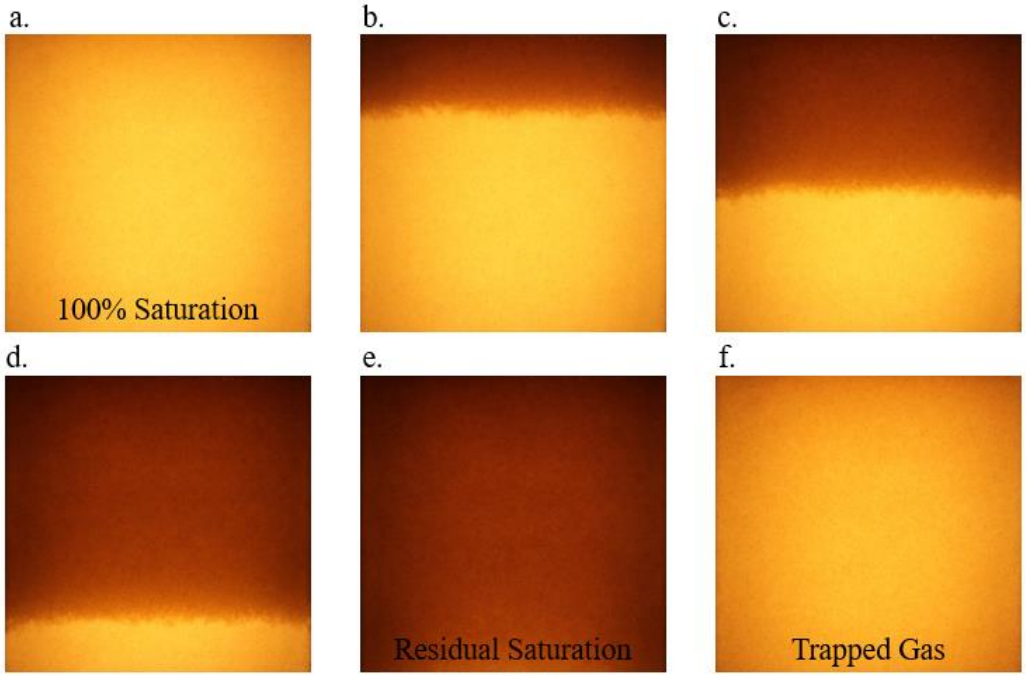

FIGURE 2.3: Example of light transmission images from test U3 prior to image processing showing (a) saturated conditions followed by unsaturated conditions with water positions at approximately (b) 75 %, (c) 50 %, and (d) 25 % of the cell height, as well as (e) residual saturation and (f) following water imbibition to create trapped gas.

Based on drained water volumes, the S_r values were calculated to be between 0.04 and 0.05, which is consistent with previously reported values between 0.046 and 0.048 (Schroth et al., 1996; Niemet and Selker, 2001) for the same sand packed at similar porosities. Therefore, a value of 0.046 was used in Eq. 7 for unfrozen tests, and a value of 0.050 was used for frozen tests (accounting for the 9 % increase in volume as water turns to ice).

2.3.2 Calibration

Table 2.2 shows the known and calculated water volumes in each image presented in Figure 2.3 (Test U3). The calculated water volumes (based on Eqs. 6 and 7) were obtained using a best-fit value of $I_r/I_s = 0.48$. The known and calculated water volumes from all tests are plotted in Figure 2.4. The calculated water volumes for all tests were obtained using the same best-fit value of $I_r/I_s = 0.48$, and this best-fit value applied to water saturation in unfrozen packs and to ice saturation in frozen packs. Images of frozen packs consistently appeared darker than their respective unfrozen ones, however the validity of a single fit parameter for I_r/I_s suggests that the unfrozen and frozen I_r/I_s ratios are the same. The ability to apply a single I_r/I_s value such that known and calculated ice volumes are within 2 % over a range of water/ice positions in the cell validates the use of the LTM in frozen soils for ice quantification. The applicability of the fit parameter to both ice and water also means that the calibration process can be performed in unfrozen conditions and then be applied to frozen conditions. The ability to calibrate results using a pack in the unfrozen state is an efficient calibrating procedure as it can be done much faster since the cell does not have to be frozen for several hours at each water table adjustment. In any saturation condition, ice can be quantified using a frozen saturated image to obtain I_s along with the fitting parameter for I_r/I_s, provided that the value of S_r is known.

TABLE 2.2: Test U3 known and calculated water volumes in the cell.

Water Position in the cell	Known Water Volume (ml)	Calculated Water Volume (ml)
Sr	30.04	30.16
25 %	157.62	157.57
50 %	334.95	337.28
75 %	500.23	495.29
100 %	652.97	654.69
TG	581.61	572.95

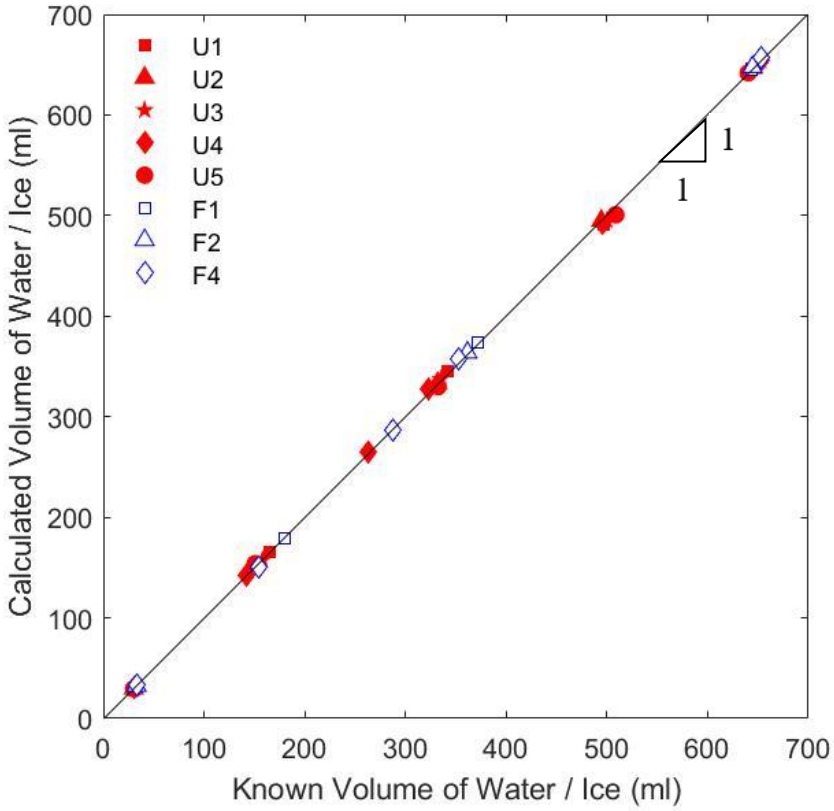

FIGURE 2.4: Calculated versus known volumes of water and ice in the cell from all tests.

2.3.3 Validation of *S*-I/I_s Relationships

Figure 2.5 demonstrates both S_{water}-I/I_s and S_{ice}-I/I_s relationships. The shape of the curves is consistent with Niemet and Selker (2001). Further, the relationships are nearly the same (the relationships overlap each other), however not because $\tau_{pl}^{2kS} \cong \tau_{pi}^{2kS}$ as previously hypothesised (images of frozen packs are darker), but due to the fact that the I_r/I_s ratio is the same in unfrozen and frozen sand packs (Eq. 6). The relationships are not identical because the frozen S_r is different than the unfrozen S_r (Eq. 7). Each curve starts at the fitting parameter (I_r/I_s = 0.48) and S_r (0.046 for unfrozen, 0.050 for frozen) and ends at the fully saturated conditions (I/I_s = 1, S = 1). In both cases, a small variation in I/I_s results in a much greater difference in S. In addition, any variation in S resulting in an I/I_s ratio less than the fitting parameter falls below the detection limit, which mainly affects the unsaturated transition zone on top of the capillary fringe. Anything below the detection limit results in a computed negative S_e, which is interpreted as an effective saturation of 0 (Eq. 6), therefore resulting in an absolute saturation S equivalent to S_r (Eq. 7).

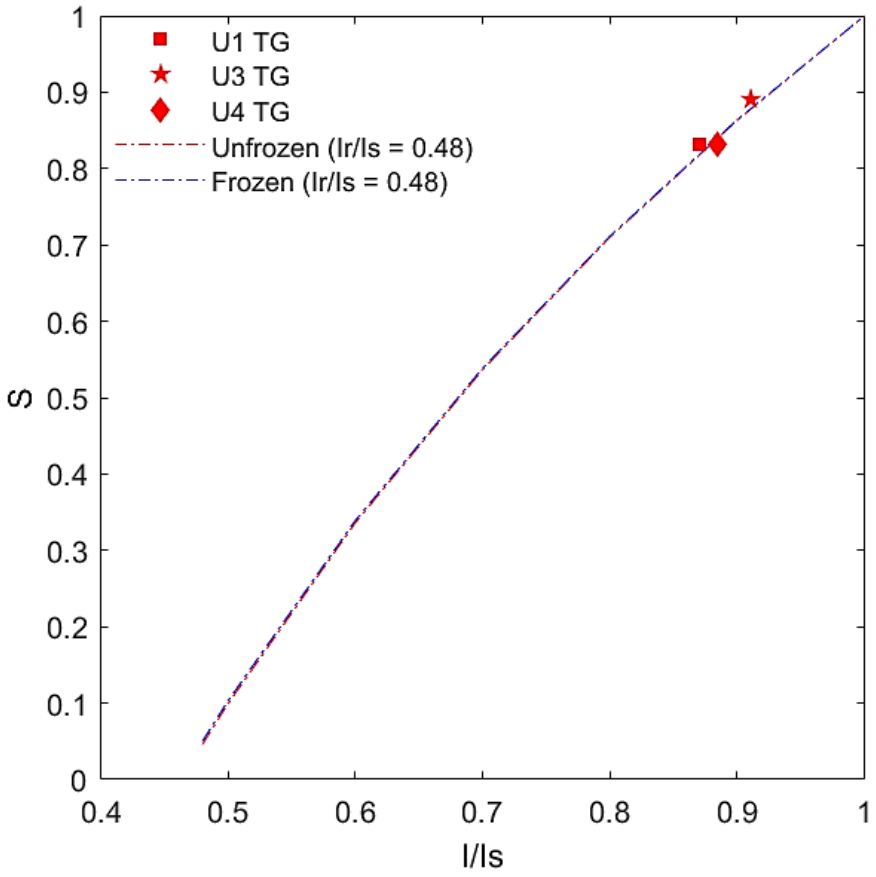

FIGURE 2.5: Relationship between *I/Is* and *S* for both unfrozen and frozen experiments with trapped gas images from tests U1, U3 and U4.

Generally, the water saturation of an unsaturated sand pack varies with height above the capillary fringe. There are two exceptions: 1) saturations in a fully drained sand pack (end of primary drainage) are equal to the residual saturation everywhere, and 2) saturations in a fully imbibed sand pack (end of secondary imbibition or beginning of secondary drainage) are equal to the difference between fully saturated and the maximum trapped gas saturation. This is in addition to fully saturated conditions, where the local saturations also do not vary with height (100 % everywhere). Because those saturations do not vary in space, they can be calculated based on the porosity and total water volume measured in the sand pack. Fully saturated and residual saturated conditions are used to calibrate the LTM, but the trapped gas conditions can be used for validation (Sills et al., 2017). The data presented in Figure 2.5 demonstrate that the saturations predicted using Eqs. 6 and 7 and the best-fit value of I_r/I_s = 0.48 reproduce measured saturation values under trapped gas conditions to within ± 2 %. As proposed by Sills et al. (2017), this supports an approach that uses the trapped gas (TG) images to determine the required I_r/I_s value rather than a series of images at different water positions in the cell, which would further reduce the effort required to calibrate the LTM for use in frozen conditions.

2.3.4 Saturation Maps and Profiles

One advantage of the LTM over traditional moisture content measurement techniques is its ability to measure local saturations over the entire field of interest. This technique is highlighted in Figure 2.6 for two images captured in unfrozen and frozen conditions during the tests U4 and F4, respectively. Saturation maps are useful to identify zones of 100 % saturation and residual saturation and they clearly illustrate the transition zones between the two using the colour bar. The colour scheme used in the saturation maps helps to visualize the 9 % increase in volume as water turns to ice, identified by the higher position of the ice in Figure 2.6d in comparison to the position of water in Figure 2.6b.

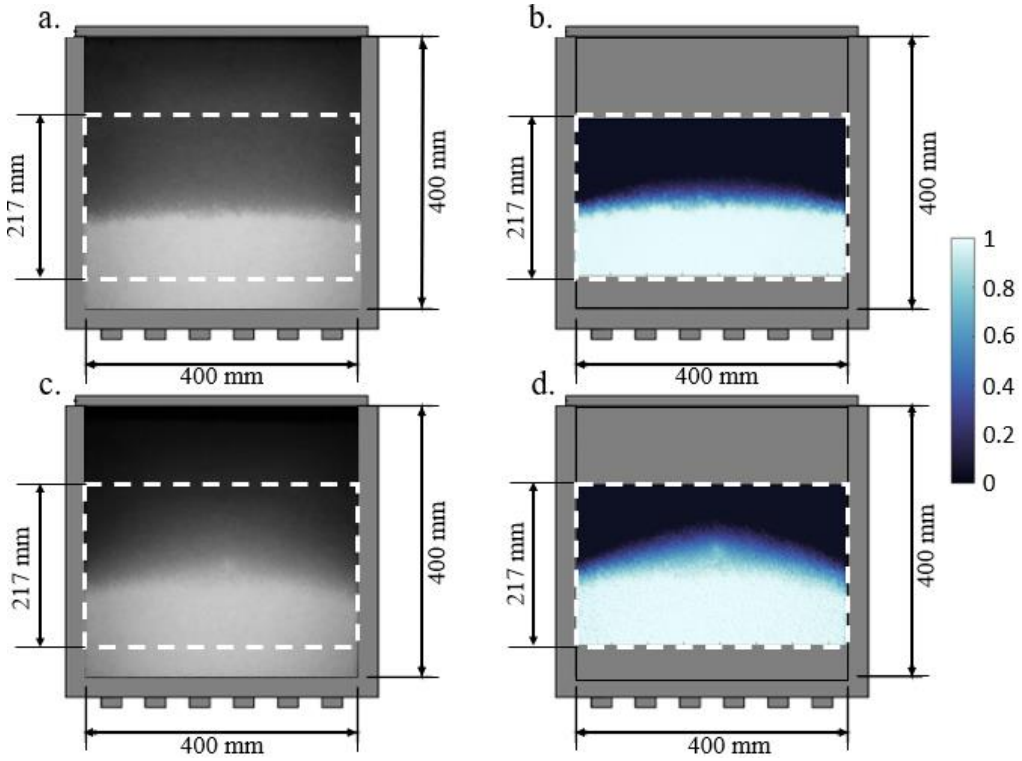

FIGURE 2.6: Water distribution in two zones of interest (dashed rectangles) in both unfrozen (U4) and frozen (F4) conditions shown as (a) unfrozen grayscale image, (b) unfrozen saturation map, (c) frozen grayscale image, (d) frozen saturation map.

Changes in ice distribution in the cell can also be assessed using profiles. In Figure 2.7, pixel intensities (from images) and saturation values (from saturation maps) from Figure 2.6 were averaged across the cell width. Doing so provides useful quantitative data for the investigation of unfrozen and frozen images and saturation maps.

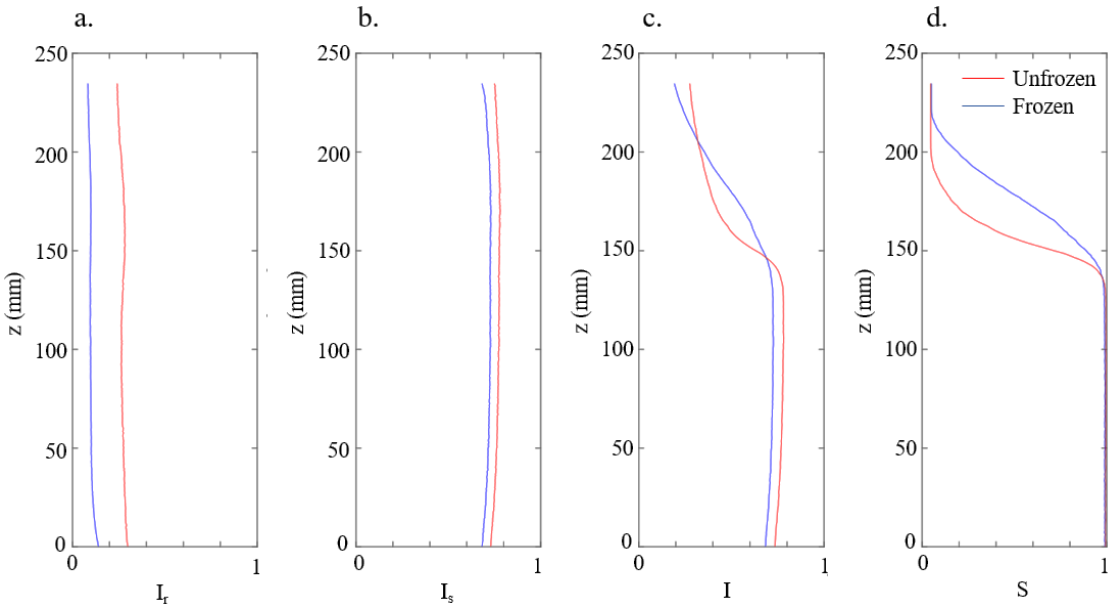

FIGURE 2.7: Intensity and saturation profiles versus height showing both unfrozen and frozen (a) residual saturation intensities, (b) 100 % saturation intensities, (c) evaluated images intensities, (d) evaluated images saturations.

For example, the 9 % increase in volume as water turns to ice can be seen in Figure 2.7d, where the frozen saturations are higher than the unfrozen ones in the transition zone between 100 % saturation and residual saturation. Otherwise, no change in saturation is observed between the unfrozen and frozen images (from top to bottom, they both start at residual saturations, and end at 100 % saturations). Further, as seen in Figure 2.7a, 2.7b and 2.7c, the intensities are darker in frozen test images than unfrozen. Even though pure ice and water have the same refractive indexes; the frozen tests images indicate that light is more attenuated in frozen sand packs, even more so at residual saturation when compared to 100 % saturation (Figures 2.7a, 2.7b), which indicates that the ice in the cell might not be pure. Fresnel's Law states that light can be refracted and absorbed as it passes through interfaces (Tidwell and Glass, 1994). Consequently, it is hypothesized that the air contained in the unfrozen water used to pack the cell gets excluded as ice crystals form from pure water, which results in entrapped air bubbles in ice. The air bubbles increase the number of interfaces light has to go through. This would explain why light is more attenuated in frozen sand packs; however; not why images at frozen residual saturation appear even darker than images at frozen 100 % saturation. This observation warrants further investigation, however, the unequal darkening of frozen images between high and low saturations surprisingly did not prevent calculated ice and water volumes to be calibrated using the same single fit parameter. Nevertheless, the attenuation of light as the cell freezes can prove to be useful if one was interested in tracking the location of the freezing front (Appendix C). Finally, Figure 2.7a and 2.7b do not display completely straight lines due to edge effects in the original images, however the curves are smooth, indicating good homogeneity in the pack.

2.4 Conclusion

There is a need to investigate the distribution of ice in frozen soils at a high spatial resolution. Given the successful application of the light transmission method to investigate water distribution in unfrozen soils during laboratory experiments, this paper explored the application of the LTM on frozen soils. A thin flow cell was used to capture images of sand at various water and ice saturations. A total of 5 cells were packed, with 5 unfrozen tests and 3 frozen tests being completed. An image processing technique was used to calculate total water or ice volumes in the cell and generate saturation maps and profiles.

A single fit parameter was applied to both water saturation in unfrozen packs and to ice saturation in frozen packs. Known and calculated ice volumes were within 2 % over a range of different ice saturations in the cell. These results validate the use of the LTM in frozen soils for ice quantification. Further, the ability to calculate both water and ice content with a single fit parameter indicates that the calibration process can be performed during unfrozen experiments and then be applied to frozen experiments. This allows the calibration process to be completed in a matter of hours, rather than days.

Despite the fact that pure ice and water have the same refractive indexes, images from frozen tests showed more light attenuation than unfrozen tests. It is hypothesized that the extra attenuation of light in frozen sand packs is attributed to entrapped air bubbles created as ice formed from pure water, which increases the number of interfaces light has to go through. The attenuation of light as a sand pack freezes is helpful, as it not only helps to confirm whether a pack is frozen or not, but it also provides a means to track the position of the freezing front in a freezing cell in space and time.

In future research on unsaturated or saturated flow phenomena using the LTM, one should consider not to fill the cell completely when packing such that a space is left for the increase in volume when water turns to ice. This would allow a frozen I_s image to be obtained without compromising the tracking of water mass during drainage and without additional image cropping, which reduces visibility in the sand pack. Given the challenges with understanding permafrost hydrology behaviours in current conditions, let alone the changes occurring due to climate change, the LTM proves to be a valuable tool for studying these fascinating processes. The LTM has also been used to investigate wetting and nonwetting fluid saturations (i.e., water and non-aqueous phase liquids, respectively) in unfrozen porous media, and future research may consider testing the LTM for use in such studies in frozen soils.

2.5 References

Barnes, D., & Chuvilin, E. (2009). *Permafrost Soils.* Springer.

Belfort, B., Weill, S., Fahs, M., & Lehmann, F. (2019). Laboratory Experiments of Drainage, Imbibition and Infiltration under Artificial Rainfall Characterized by Image Analysis Method and Numerical Simulations. *Water*.

Conrad, S., Glass, R., & Peplinski, W. (2002). Bench-Scale Visualization of DNAPL Remediation Processes in Analog Heterogeneous Aquifers: Surfactant Floods and In Situ Oxidation Using Permanganate. *Journal of Contaminant Hydrology*.

Darnault, C., DiCarlo, D., Bauters, T., Jacobson, A., Throop, J., Montemagno, C., . . . Steenhuis, T. (2001). Measurement of Fluid Contents by Light Transmission in Transient Three-Phase Oil-Water-Air Systems in Sand. *Water Resources Research*.

Darnault, C., Throop, J., DiCarlo, D., Rimmer, A., Steenhuis, T., & Parlange, J. (1998). Visualization by Light Transmission of Oil and Water Contents in Transient Two-Phase Flow Fields. *Journal of Contaminant Hydrology*.

Davidson, M., Mumford, K., Mullins, N., & Calvert, M. (2022). Modification of a 3D Printer to Create Geologically Realistic Structures Used to Investigate Gas Migration Using the Light Transmission Method. *Vadose Zone Journal*.

de Grandpré, I., Fortier, D., & Sephan, E. (2012). Degradation of Permafrost beneath a Road Embankment Enhanced by Heat Advected in Groundwater. *Can. J. Earth Sci.*

Dobriyal, P., Qureshi, A., Badola, R., & Hussain, S. (2012). A Review of the Methods Available for Estimating Soil Moisture and its Implications for Water Resource Management. *Journal of Hydrology*.

Glass, R., Conrad, S., & Peplinski, W. (2000). Gravity-Destabilized Nonwetting Phase Invasion in Macroheterogeneous Porous Media: Experimental Observations of Invasion Dynamics and Scale Analysis. *Water Resources Research*.

Goit, J., Groenevelt, P., Kay, B., & Loch, J. (1978). The Applicability of Dual Gamma Scanning to Freezing Soils and the Problem of Stratification. *Soil Sci. Soc.*

Heller, A., Shi, L., Brenizer, J., & Mench, M. (2009). Three Dimensional Water and Ice Quantification using Neutron Imaging. *Springer*.

Mumford, K., Hegele, P., & Vandenberg, G. (2015). Comparison of Two-Dimensional and Three-Dimensional Macroscopic Invasion Percolation Simulations with Laboratory Experiments of Gas Bubble Flow in Homogeneous Sands. *Vadose Zone Journal*.

Niemet, M., & Selker, J. (2001). A New Method for Quantification of Liquid Saturation in 2D Translucent Porous Media Systems Using Light Transmission. *Advances in Water Resources*.

Oostrom, M., Dane, J., & Wietsma, T. (2007). A Review of Multidimensional, Multifluid, Intermediate-Scale Experiments: Flow Behaviour, Saturation Imaging, and Tracer Detection and Quantification. *Vadose Zone Journal*.

Orozco-Lopez, E., Munoz-Carpena, R., Gao, B., & Fox, G. (2021). High-Resolution Pore-Scale Water Content Measurement in a Translucent Soil Profile from Light Transmission. *Transactions of ASABE*.

Schroth, M., Ahearn, S., Selker, J., & Istok, J. (1996). Characterization of Miller-Similar Silica Sands for Laboratory Hydrologic Studies. *Soil Sci. Soc.*

Schroth, M., Istok, J., Selker, J., Oostrom, M., & White, M. (1998). Multifluid Flow in Bedded Porous Media: Laboratory Experiments and Numerical Simulations. *Advances in Water Resources*.

Selker, J., Steenhuis, T., & Parlange, J. (1989). Preferential Flow in Homogeneous Sandy Soils Without Layering. *American Society of Agricultural Engineers*.

Sills, L., Mumford, K., & Siemens, G. (2017). Quantification of Fluid Saturations in Transparent Porous Media. *Vadose Zone Journal*.

Sjoberg, Y., Coon, E., Sannel, A., Pannetier, R., Harp, D., Frampton, A., . . . Lyon, S. (2016). Thermal Effects of Groundwater Flow Through Subarctic Fens: A Case Study Based on Field Observations and Numerical Modeling. *Water Resources Research*.

Spaans, E., & Baker, J. (1995). Examining the Use of Time Domain Reflectometry for Measuring Liquid Water Content in Frozen Soil. *Water Resources Research*.

Tidwell, V., & Glass, R. (1994). X Ray and Visible Light Transmission for Laboratory Measurement of Two-Dimensional Saturation Fields in Thin-Slab Systems. *Water Resources Research*.

Van De Ven, C., & Mumford, K. (2018). Visualization of Gas Dissolution Following Upward Gas Migration in Porous Media: Technique and Implications for Stray Gas. *Advances in Water Resources*.

Van De Ven, C., Abraham, J., & Mumford, K. (2020). Laboratory Investigation of Free-Phase Stray Gas Migration in Shallow Aquifers Using Modified Light Transmission. *Advances in Water Resources*.

Walvoord, M., & Kurylyk, B. (2016). Hydrologic Impacts of Thawing Permafrost - A Review. *Vadose Zone Journal*.

Wang, C., Su, X., Lyu, H., & Yuan, Z. (2021). Remobilization of LNAPL in Unsaturated Porous Media Subject to Freeze-Thaw Cycles Using Modified Light Transmission Visualization Technique. *Journal of Hydrology*.

Werth, C., Zhang, C., Brusseau, M., Oostrom, M., & Baumann, T. (2010). A Review of Non-Invasive Imaging Methods and Applications in Contaminant Hydrogeology Research. *Journal of Contaminant Hydrology*.

Woo, M.-k. (2012). *Permafrost Hydrology.* Springer.

Zhang, Y., Wu, J., & Ye, S. (2021). Quantification of the Fluid Saturation of Three Phase of NAPL/Water/Gas in 2D Porous Media Systems Using a Light Transmission Technique. *Journal of Hydrology*.

CHAPTER 3 LNAPL SPILL IN FROZEN HETEROGENEOUS POROUS MEDIA

3.1 Introduction

Current permafrost terrains affect NAPL migration (Barnes and Chuvilin, 2009). The low hydraulic conductivities of permafrost soils, the presence of ice, the influence of seasonal freeze and thaw cycling, and the typically shallow active layers found in permafrost environments all impact the movement, storage, and exchange of surface and subsurface fluids in a manner not found in temperate soils (soils that do not experience deep freezing) (Barnes and Chuvilin, 2009; Walvoord and Kurykyk, 2016). In addition, climate warming is expected to modify the distribution of permafrost, leading to alterations in hydrologic conditions (Walvoord and Kurylyk, 2016), which will, in turn, affect NAPL migration. Thaw-activated groundwater flow will open up new transport pathways, leading to variations in terrestrial-to-aquatic exchanges of nutrients and contaminants (i.e., LNAPLs) and will pose new risks to Arctic water supplies, raising both human and ecosystem health concerns (McKenzie et al., 2021). Understanding NAPL behaviours in current and future permafrost terrain is essential for protecting the environment in a changing climate.

Permafrost is ground that is at or below 0 °C for at least two consecutive years. It used to be conceived as perennially frozen ground (Muller, 1943), but the permafrost definition is currently based on temperature and not the freeze-thaw state of water in the host medium (Woo, 2012). The active layer is the seasonally thawed surface layer of the ground in a permafrost area (Woo, 2012) (Figure 3.1).

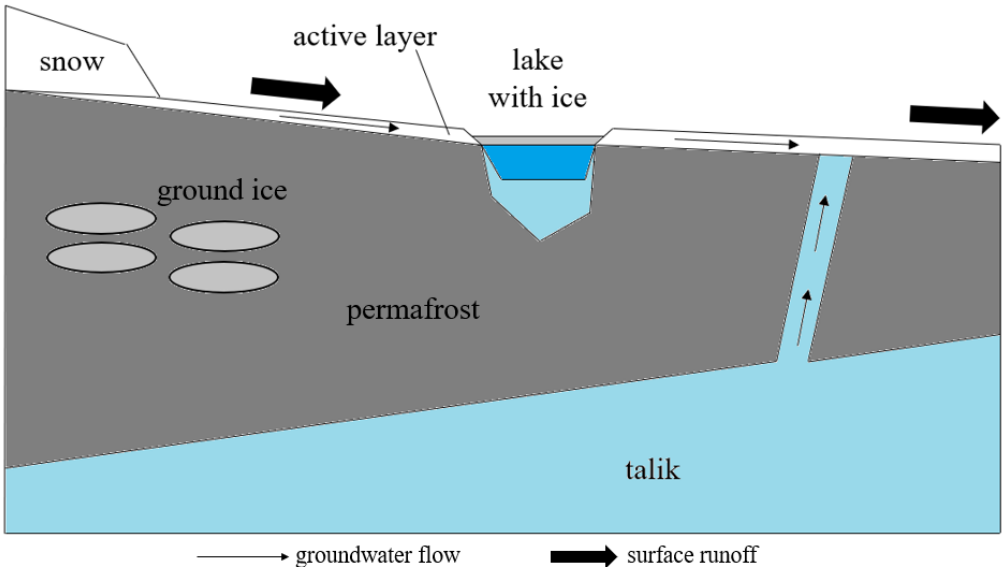

FIGURE 3.1: Conceptual model of water circulation in permafrost conditions, modified after Woo (2012).

To understand NAPL movement through freezing and frozen soils, it is useful to review the fundamental LNAPL migration principles through unfrozen soil (Barnes and Chuvilin, 2009). NAPLs with a density lower than water are called light non-aqueous phase liquids (LNAPLs). Following a spill, LNAPLs generally migrate down through a soil's partially saturated zone until they reach the top of the capillary fringe (Figure 3.2). The LNAPL distribution that accumulates in the subsurface is typically termed the 'source zone' of contamination, comprising both immobile residual LNAPL, trapped in pore space by capillary forces, and potentially mobile LNAPL, which exists as a continuous fluid across interconnected pores capable of migrating if provided a sufficient driving head (Rivett et al., 2014). The latter often manifests as a layer of LNAPL (e.g., oil or fuel) distributed across the capillary fringe interface due to the LNAPL buoyant nature (Rivett et al., 2014).

NAPL migration is very sensitive to heterogeneities and anisotropies of porous media hydraulic properties (Osborne and Sykes, 1986; Kueper and Frind, 1991; Poulsen and Kueper, 1992; Schroth et al., 1998). Horizontal bedding in the formation results in lateral spreading and retention at textural interfaces (Kechavarzi et al., 2008). Additionally, Poulsen and Kueper (1992) reported that an extremely heterogeneous distribution of NAPL residual can result from NAPL migration through sands exhibiting only a moderate spatial variability in permeability and capillary characteristics (i.e., mild heterogeneity). Based on results obtained from a field experiment conducted on an old prograding shoreline deposit, they noted that NAPL can migrate parallel to soil bedding and that certain laminations may or may not contain stringers of residual NAPL. Therefore, soil characterization is important for accurate predictions of NAPL movement in the vadose zone.

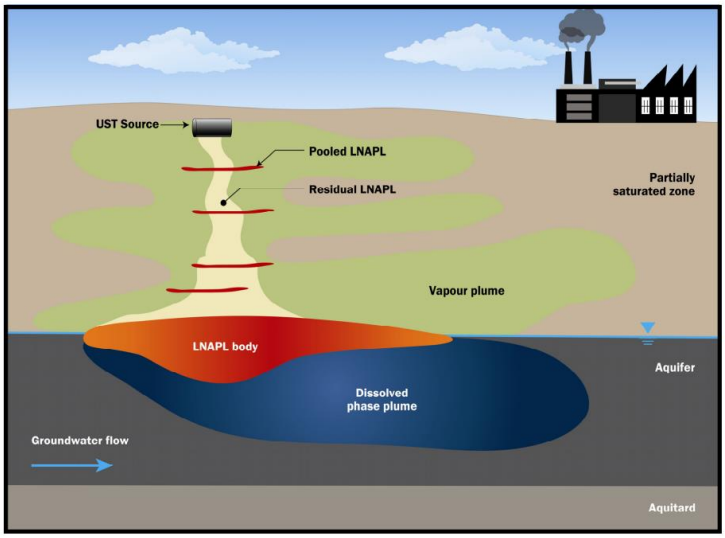

FIGURE 3.2: Conceptual model of LNAPL release in the subsurface in unfrozen conditions from Rivett et al. (2014).

Assuming that a porous medium is water-wet (water wets the solid surfaces), the wettability increases in the order air < NAPL < water (Leverett, 1941). Consequently, when all three fluids are present, the smallest pores are occupied by water, the intermediate-size pores are occupied by LNAPL, and the largest pores are occupied by air (Schroth et al., 1998). This concept is useful for

the prediction of NAPL behaviour in the vicinity of textural interfaces where variability in both permeability and water saturation (S_w) can occur (Schroth et al., 1998). For example, Schroth et al. (1998) demonstrated that LNAPL migrating in a fine-grained soil layer is diverted parallel to an interface with a layer of coarse-grained soil when both layers are at low water saturation (when S_w ~ 0, LNAPL is the wetting fluid and occupies the small pores, air is the non-wetting fluid and occupies the large pores, which causes LNAPL to be contained in the fine-grained soil layer). Further, Schroth et al. (1998) demonstrated that LNAPL is also diverted parallel to a textural interface in zones of high water saturations, however, in this case, rather than being diverted along the textural interface, LNAPL diversion occurs in the upper portion of the zone of high water saturation which supports the LNAPL. Schroth et al. (1998) demonstrated that only in zones of moderate water saturation does partial penetration of LNAPL into the coarse-grained layer occur (at the interface, water occupies the small pores and LNAPL is forced to move into larger pores than it previously occupied during vertical downward migration).

In freezing and frozen soils where water turns to ice, LNAPLs behave differently. First, LNAPL penetration rates were reported to decrease in frozen soils due to an increase in the viscosity with a decrease in temperature (Singh and Niven, 2013). In addition, using gravelly sands, Andersland et al. (1996) reported that dry unfrozen and frozen soils have similar hydraulic conductivities, however hydraulic conductivities decrease with an increase in ice content. Wiggert et al. (1997) performed tests to study the interaction between ice saturation and intrinsic permeability and reported that the permeability decreases nearly linearly with an increase in ice saturation. Consequently, LNAPL penetration rates also decrease with an increase in ice saturation (McCauley et al., 2002). In the extreme, high ice saturations may even result in a nearly impermeable ground surface, promoting surface spread (Barnes and Chuvilin, 2009).

Biggar and Neufeld (1996) packed a 30-cm high saturated silty sand soil column with a layer of diesel-contaminated soil placed on top and performed freeze-thaw cycles such that the top of the cell could freeze and thaw (to mimic an active layer), while keeping the bottom part of the cell permanently frozen (to mimic a permafrost table). After 8 freeze-thaw cycles, results showed considerable migration of diesel into the saturated uncontaminated soil subjected to cyclic freezing and thawing, however, the permanently saturated frozen soil showed no contamination. Ice lenses in the field have also been observed to be effective barriers to LNAPL vertical migration (Biggar et al., 1998). However, the literature does provide some evidence of the potential for LNAPL to move into small fissures and vertical cracks formed by thermal contraction in frozen saturated soils, suggesting that even a high ice saturation permafrost table can allow vertical LNAPL migration in certain conditions (Biggar and Neufeld, 1996; Biggar, n.d.; Biggar et al., 1998).

Ice acts as a solid in the ground, changing the pore geometry and capillarity of the soil (Barnes and Chuvilin, 2009). Barnes and Shur (2003) and Barnes and Wolfe (2008) investigated how pore ice impacts the migration of petroleum hydrocarbons (NAPL) by spilling 100 ml of colored NAPL in frozen laboratory soil flumes (at -5 ºC) packed homogeneously with respect to both grain size and water saturations. Two different sand grain sizes were used (coarse sand: grain size of 0.6 mm, and medium sand: grain size of 0.212 mm) at two different uniform water saturations (resulting in ice saturations of 26 % and 54 % once frozen) for a total of four tests. The tests conducted on the coarse sand showed that an increase in ice saturation can cause an increase in lateral movement of NAPL due to restricted or blocked pore space by ice (NAPL widths were 0.19 m at 26 % ice saturation, compared to 0.43 m at 54 % ice saturation). In addition, ponding of NAPL occurred at 54 % ice saturation after being introduced into the flume, but not at 26 % ice

saturation. The authors attributed the ponding effect to a decrease in permeability of the porous medium at higher ice saturation. Finally, the maximum depth of penetration was greater at 54 % ice saturation, which was attributed to the initial pressure head of NAPL created as it was introduced into the flume (it ponded) and a decreased amount of pore space available to retain NAPL causing deeper migration. As for the tests conducted on medium sand, NAPL widths were similar at both ice saturations (0.28 m at 26 % ice saturation, compared to 0.30 m at 54 % ice saturation), which Barnes and Wolfe (2008) attributed to clusters of ice-saturated pores being approximately the same size in both packs, but possibly more numerous at 54 % ice saturation. According to Barnes and Wolfe (2008), and Fourie et al. (2007), it is possible that infiltrating liquid water in frozen soils (or water rearrangement in this case as the cell was freezing) may be retained by capillary forces, which once frozen might create dead-end pores resulting in ice-saturated pore space and the formation of preferential pathways around the blocked pore space. Additionally, the same initial ponding behaviour occurred in the medium sand at 54 % ice saturation. Finally, penetration was less in tests conducted on medium sand, which Barnes and Shur (2003) attributed to a greater decrease of pore channel diameters in finer sand resulting in an increase in capillary pressure and associated NAPL lateral or restricted overall movement.

Investigating LNAPL movement and distribution in soils, under both frozen and unfrozen conditions is often done using laboratory flow cell experiments (Barnes and Shur, 2003; Oostrom et al., 2007; Barnes and Wolfe, 2008). To the author's knowledge, most laboratory experiments involving LNAPL migration in frozen soils to date were performed on frozen porous media with homogeneous grain distribution and water/ice contents. Those experiments were helpful in understanding the isolated effects of pore ice and freezing temperatures on LNAPL migration in different types of frozen homogeneous sands, however, in an attempt to reproduce more field conditions, there is a need to investigate the governing processes affecting LNAPL migration in frozen heterogeneous porous media. Further, the unique features and complex dynamics associated to permafrost terrains (Walvoord and Kurylyk, 2016) require LNAPL studies at high spatial resolution. Barnes and Adhikari (unpublished data) (as discussed by Barnes and Chuvilin, 2009) did perform an experiment to investigate petroleum migration into a frozen sand pack that contained a simple form of geological heterogeneity (a 1.3 cm thick fine-grained layer interbedded between coarse grain sand layers). For this investigation, the soil was thoroughly wetted by introducing water to the top of the flume, however water was allowed to drain through the sand layers (Barnes and Chuvilin, 2009). When water drainage ended (water in the pore space was held by capillary forces at some residual level, presumably with higher water content in the finer-grained layer), the flume was insulated on the sides and bottom and placed in a cold room at -5 ºC to induce a top-down freezing (Barnes and Chuvilin, 2009). Once frozen, colored jet fuel (JP2) chilled to -5 ºC was introduced to the top of the soil layer, and migration of the petroleum through the soil was tracked using time-lapse photography (Barnes and Chuvilin, 2009). The test was also repeated in the same manner, but in unfrozen condition. The authors reported that while NAPL was able to breach through the fine-grained layer in the unfrozen condition, it was not able to do so in the frozen condition. The fine-grained layer retained enough water, which once frozen, was sufficient to create an impermeable barrier. More controlled laboratory investigations on LNAPL migration in frozen soils are needed to study LNAPL dynamics in the presence of spatial variation of permeability, capillarity, and water/ice content characteristics.

Traditionally, the techniques used for NAPL saturation mapping for flow cell experiments conducted in unfrozen material are mostly limited to photon-attenuation methods such as gamma and X-ray techniques and photographic methods such as the light reflection, light transmission,

and multispectral image analysis techniques (Oostrom et al., 2007). Photographic methods such as light transmission do not require specialized equipment and are, therefore, low-cost methods (Niemet and Selker, 2001). They are non-destructive, non-invasive and can lead to quantitative measurements without inserting (m)any probes in the porous media (Belfort et al., 2019). Photographic methods also have advantages with respect to resolution in time and space. Utilization of digital cameras provides a nearly instantaneous high-density array of spatial measurements while sampling a large area (~0.1-1 m^2), as opposed to many other methods where long count times and/or small pointwise measurements (less than 1 cm^3) are typical (Niemet and Selker, 2001).

The light transmission method (LTM) is a good non-destructive and non-invasive photographic method for systems with rapid changes (Oostrom et al., 2007). The LTM has been used in a wide variety of two-dimensional (2D) laboratory studies to investigate water saturations in both stable and transient flow fields (Tidwell and Glass, 1994; Niemet and Selker, 2001; Orozco-Lopez et al., 2021), wetting and nonwetting fluid saturation (i.e., water and NAPL respectively) in porous media (Darnault, et al., 1998; Glass et al., 2000; Darnault, et al., 2001; Conrad et al., 2002; Zhang et al., 2021), and gas migration investigations (Van De Ven and Mumford, 2018; Van De Ven et al., 2020). To the author's knowledge, other than the results presented in Chapter 2 of this thesis where the LTM was adapted to quantify ice, the use of the LTM on frozen soils has been limited to one study. Wang et al. (2021) applied a modified version of the LTM to investigate the remobilization of LNAPL in unsaturated porous media subject to freeze-thaw cycles, however, LNAPL was spilled into the cell in the unfrozen condition and then was subjected to freeze-thaw cycles. Wang et al. (2021) did not use the LTM to track LNAPL movement through frozen soils.

Given the promising results of the LTM in frozen soils shown in Chapter 2, and the need to investigate LNAPL flow in frozen heterogeneous porous media at a high spatial resolution, there is an opportunity to continue testing the method for the investigation of LNAPL migration in frozen soils. This paper aims to demonstrate the use of the LTM in frozen soils to investigate LNAPL dynamics in the presence of pore ice and spatial variation of permeability and capillarity characteristics. Specifically, the objectives were to perform a macroscopic analysis of LNAPL migration in three different sand packs with various degrees of heterogeneity, analyse the spill migration in these packs in both unfrozen and frozen conditions, and further test the use of the LTM for such studies in frozen soils. These objectives were addressed using a series of experiments conducted in an intermediate scale 2D flow cell. For an experiment to be classified as intermediate scale, the flow cell has to be small enough for its boundary conditions to be controlled and allow small scale processes to manifest themselves at a larger scale so they can be studied and quantified (Oostrom et al., 2007).

3.2 Methodology

3.2.1 Experimental Set-Up

The LTM consists of placing a thin experimental flow cell between a light assembly and a digital camera to measure the intensity of light passing through the cell in space and time (Figure 3.3). The cell is filled with translucent sand, which allows light to be transmitted and provides a two-dimensional representation that is integrated over the pack thickness. The experimental set-up

used in this study is based on previous LTM studies by Lefebvre et al. (2022) (Chapter 2), Davidson et al. (2022), Tidwell and Glass (1994) and Niemet and Selker (2001), with minor modifications to the size so it could be moved in and out of a chest freezer. A 400 mm × 400 mm × 12 mm flow cell was built with two 6 mm glass panels sealed to an aluminum frame using a Neoprene O-ring (Figure 3.4). The total volume of the cell was 1,925 ml, which accounts for the small cavities at each port. The cell was equipped with six bottom ports allowing for water drainage and imbibition. Each bottom port was topped with a water-wet nylon net filter (Merck Millipore Ltd, 80 μm); a membrane that allowed water to go through while preventing sand and air from escaping the cell during water drainage and allowed the cell to be drained under vacuum using flexible transparent tubes linking the bottom ports to the water table control beaker. The 2D flow cell was back lit with a LED light panel assembly (Ledgo-LG-1200S) placed 150 mm from the cell and images were captured using a Canon Rebel T2i camera with a EFS 10-18 mm image stabilizer lens placed 505 mm in front of the cell (Figure 3.3). The camera was set-up to manual focus with the following settings: 1/10 as the shuttle speed, F16 as the aperture and ISO 1600. The settings were chosen manually in order to get high resolution images (0.01695 mm^2/pixel) and maintain consistency between images. Images in one experiment were captured using a GoPro (Hero 4) camera in frozen conditions in an attempt to prevent damage to the digital camera (Canon) while in the freezer, however, further testing showed that when the camera is thawed in a sealed plastic bag, which prevents moisture infiltration by condensation into the camera as it thaws, no damage occurs. Consequently, the Canon camera was used for the remainder of the experiments in both unfrozen and frozen conditions. The light, cell and camera were affixed in place on a mobile platform so the entire set-up could be placed in a freezer for frozen experiments. Black-out black curtains were also used to cover the set-up to prevent errors in light intensity measurements due to ambient light or light reflection from the sides of the freezer.

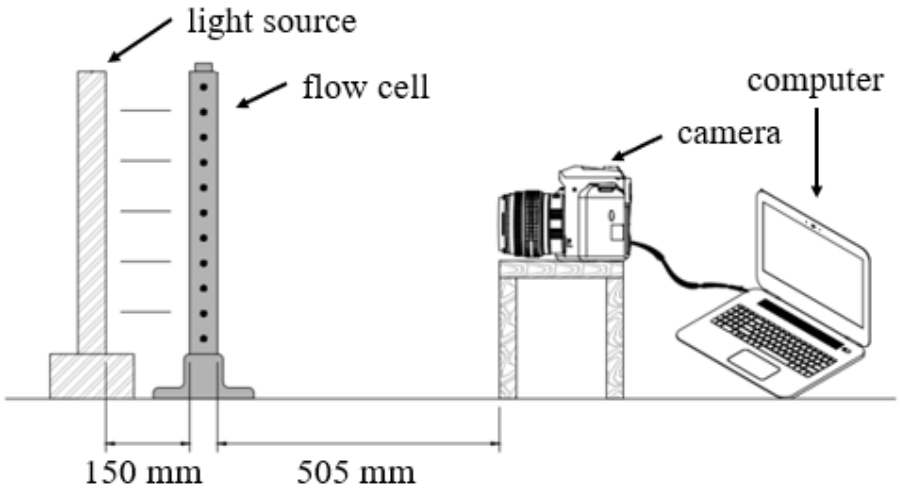

FIGURE 3.3: Light transmission experimental set-up including data acquisition system.

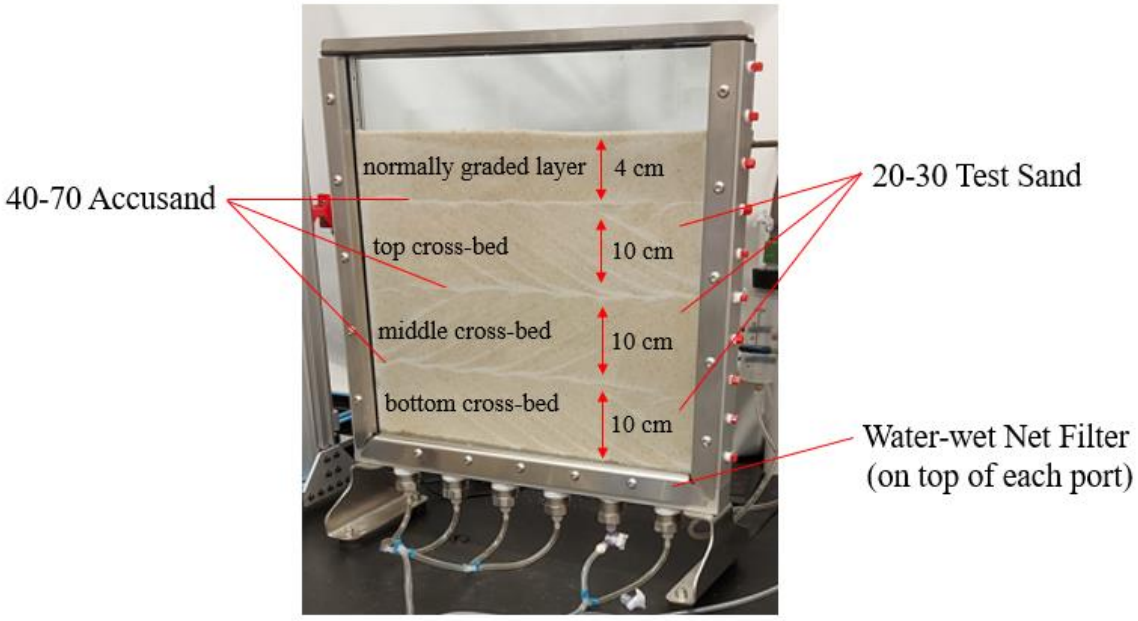

FIGURE 3.4: Flow cell details showing a heterogeneous sand pack.

3.2.2 Sand Packing

A total of six sand packs were used in this study. The sand packs consisted of three different configurations and each configuration was used in unfrozen or frozen conditions (single use per pack). The first configuration consisted of a homogeneous distribution (Figure 3.5a) and the second and third configurations consisted of a heterogeneous distribution (Figure 3.5b). Cross-beds were used for the heterogeneous distribution. Due to their fluvial origin, cross-beds are the dominant structure and the main source of anisotropy in permeability in sand reservoirs (Davidson et al., 2022). The packs were assembled using natural silica sands, which have been used in previous LTM studies (e.g., Van De Ven and Mumford, 2020; Davidson et al., 2022; Lefebvre et al., 2022 (Chapter 2)). Sands were combined in two different mixtures: ASTM 20-30 Test Sand (specific gravity of 2.65) with either 30-40 or 40-70 Accusand (specific gravity of 2.66). The first and second pack configurations consisted of a mixture of 80 % 20-30 and 20 % 30-40 silica sand (by mass) packed in both homogeneous and heterogeneous (cross-bedded) spatial distribution hereafter referred to as H3040 (which stands for homogeneous distribution with 20-30 + 30-40 mixture) and CB3040 (which stands for cross-bedded distribution with 20-30 + 30-40 mixture respectively). The third pack configuration consisted of 80 % 20-30 mixed with 20 % 40-70 silica sand (by mass) printed in cross-bedded spatial distribution hereafter referred to as CB4070 (which stands for cross-bedded distribution with 20-30 + 40-70 mixture).

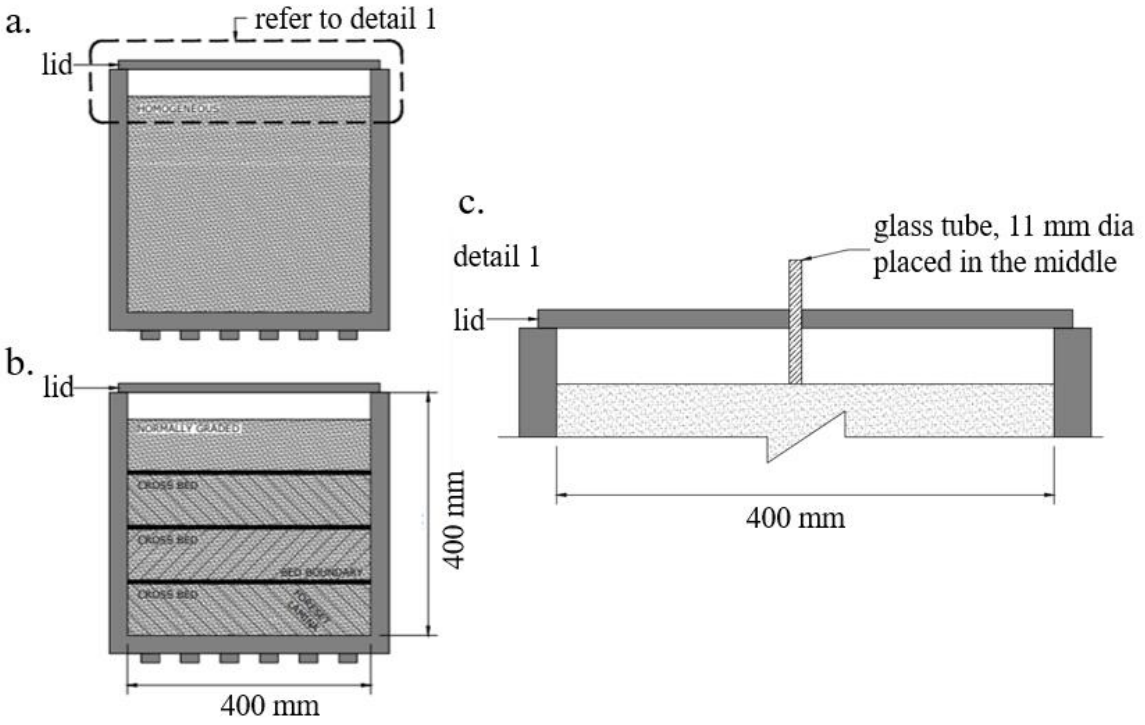

FIGURE 3.5: Flow cell set-up and sand pack configurations: (a) homogeneous sand pack (H3040), (b) heterogeneous cross-bedded sand packs (CB3040 and CB4070), and (c) spill tube set-up.

The name of each experiment combined the abbreviation of the pack with the suffix ‘’U’’ or ‘’F’’ to refer to unfrozen or frozen conditions, respectively (Table 3.1).

TABLE 3.1: List of tests performed in both unfrozen and frozen conditions including sand mixtures and packing configurations.

Coarser sand (sieve size)	Finer sand (sieve size)	Packing configuration	Unfrozen Tests	Frozen Tests
20-30	30-40	Homogeneous	H3040U	H3040F
20-30	30-40	Cross-bedded	CB3040U	CB3040F
20-30	40-70	Cross-bedded	CB4070U	CB4070F

Before packing, all sand mixtures were rinsed with deionized water to remove fines and dust. The sand mixtures were then oven dried for 24h at 110 °C. The homogeneous packs (H3040U and H3040F) were assembled using the wet pack method (otherwise called slurry packing), a technique involving oversaturating the soil with water before letting it settle at the bottom of the flow cell. A fitted funnel was used to facilitate the procedure. A rubber mallet was also used to vibro compact the sand as it was settling into the flow cell to promote consolidation. Using the wet pack method

resulted in a uniform, homogeneous saturated pack. The porosity of each pack was determined gravimetrically.

The cross-bedded packs for experiments CB3040U, CB3040F, CB4070U and CB4070F were assembled using dry sand and a modified 3D printer developed by Davidson et al. (2022). Generally, the 3D printer technique involves depositing sand in x (width) and z (height) directions in the cell to produce the desired heterogeneities in spatial distribution of the grains. Automating this process allows pack configurations to be reproduced at high accuracy, which is useful when comparing data from multiple controlled laboratory experiments. The x-axis and z-axis actuators of the 3D printer guide a sand hopper that contains a homogeneous sand mixture, which is consistently released through a feed tube during the print. Segregation of the sand through the feed tube and avalanching during deposition is used to create cross-beds separated by finer-grained boundaries. The heterogeneous sand packs consisted of three roughly 10 cm thick cross-bedded layers printed in a chevron pattern topped with a roughly 4 cm normally graded layer (Figure 3.4). A fine-grained layer was deposited on the cell side walls to prevent preferential LNAPL migration along the aluminum side walls. After each print, the packs were vibro compacted using a rubber mallet and CO_2 gas was injected through the bottom ports for 120 minutes (Masterflex, PMR1-010540, 1000 ml/min). Packs were then fully saturated through the bottom ports using degassed water applied using a peristaltic pump (Masterflex L/S 07528-30) (approximately two pore volumes) to displace and dissolve the CO_2. Water was applied until no residual gas bubbles were visible. Lastly, the packs were vibro compacted once again using the rubber mallet. The mass of dry sand used to assemble each pack was tracked to determine the porosity. All three pack configurations had a porosity of approximately 0.33.

3.2.3 Unfrozen and Frozen Experiments

Unfrozen experiments were performed at room temperature (~22 °C). To capture images of sand in frozen conditions, the entire set-up (light, cell, camera, and platform) was placed in a chest freezer (Frigidaire FFFC20M4TW, interior dimensions: 1702 mm wide, 546 mm deep, 635 mm high), at approximately -28 °C. The mobile platform was built out of wood painted in mat black and had reference markers to ensure that all pieces of equipment were always installed in the same location. The light was kept on at all times in the freezer including while the cell was freezing. Doing so prevented the cell from freezing too fast, which would allow for frost to appear on the glass surfaces. Silica beads were also found to help minimize the humidity level in the freezer, keeping frost formation under control. A temperature probe (Traceable 4000 90080-09) was inserted in the top portion of the cell at the conclusion of two tests to measure the temperature of the frozen pack. This was completed at the end of the tests to avoid disturbing the sand structure prior to, or during a test. With the light on, the cell temperature remained constant at -9 °C after a minimum of 18 h in the freezer.

3.2.4 Initial Water Conditions

The water table was dropped to 55 mm below the cell bottom using the water table control beaker to reach the desired pre-spill pack conditions (Figure 3.6). The water level in the cell was allowed to come to equilibrium overnight for a period of at least 12 h and the water drain valve was kept open for the duration of the experiment (including during the spill). Each pack configuration resulted in a unique water distribution (the top of the capillary fringe varied in height). In general, approximately 25 % of the cell was saturated, identified by the bright light

intensity, while the top 75 % of the cell was unsaturated, identified by the much darker light intensity (water-particle interfaces transmit more light than air-particle interfaces). Homogeneous (H3040) packs had a smooth capillary fringe, while cross-bedded packs (CB3040, CB4070) had a heterogeneous water distribution. Water distribution in heterogeneous packs is affected by fine-grained layers, which can retain more water and at greater elevations than coarse-grained layers. Water increases in volume by 9 % as it freezes. The volume increase can be seen in Figure 3.6d, 3.6e and 3.6f when comparing their capillary fringe heights with Figure 3.6a, 3.6b and 3.6c respectively. As seen in Figure 3.6, the different sand layers were more visually noticeable in CB4070 (Figure 3.6c and 6f) than CB3040 packs (Figure 3.6b and 3.6e). If CB3040 packs were not initially saturated and drained and were not back lit, they would look like homogeneous packs, and a similar soil mix might be qualified as such in the field. They were chosen for these experiments to see if a heterogeneous pack which might appear as homogeneous might have an influence on LNAPL migration in unfrozen conditions, and if the effects would be enhanced once frozen when water turns to ice. Results in these packs were compared to truly homogeneous packs as well as to evidently heterogeneous packs to observe the effects of spatial variation in grain distribution on LNAPL migration in both unfrozen and frozen conditions.

3.2.5 Chosen LNAPL, Spill and Tracking

The LNAPL used in all tests was heptane, a component of gasoline. Heptane was selected due to its low volatility at room temperature (6,133 Pa) and low freezing point (-90 °C). A single-component hydrocarbon rather than a hydrocarbon mixture, such as gasoline, was used to take advantage of known fluid properties (density, viscosity, interfacial tension). To enhance the visual contrast of heptane migrating through the cell, it was colored with hydrophobic Oil Red O dye at a concentration of 1 g of dye per l of heptane. Once the dyed solution was prepared, it was chilled in a refrigerator to approximately 2 °C (the refrigerator temperature was measured using a digital thermometer: Traceable 4000 90080-09).

A 6 g mass of heptane was rapidly spilled into the cell using a small glass funnel and a glass tube inserted at the top of the cell (Figure 3.5c). The LTM was used to track the progression of the spill in space and time. Images were captured every 5-10 s for the first 30 min after which the time intervals were adjusted based on the spill progression. Each spill was tracked for a minimum period of two days; however, each test was considered terminated when the spill had reached equilibrium and stopped progressing. Of note, for the volume of heptane used in these experiments and the size of the flow cell, most of the LNAPL was contained in the unsaturated portion of the cell. In unsaturated experiments where all three fluids are present (air, NAPL, water), air is non-wetting to both NAPL and water and therefore, occupies the largest pores of the cell located between the glass surfaces and the grains, which prevents NAPL preferential flow against the glass (NAPL will flow in intermediate size pores). Following each test, observations were made on both sides of the cell to confirm that no preferential flow occurred against the glass surfaces.

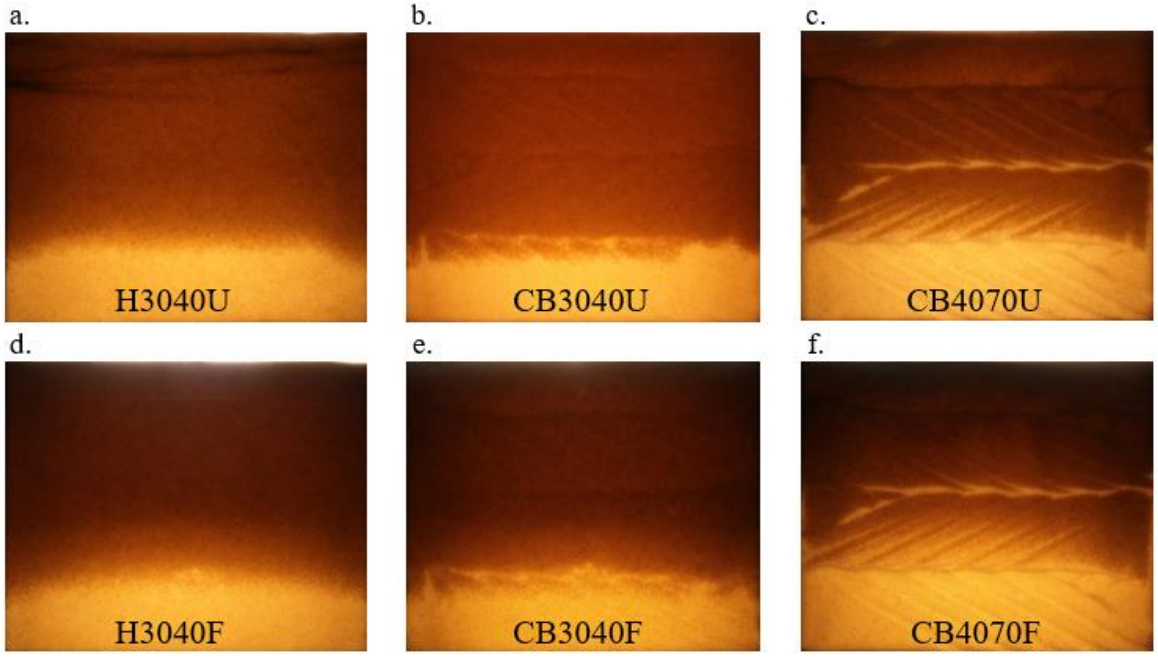

FIGURE 3.6: Initial water or ice saturation conditions (pre-spill) for each pack configuration in unfrozen conditions (a) H3040U, (b) CB3040U and (c) CB4070U as well as in frozen conditions (d) H3040F, (e) CB3040F, (f) CB4070F.

3.2.6 Image Processing

Nine images were selected per test at similar time intervals for comparison between tests in space and time. Each image was converted from RGB to HSV in MATLAB and hue ranges were used to extract the LNAPL coordinates in each image. Each hue range was based on a whole test and was applied to all nine images selected for that test (Table 3.2). Of note, the full range of both saturations and values were used (0 to 1). Dilation and erosion filters were applied to the binary images obtained from the hue filtration step to reduce noise. All binary images were then given a colour and were stacked on top of each other to produce spill maps. Coordinates in the binary images were also used to measure the LNAPL spill depth, total width, and maximum width over time.

TABLE 3.2: Hue* ranges used per test to extract spill coordinates from selected images.

Test	Hue (min)	Hue (max)
H3040U	0.978	0.030
H3040F	0.940	0.033
CB3040U	0.952	0.037
CB3040F	0.940	0.039
CB4070U	0.973	0.037
CB4070F	0.977	0.026

*Hue is given a value from 0 to 1 for image processing in MATLAB.

3.3 Results and Discussion

3.3.1 Captured Images

A total of six spills were performed in three different sand pack configurations used in both unfrozen and frozen conditions, and the LNAPL spills were tracked using hue (i.e., red colour). Example spill images are shown in Figure 3.7 for test CB4070U. Figure 3.7 shows that LNAPL migration was very sensitive to geological heterogeneities. Horizontal spreading occurred when the spill reached the first capillary barrier (the interface above the top cross-bed) (Figure 3.7c), however LNAPL built enough pressure to break through that barrier. Once in the top cross-bed LNAPL initially traveled preferentially in small pores following the inclined bedding layers at low water saturation. As the water saturation increased in the fine-grained layers with increasing depth (to moderate water saturation), LNAPL was forced to move into larger pores than it previously occupied and partially penetrated the coarser sand layers below the inclined fine-grained layers it previously occupied. As water saturation increased further in the inclined fine-grained layers, LNAPL was completely diverted along the interfaces supported by the fine-grained layers at high water saturation (Figure 3.7d). LNAPL reached the second capillary barrier (the interface above the top of the second cross-bed) (Figure 3.7e) and went through that barrier despite the high water content. LNAPL then shifted direction due to the chevron pattern of the cross-beds (and the cell perimeter capillary barrier made of fine grains preventing LNAPL from hitting the cell side wall) and reached the top of the capillary fringe at which point it induced water drainage (likely due to a combination of NAPL-water drainage and a decrease in the air-water interfacial tension) (Figure 3.7f, 3.7g). LNAPL then pooled in zones of partially drained coarse-grained layers (Figure 3.7h). Apart from the residual LNAPL saturations it left behind, LNAPL eventually completely pooled in drained layers of coarse sand (Figure 3.7i). Spill progression image sets were made for all 6 tests and are included in Appendix G.

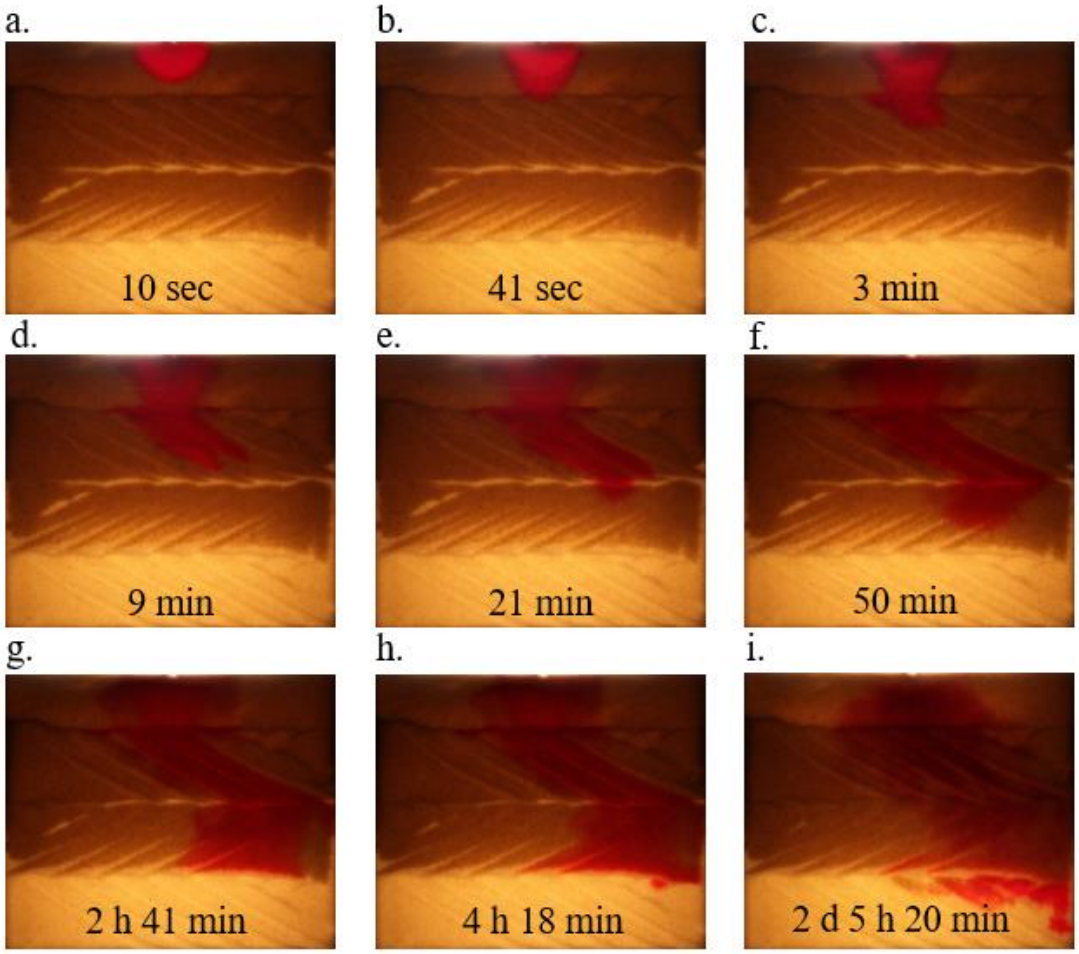

FIGURE 3.7: Test CB4070U images tracking spill progression in space at (a) 10 sec, (b) 41 sec, (c) 3 min, (d) 9 min, (e) 21 min, (f) 50 min, (g) 2 h 41 min, (h) 4 h 18 min and (i) 2 d 5 h 20 min.

3.3.2 LNAPL Distribution during Migration

Spill maps were created to visualize the shape of each spill in space and time in a single frame and facilitate comparisons between pack configurations in unfrozen and frozen conditions. Spill maps for the 6 tests are shown in Figure 3.8, from which several observations and comparisons can be drawn. As seen in Figure 3.8, spills in the unfrozen conditions for H3040U (Figure 3.8a) and CB3040U (Figure 3.8b) were very similar. The difference in grain sizes used in CB3040 packs was not sufficient to have a significant influence over LNAPL flow, which suggests that the pore sizes were somewhat consistent throughout the packs despite the cross-bed configuration in CB3040. In unfrozen conditions, the spills in H3040U and CB3040U packs slightly differed once they hit the top of the capillary fringe. H3040U had a smooth capillary fringe (Figure 3.6a), which facilitated lateral spreading of LNAPL (Figure 3.8a). CB3040U had layers of fine-grained sand, which retained water, and partially drained layers of coarse-grained sand (Figure

3.6b), which created a zone where LNAPL could pool once it hit the top of the capillary fringe (Figure 3.8b). Consequently, in CB3040U, LNAPL did not spread as much as in H3040U once it hit the capillary fringe. The fact that LNAPL migrations were similar in H3040U and CB3040U in zones of residual water saturations but differed once LNAPL hit the top of the capillary fringe indicates that the heterogeneity in water content in the cell is just as important as the heterogeneity in grain distribution. Nevertheless, the spills in H3040U and CB3040U were similar enough such that the CB3040U pack could be classified as homogeneous (since the stratification is barely visible to the naked eye without contrast enhancement) without compromising predictions of LNAPL spill extent. Classifying CB3040U as homogeneous may even result in a conservative approach since the spill in CB3040U might not spread as much as anticipated once it hits the capillary fringe.

In frozen conditions, the spill in H3040F (Figure 3.8d) and CB3040F (Figure 3.8e) were also similar, however, the differences are more pronounced than their unfrozen counterparts. First, the comparison between the proximity of the spill contours indicates that the penetration rate was much slower in CB3040F than H3040F. Second, while the effects of the heterogeneity in CB3040F were minimal at residual ice saturation (the top portion of the pack), they were not once LNAPL reached the capillary fringe. The ice froze in a manner that facilitated LNAPL spread in the direction of the cross-beds (i.e., from widths 0 to 100 mm and from depths 180 to 270 mm in Figure 3.8e), which suggests that there might have been enhancement of the effects of heterogeneity in CB3040F in zones of high ice saturations only and that classifying the soil as homogeneous in frozen conditions may lead to erroneous predictions of LNAPL migrations (unlike in unfrozen conditions). Of note, as seen in the original pictures of the spill in CB3040F (Appendix G, Figure G.5), LNAPL traveled on both sides once it hit the top of the capillary fringe, however most of the migration occurred in the direction of the cross-beds (left side). The hue technique artificially enhanced this process, however, the conclusion remains the same. Future attempts to quantify LNAPL using the LTM should look into reducing the redness of the packs before a spill by playing with the camera settings to further enhance contrast between the coloured LNAPL spill and the sand pack. Another solution worth looking into would be to use a blue dye. This would further simplify the hue technique and will prevent certain processes from being overpredicted.

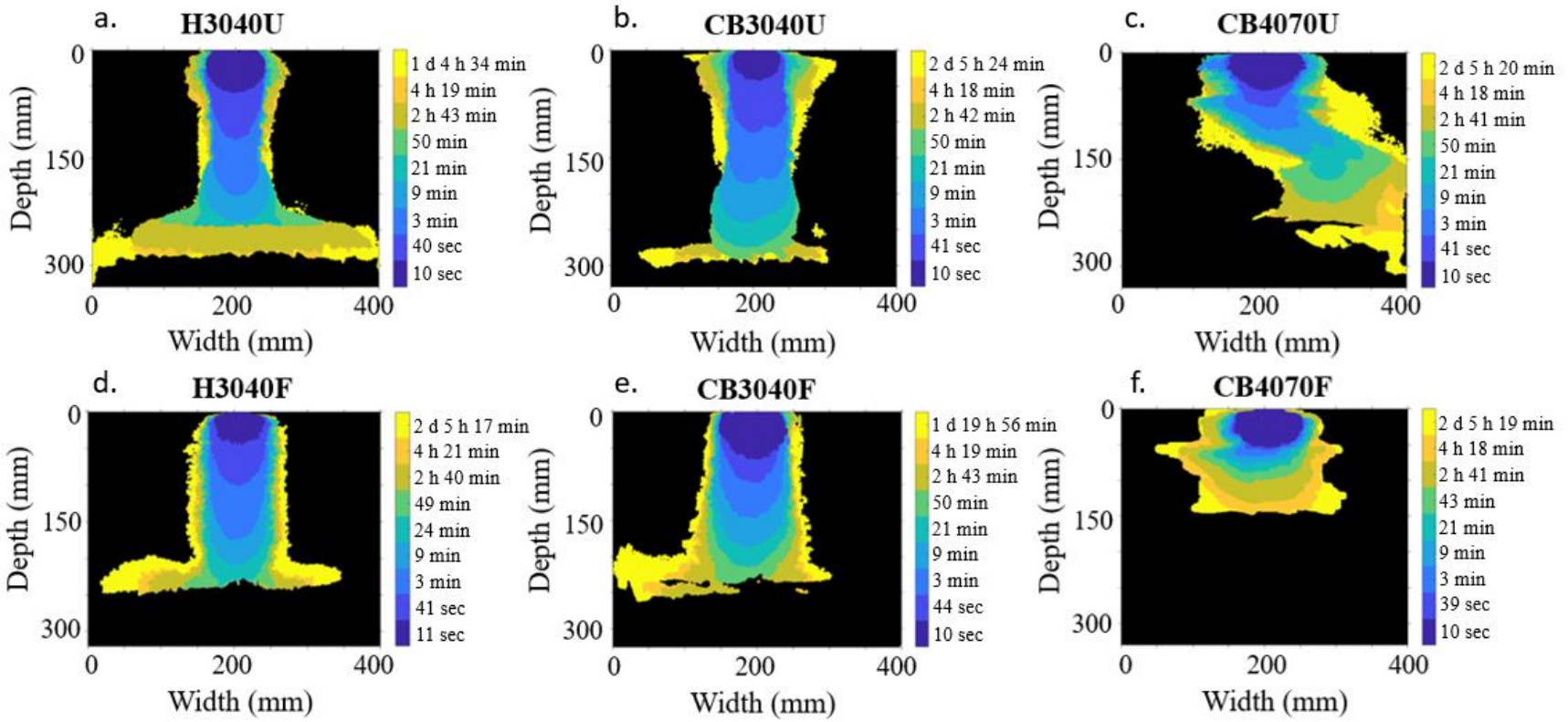

FIGURE 3.8: Spill progression map in space and time for all tests (a) H3040U, (b) CB3040U, (c) CB4070U, (d) H3040F, (e) CB3040F and (f) CB4070F.

The spills in the unfrozen and frozen CB4070 packs (Figure 3.8c, 3.8f) migrated very differently than the spills in the H3040 (Figure 3.8a, 3.8d) and CB3040 packs (Figure 3.8b, 3.8e) . The spill in CB4070U (Figure 3.8c) was very sensitive to the stratification (cross bedding) of the pack, including in zones of residual water saturation. The packing pattern and chevron style fine-grained layering was selected for these tests to encourage redirection of the spill to the middle of the flow cell and not pool on the side walls. However, an inclined bedding in the field would result in LNAPL migration far away (both horizontally and vertically) from the source, which is consistent with observations made by Poulsen and Kueper (1992). Additionally, horizontal capillary barriers made of fine-grained sand between beds caused LNAPL to spread laterally before pushing through them, at both residual water saturation (1st capillary barrier) and 65 % water saturation (2nd capillary barrier) (the water saturation in the fine-grained layer was estimated based on Schroth et al., 1996 and the height above the water table). In a similar manner to the spill in CB3040U, the spill in CB4070U ended up pooling in partially drained zones of coarse-grained sand.

The spill map for the final test, CB4070F, is shown in Figure 3.8f. As seen in the spill map, this test is noticeably different than the previous five, whereby the spill did not penetrate the second capillary barrier. Similarly to the spill in CB4070U, the spill in CB4070F also followed the inclined bedding of the pack, however, there was an additional increase in lateral spreading. The spill did not follow the cross-beds as precisely as it did in the unfrozen conditions, which is likely the result of partial restriction of pore space by ice and increased viscous forces due an increase in heptane viscosity at lower temperature. Generally, buoyancy and capillary forces are dominant. However, studies have reported that LNAPL movement can also be affected by viscous forces (which stabilize the effects of capillary forces) in addition to being directed by the particular structural and hydraulic properties of the porous medium when NAPL flows fast enough such that NAPL viscosity is high (Ewing and Berkowitz, 1998; Lenormand and Touboul, 1988; Frette et al., 1992). While there may have been an enhancement of the effects of the cross-beds at high ice saturation in CB3040F, the effects of the cross-beds seen in unfrozen conditions (in CB4070U) were diminished in frozen conditions (in CB4070F). However, the heterogeneity still played a significant role in LNAPL migration, since LNAPL did not breach through the second capillary barrier, which is similar to Barnes and Adhikari's experimental results (as reported in Barnes and Chuvilin, 2009). This indicates that even a slim layer of fine-grained sand (< 1 cm thick in this experiment) with high ice saturation (approximately 71 % ice content in this test based on the estimated 65 % water content) can be impermeable, preventing further LNAPL vertical migration and promoting lateral spreading. The impact of one such thin layer on LNAPL migration is high yet could easily be missed in the field as one could drill through it without knowing or seeing it when sampling the ground. Furthermore, even if a fine-grained layer is properly identified, measuring the sample layer moisture content can be challenging. For example, if a 100 mm thick soil sample (with a fine-grained layer in the middle) was analysed using a direct moisture content measurement method, such as the gravimetric method, it would result in an averaged water (or ice) content over the entire sample, rather than accurately attributing most of the water (or ice) content to the fine-grained soil layer (since the method disturbs the sample). Such results would be misleading and would minimize the impact of the thin fine-grained layer at high ice saturation, which would lead to erroneous predictions of NAPL migration.

3.3.3 Depth and Width of LNAPL Migration

The six test spills were also analysed by plotting the depth of LNAPL migration over time. Figure 3.9a shows the final spill migration image for CB4070F, with Figure 3.9b showing the incremental spill depth of CB4070F versus time. Highlighted across Figure 3.9a-b are the 3 capillary barriers within the cell. As previously discussed, in CB4070F, LNAPL did not penetrate the second capillary barrier, and is stalled from further penetration from 10^4 s onwards. Figure 3.9c plots migration versus time for all six tests. In all cases, the unfrozen conditions migrated to greater depths than their frozen counterparts. In unfrozen conditions, the LNAPL spills induced water drainage once they hit the top of the capillary fringe, allowing deeper penetrations of LNAPL in the cell. Once water turns to ice, drainage is not possible, so the spills in frozen conditions were contained to higher heights in the cell (most prominent in CB4070F where the spill did not pass the second capillary barrier). Previous studies (e.g., Biggar and Neufeld, 1996; Biggar, n.d.; Biggar et al., 1998) suggest that LNAPL penetration can occur in high ice saturation layers due to cracks or fissures formed by thermal contraction, however, this phenomenon did not occur in this study likely because the cell only went through one freezing cycle before each spill in frozen conditions.

The penetration rates of the spills in frozen conditions were lower than in unfrozen conditions, and the decrease in penetration rate was enhanced with an increasing degree of heterogeneity (Figure 3.9c). Layered systems increased lateral spreading, reducing the penetration rate. The additional decrease in penetration rate in frozen conditions is likely the result of a combination between an increase of the LNAPL viscosity at freezing temperatures and partial blockage of pore space by ice, which decreases the LNAPL permeability. The decrease of the penetration rate due to an increase in viscosity is consistent with the literature (Singh and Niven, 2013). A decrease of the penetration rate due to partial blockage of pore space by ice is also consistent with findings from Barnes and Shur (2003). In Figure 3.9c, the curve of the spill in H3040U shows a bump around depth 250 mm. This bump is the result of an air bubble in the draining tube, which temporarily prevented water drainage. It caused LNAPL to prematurely spread laterally rather than induce water drainage and further vertical migration. The air bubble was removed during the experiment, and water drainage continued resulting in a final depth that is consistent with other unfrozen experiments. When neglecting the bump, the depth over time curves between H3040U and CB3040U are very similar, except for the final depth. The depth over time curves between H3040F and CB3040F are also similar, but the spill in CB3040F migrated at a slower rate and ended up deeper. As for the spill in CB4070U, it ended up being the slowest unfrozen spill (penetration rate), however, it was also the deepest unfrozen spill. The spill in CB4070F was considerably slower than all other spills and ended up being the shallowest spill (Figure 3.9c).

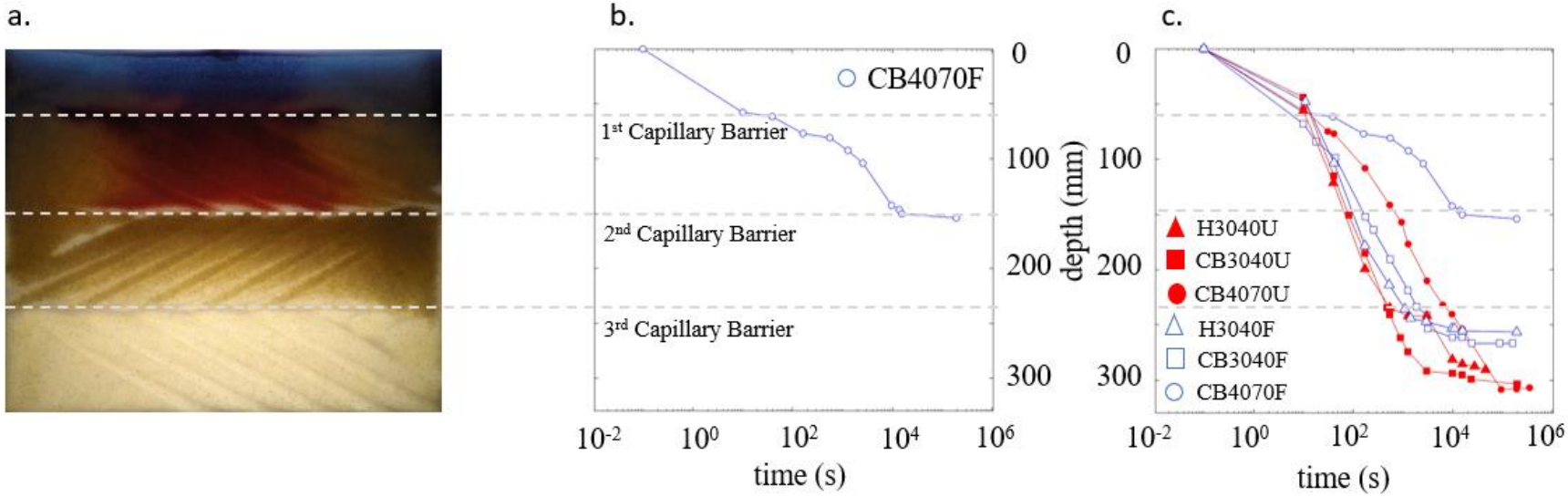

FIGURE 3.9: Depth versus time for all spills with (a) final spill image in CB4070F showing the position of the capillary barriers in the cell, which are extended in (b) the depth versus time for CB4070F and (c) the depth versus time for all six tests.

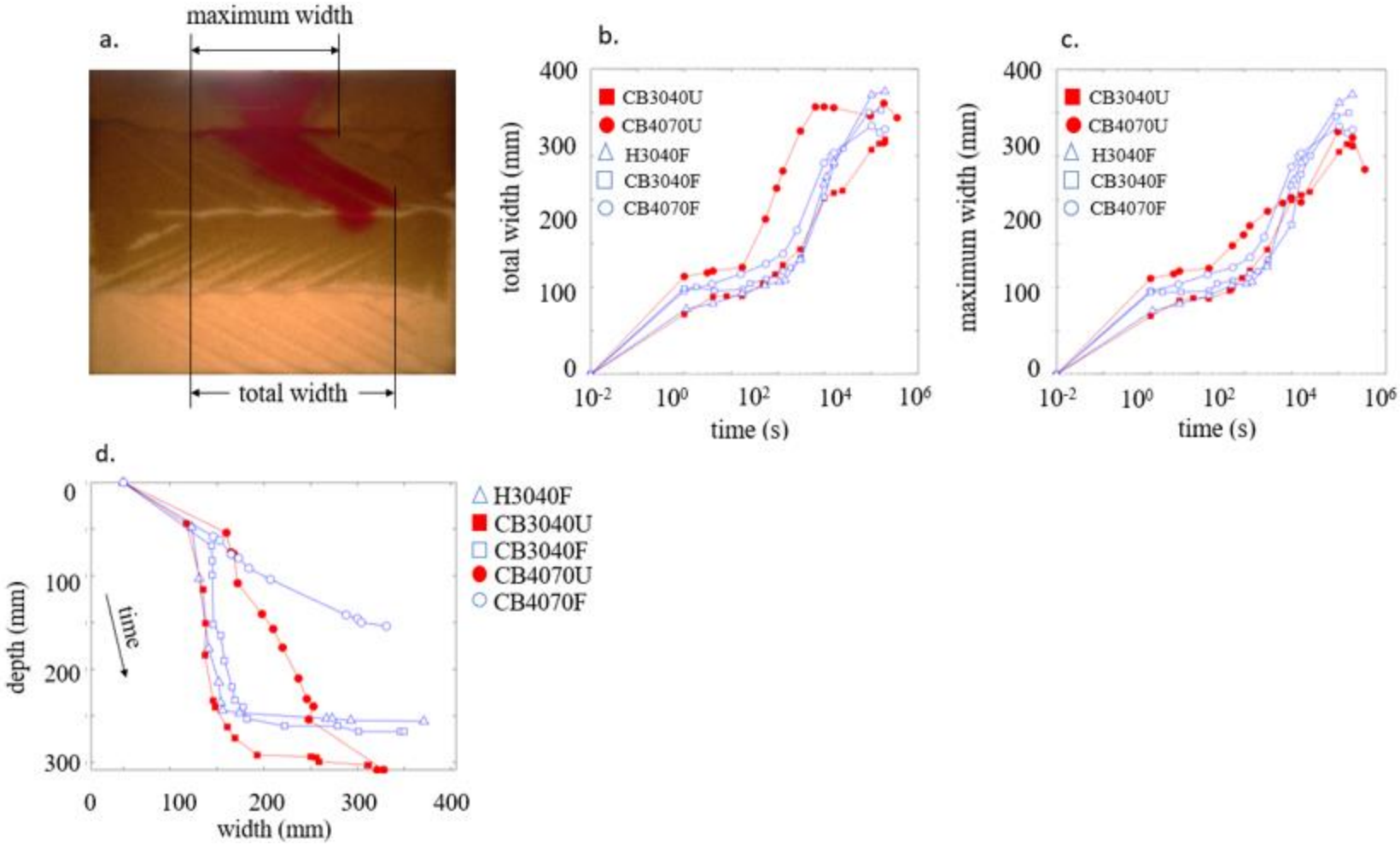

FIGURE 3.10: Width versus time for all spills with (a) an image from the spill in CB4070U to define total and maximum width, (b) total width versus time for all tests, (c) maximum width versus time for all tests and (d) depth versus maximum width for all tests.

Pore ice causes lateral spreading of LNAPL (Barnes and Shur, 2003; Singh and Niven, 2013). It is, therefore, useful to plot width versus time for all spills (Figure 3.10a-c). For the purpose of this analysis, total width (Figure 3.10a) refers to the total horizontal footprint of the LNAPL spill over the entire depth of the LNAPL distribution. The maximum width (Figure 3.10a) refers to the maximum width at any one particular depth. Further, because LNAPL migrates at different rates in unfrozen and frozen conditions, it is also useful to plot depth versus maximum width to analyse the maximum spill widths for a same depth in both unfrozen and frozen conditions (Figure 3.10d). The air bubble artificially affected the width of the H3040U spill and is therefore disregarded for the spill width analysis.

When comparing total widths between unfrozen and frozen spills, total widths were similar in CB3040U and CB3040F for the majority of the test, however, at the end, the CB3040F spill ended up wider (Figure 3.10b). When comparing total widths in CB4070U and CB4070F, the total footprint of the spill was greater throughout in CB4070U. When comparing maximum widths between unfrozen and frozen spills, LNAPL maximum widths were greater for a same depth in frozen conditions in both CB3040 and CB4070 pack configurations (Figure 3.10d). After the migration stopped, the spill in CB3040F ended up wider (maximum width) than in CB3040U by approximately 40 mm, however, the spill in CB4070F was only slightly wider (maximum width) than in CB4070U (10 mm) (Figure 3.10c, 3.10d). Those results demonstrate that while a LNAPL spill may migrate as a wider mass in frozen conditions, it does not necessarily mean that the total footprint will be greater (i.e., the total footprint in CB4070U was greater than in CB4070F).

When comparing spills in CB3040U and CB4070U, it was observed that a higher degree of heterogeneity resulted in more lateral spreading, for both total width (Figure 3.10b) and maximum width (Figure 3.10c, 3.10d), even in this experiment where the spill width in CB4070U was constrained by the size of the cell and the sand pack configuration (the spill would spread more laterally in the field). This is consistent with the increase in lateral spreading of LNAPL observed in layered systems reported by many researchers (e.g., Schroth et al., 1998). In frozen conditions, a higher degree of heterogeneity also resulted in more lateral spreading (Figure 3.10b-d), however, once LNAPL reached the top of the capillary fringe, the spills were wider in more homogeneous conditions (CB3040F, H3040F) due to the smoother capillary fringe promoting lateral spreading. NAPL migrating as a wider mass in CB3040F (almost homogeneous) is consistent with findings from Barnes and Shur (2003), who suggested that lateral spreading can occur as a result of blockage of pore space by ice. However, because lateral spreading also occurred at residual ice saturation, it is hypothesised that viscous forces affected the spill migration as well.

3.3.4 Observation of Halo in Frozen Tests

An unexpected observation was repeatedly made in all frozen tests in this study. As early as 30 min after the initial spill, a region of higher light intensity on the perimeter of the LNAPL distribution was seen. This ‘halo’ effect then remained throughout the test, following the migration pattern of the LNAPL. The halo was visible in all sand pack configurations; however, it was more pronounced in the homogeneous sand packs. To the author’s knowledge, there is no other study that has identified this halo effect during an LNAPL spill in frozen soils, which is likely driven by the testing methodology, rather than the absence of the halo. Shown in Figure 3.11 are two images captured during an additional spill test performed in a H3040F pack. The cell images are split in half and placed side by side such that the left side of Figure 3.11 shows an LTM image, and the right shows a front lit image. The halo is evident in the LTM image, but almost imperceptible in

the front lit image. This suggests that the halo was likely present in previous studies, though undetected using front lit images.

FIGURE 3.11: Difference between back lit (left side) and front lit (right side) images.

The halo was originally thought to be caused by water rearrangement in the cell (the heptane chilled to 2 ºC would have melted the ice and pushed it outside the spill area) even though the halo size appeared considerable in comparison to the amount of water that would be available for displacement by LNAPL in zones of residual water saturation. For the additional spill performed (shown in Figure 3.11), the heptane was chilled to -28 ºC before being spilt into the cell. The halo was still present, which suggested that any water rearrangement would have come from unfrozen water content in the frozen cell. Unfrozen water content in frozen soil has been reported in multiple studies (Anderson and Morgenstern, 1973; Tice et al., 1976; Andersland and Anderson, 1978; Van Everdingen, 1990; Konrad & McCammon, 1990). After investigating intensities of the H3040F pack in the unfrozen condition (pre-spill), frozen condition (pre-spill), and thawed condition (post-spill), there were no indications that water rearrangement occurred in the cell since the intensities in the thawed condition (post-spill) matched the intensities in the unfrozen condition (pre-spill) (Appendix H). However, the image was captured once the cell was completely thawed so it is possible that the moving unfrozen water drained as the cell thawed, which would prevent its observation at the time of the image capture. In addition, the halo intensities in frozen images increased up to a point where they were the same as the intensities of a thawed cell (intensities are darker in frozen sand packs, see more details in Chapter 2), further suggesting that the halo might be water, not ice. Since quantifying water content in the cell was outside the scope of this study, this hypothesis requires further investigation.

Dye separating from the heptane was investigated in case the halo was the result of a reduction in dye solubility at low temperatures resulting in the migration of undyed heptane. To test this hypothesis, a solution of dyed heptane was chilled to approximately -28 °C in a transparent glass beaker (by adding it to the freezer away from the lamp, and outside the curtain enclosure) and after confirming that no dye settled or separated during a period of 12 h, the solution was spilled into the cell. The halo still appeared, thus concluding that the halo was not due to dye

separating from the heptane. This also confirmed that there were no impacts on hue ranges used to extract the LNAPL spill contours. Should the halo phenomenon be a relevant process in one's study, it would reinforce the use of the light transmission method to see it happening in the first place.

3.3.5 Towards an Improved Conceptual Model of LNAPL Migration in Frozen Soil

The combination of previous laboratory (Biggar and Neufeld, 1996; Schroth et al., 1998; Barnes and Shur, 2003; Barnes and Wolfe, 2008; Kechavarzi et al., 2008; Barnes and Adhikari, unpublished data, as reported in Barnes and Chuvilin, 2009) and field (Poulsen and Kueper, 1992; Biggar et al., 1998) studies with the results of the experiments presented here provides an opportunity to improve the conceptual model of LNAPL migration in frozen soil, particularly in relations to differences between unfrozen and frozen conditions and the effects of heterogeneity (Figure 3.12).

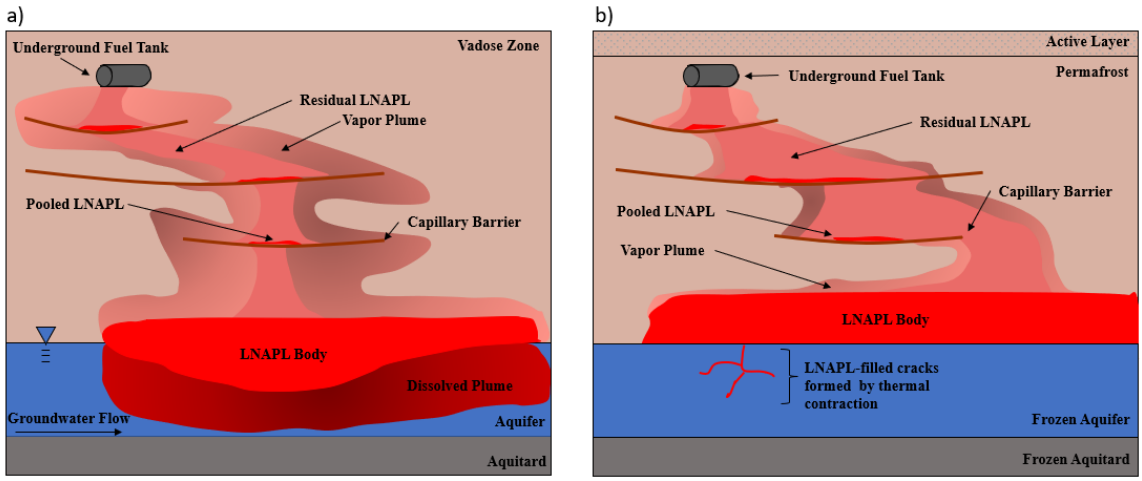

FIGURE 3.12: Conceptual model for LNAPL migration in (a) temperate region terrain and (b) permafrost terrain.

LNAPL migration in permafrost terrain is expected to be sensitive to both geological and water/ice content heterogeneity. In these experiments, LNAPL was able to penetrate finer layers (horizontal or cross-bedded) at lower water saturations but not those at higher saturations when frozen. Frozen capillary barriers cause lateral spreading of LNAPL even at ice saturations that do not prevent vertical migration. A frozen capillary barrier that can prevent vertical migration may not prevent vertical migration when thawed, even at high water saturations. Furthermore, LNAPL is expected to migrate as a wider mass in frozen conditions due to an increase in the LNAPL viscosity at low temperatures and partial blockage of pore space by ice. In frozen conditions, a wider mass of residual is also expected, but due to a decrease in the vapour pressure at lower temperatures, the LNAPL vapour plume is expected to be thinner. Once LNAPL reaches an unfrozen capillary fringe, LNAPL induces water drainage and pools at elevations lower than the original top of the capillary fringe, but that drainage does not occur in frozen conditions and all LNAPL pools above the capillary fringe, unless cracks formed by thermal contraction are present.

Because of these differences in response to the geological and water content heterogeneity, LNAPL is generally expected to migrate as a wider mass in frozen soils and its distribution is expected to be shallower in frozen soils than in unfrozen soils.

3.4 Summary and Conclusions

Permafrost affected regions present additional complexities affecting LNAPL migration. It is essential to understand the effects of such complexities to engineer effective remediation plans. It involves understanding the LNAPL dynamics in frozen soils containing spatial variation of permeability, capillarity, and water/ice content characteristics. Given the promising results of the light transmission method (LTM) in frozen soils shown in Chapter 2, and the need to investigate LNAPL flow in frozen heterogeneous porous media at a high spatial resolution, the LTM was tested for the investigation of LNAPL migration in frozen soils. LNAPL behaviour was investigated in three different sand pack configurations in both unfrozen and frozen conditions, for a total of six tests. Many observations made in this study agreed with previous findings from other researchers working on LNAPL migration in frozen soils, however, findings also help further understanding LNAPL migration in frozen soils.

Results showed that heterogeneity in water content is as important as heterogeneity in grain size and distribution to influence LNAPL migration. The spills in H3040U and CB3040U were very similar in zones of residual water saturation, however, they differed once the spill reached the top of the capillary fringe. The partially drained layer of coarser sand in CB3040U created a zone where LNAPL could pool instead of spreading laterally like it did in H3040U. Nevertheless, the spill in CB3040U was similar enough to the spill in H3040U to classify the CB3040 pack as homogeneous without compromising predictions in LNAPL migration (in unfrozen condition). However, the spills in H3040F and CB3040F showed more pronounced differences. While classifying CB3040 packs as homogeneous in unfrozen condition may lead to accurate predictions of LNAPL migration, it might not be the case in frozen condition since the ice froze in a manner that encouraged LNAPL to preferentially spread in one direction once it hit the top of the ice capillary fringe (rather than equally spread on both sides). Such results suggest that there might have been enhancement of the heterogeneity effects in frozen soils at high ice saturation. Future research should investigate if this observation is consistent in different ice saturation conditions.

Results showed that the effects of the cross-beds can differ between unfrozen and frozen conditions. The spill in CB4070U was very sensitive to the heterogeneity of the pack throughout (cross-beds), including in zones of residual water saturation. However, the spill in CB4070F followed the inclined bedding of the pack, while also spreading laterally due to restricted pore space by ice, and an increase in the LNAPL viscosity at low temperatures. Future research should further investigate the effects of viscous forces in frozen soils, including the conditions where viscous forces stabilize capillary forces. Numerical models should also consider using viscous forces in addition to buoyancy and capillary forces for accurate NAPL migration prediction. Even though the effects of the cross-beds were diminished in frozen conditions due to competing viscous forces, the heterogeneity in grain size and ice content still played a significant role. The spill in CB4070F did not breach through the second capillary barrier made from a layer of fine sand at high ice saturation. Such small layers are important since they could easily be missed in the field (both the layer of grains and its ice content), but their effect on LNAPL migration can be significant. Future research could look into the ice saturation threshold required to completely

block LNAPL vertical migration. Future research could even consider investigating the efficiency of such thin layers as a mean of LNAPL containment barrier in frozen soils (i.e., fuel farms).

Spills in unfrozen condition all migrated to greater depths than spills in frozen condition since water drainage is not possible once it turns to ice (the ice-saturated sand supported the LNAPL at higher elevations in the cell). Additionally, the LNAPL penetration rates decreased in frozen conditions due to an increase in the LNAPL viscosity and restriction of pore space by ice. Previous studies have showed evidence of LNAPL migration in high ice saturation layers (through small fissures or cracks formed by thermal contraction), however, the cell in this study only went though one freezing cycle therefore reducing the likelihood of such cracks or fissured from being formed. Penetration rates also decreased with an increasing degree of heterogeneity (layered system lead to more lateral spreading).

In frozen condition, the spills migrated as wider masses even at residual ice saturation. In terms of total footprint (total width), the spill in CB3040F ended with a bigger footprint than in CB3040U, however, the opposite was true for the spills in CB4070 packs (the total footprint was greater in CB4070U than CB4070F). This means that while LNAPL spills may migrate as wider masses in frozen conditions, the total footprint may not necessarily be greater, and that proper soil characterization is important to determine the degree of heterogeneity of the soil structure.

Additionally, the results from this experiment act as a good reminder that permafrost table does not necessarily mean impermeable. Even though permafrost soils generally have low hydraulic conductivities, the permafrost table should not be automatically associated to high ice saturation since it describes the thermal behaviour of the ground only. Any depth in each frozen pack used in this study could represent the permafrost table conditions in the field. While the penetration rate may diminish in frozen conditions, only layers of high ice saturation (i.e., 70 %) may completely block LNAPL vertical migration.

Finally, the LTM proved to be a good method to use in frozen soils for the investigation of LNAPL migration. Future research should consider improving the methodology used in this study to reduce the redness of the sand packs prior to the spill (by changing the camera settings) to increase the contrast between the colored heptane and sand. Alternatively, blue dye could be used. As in unfrozen soil, the LTM should be tested for use in frozen soils to perform quantitative analysis and generate wetting and nonwetting saturation maps. Future research should also concentrate efforts to investigate the halo effects observed in frozen spill images.

3.5 References

Andersland, O., & Anderson, D. (1978). *Geotechnical Engineering for Cold Regions*.

Andersland, O., Wiggert, D., & Davies, S. (1996). Hydraulic Conductivity of Frozen Granular Soils. *J. Env. Eng.*

Anderson, D., & Morgenstern, N. (1973). Physics, Chemistry, and Mechanics of Frozen Ground: A Review. *Proc. 2nd International Conference on Permafrost, Yakutsk, U.S.S.R., North American Contribution, U.S. National Academy of Sciences*.

Barnes, D., & Chuvilin, E. (2009). Migration of Petroleum in Permafrost-Affected Regions. In R. Margesin, *Permafrost Soils.* Springer.

Barnes, D., & Shur, Y. (2003). Investigation of Immiscible Fluid Movement Through Frozen Porous Media. *Water Resources Center*.

Barnes, D., & Wolfe, S. (2008). Influence of Ice on the Infiltration of Petroleum into Frozen Coarse-Grained Soil. *Petroleum Science and Technology*.

Belfort, B., Weill, S., Fahs, M., & Lehmann, F. (2019). Laboratory Experiments of Drainage, Imbibition and Infiltration under Artificial Rainfall Characterized by Image Analysis Method and Numerical Simulations. *Water*.

Biggar, K. (n.d.). Contaminant Movement in Permafrost and Freezing Soils.

Biggar, K., & Neufeld, J. (1996). Vertical Migration of Diesel into Silty Sand Subject to Cyclic Freeze-Thaw. *8th Annual International Conference on Cold Regions Engineering*.

Biggar, K., Haidar, S., Nahir, M., & Jarrett, P. (1998). Site Investigations of Fuel Spill Migration into Permafrost. *Journal of Cold Regions Engineering*.

Conrad, S., Glass, R., & Peplinski, W. (2002). Bench-Scale Visualization of DNAPL Remediation Processes in Analog Heterogeneous Aquifers: Surfactant Floods and In Situ Oxidation Using Permanganate. *Journal of Contaminant Hydrology*.

Darnault, C., DiCarlo, D., Bauters, T., Jacobson, A., Throop, J., Montemagno, C., . . . Steenhuis, T. (2001). Measurement of Fluid Contents by Light Transmission in Transient Three-Phase Oil-Water-Air Systems in Sand. *Water Resources Research*.

Darnault, C., Throop, J., DiCarlo, D., Rimmer, A., Steenhuis, T., & Parlange, J. (1998). Visualization by Light Transmission of Oil and Water Contents in Transient Two-Phase Flow Fields. *Journal of Contaminant Hydrology*.

Davidson, M., Mumford, K., Mullins, N., & Calvert, M. (2022). Modification of a 3D Printer to Create Geologically Realistic Structures Used to Investigate Gas Migration Using the Light Transmission Method. *Vadose Zone Journal*.

Ewing, R., & Berkowitz, B. (1998). A Generalized Growth Model for Simulating Initial Migration of Dense Non-Aqueous Phase Liquids. *Water Resources Research*.

Fourie, W., Barnes, D., & Shur, Y. (2007). The Formation of Ice from the Infiltration of Water in Frozen Coarse Grain Soils. *Cold Regions Sci. Technol.*

Frette, V., Feder, J., Jossang, T., & Meaking, P. (1992). Buoyancy-Driven Fluid Migration in Porous Media. *The American Physical Society*.

Glass, R., Conrad, S., & Peplinki, W. (2000). Gravity-Destabilized Nonwetting Phase Invasion in Macroheterogeneous Porous Media: Experimental Observations of Invasion Dynamics and Scale Analysis. *Water Resources Research*.

Kechavarzi, C., Soga, K., Illangasekare, T., & Nikopoulos, P. (2008). Laboratory Study of Immiscible Contaminant Flow in Unsaturated Layered Sands. *Vadose Zone Journal*.

Konrad, J., & McCammon, A. (1990). Solute Partitioning in Freezing Soils. *Canadian Geotechnical Journal*.

Kueper, B., & Frind, E. (1991). Two-Phase Flow in Heterogeneous Porous Media. *Water Resources Journal*.

Lenormand, R., & Touboul, E. (1988). Numerical Models and Experiments on Immiscible Displacements in Porous Media. *J. Fluid Mech.*

Leverett, M. (1941). Capillary Behaviour in Porous Solids. *Trans. Am. Inst. Min. Metall. Pet. Eng.*

McCauley, C., White, D., Lilly, M., & Nyman, D. (2002). A Comparison of Hydraulic Conductivities, Permeabilities and Infiltration Rates in Frozen and Unfrozen Soils. *Cold Regions Science and Technology*.

McKenzie, J., Kurylyk, B., Walvoord, M., Bense, V., Fortier, D., Spence, C., & Grenier, C. (2021). Invited Perspective: What lies beneath a changing Arctic? *The Cryosphere*.

Muller, S. (1943). Permafrost or Permanently Frozen Ground and Related Engineering Problems. *U.S. Engineers Office, Intelligence Branch, Strategic Engineering Study Special Report 62*.

Niemet, M., & Selker, J. (2001). A New Method for Quantification of Liquid Saturation in 2D Translucent Porous Media Systems Using Light Transmission. *Advances in Water Resources*.

Oostrom, M., Dane, J., & Wietsma, T. (2007). A Review of Multidimensional, Multifluid, Intermediate-Scale Experiments: Flow Behaviour, Saturation Imaging, and Tracer Detection and Quantification. *Vadose Zone Journal*.

Orozco-Lopez, E., Munoz-Carpena, R., Gao, B., & Fox, G. (2021). High-Resolution Pore-Scale Water Content Measurement in a Translucent Soil Profile From Light Transmission. *ASABE*.

Osborne, M., & Sykes, J. (1986). Numerical modeling of immiscible organic transport at the Hyde Park landfill. *Water Resources Research*.

Poulsen, M., & Kueper, B. (1992). A Field Experiment to Study the Behaviour of Tetrachloroethylene in Unsaturated Porous Media. *Environ. Sci. Technol.*

Rivett, M., Tomlinson, D., Thornton, S., Thomas, A., Leharne, S., & Wealthall, G. (2014). An Illustrated Handbook of LNAPL Transport and Fate in the Subsurface. *CL:AIRE*.

Schroth, M., Ahearn, S., Selker, J., & Istok, J. (1996). Characterization of Miller-Similar Silica Sands for Laboratory Hydrologic Studies. *Soil Sci. Soc.*

Schroth, M., Istok, J., Selker, J., Oostrom, M., & White, M. (1998). Multifluid Flow in Bedded Porous Media: Laboratory Experiments and Numerical Simulations. *Advances in Water Resources*.

Singh, K., & Niven, R. (2013). Non-Aqueous Phase Liquid Spills in Freezing and Thawing Soils: Critical Analysis of Pore-Scale Processes. In L. Ma, *Critical Reviews in Environmental Science and Technology.* Taylor & Francis.

Tice, A., Anderson, D., & Banin, A. (1976). The Prediction of Unfrozen Water Contents in Frozen Soils from Liquid Limit Determinations. *CRREL Report 76-8*.

Tidwell, V., & Glass, R. (1994). X Ray and Visible Light Transmission for Laboratory Measurement of Two-Dimensional Saturation Fields in Thin-Slab Systems. *Water Resources Research*.

Van De Ven, C., & Mumford, K. (2018). Visualization of Gas Dissolution Following Upward Gas Migration in Porous Media: Technique and Implications for Stray Gas. *Advances in Water Resources*.

Van De Ven, C., Abraham, J., & Mumford, K. (2020). Laboratory Investigation of Free-Phase Stray Gas Migration in Shallow Aquifers Using Modified Light Transmission. *Advances in Water Resources*.

Van Everdingen, R. (1990). Ground-Water Hydrology. *Northern Hydrology: Canadian Perspectives.*

Walvoord, M., & Kurylyk, B. (2016). Hydrologic Impacts of Thawing Permafrost - A Review. *Vadose Zone Journal*.

Wang, C., Su, X., Lyu, H., & Yuan, Z. (2021). Remobilization of LNAPL in Unsaturated Porous Media Subject to Freeze-Thaw Cycles Using Modified Light Transmission Visualization Technique. *Journal of Hydrology*.

Wiggert, D., Andersland, O., & Davies, S. (1997). Movement of Liquid Contaminants in Partially Saturated Frozen Granular Soils. *Cold Regions Science and Technology*.

Woo, M.-k. (2012). *Permafrost Hydrology.* Springer.

Zhang, Y., Wu, J., & Ye, S. (2021). Quantification of the Fluid Saturation of Three Phase of NAPL/Water/Gas in 2D Porous Media Systems Using a Light Transmission Technique. *Journal of Hydrology*.

CHAPTER 4 CONCLUSION AND RECOMMENDATIONS

4.1 Conclusion

Current permafrost conditions influence LNAPL migration in a manner not found in temperate soils due to low temperatures, low hydraulic conductivities, the presence of ground ice, the influence of freeze and thaw cycles, and the typically shallow active layers. Further, as a result of climate warming, permafrost hydrology is expected to change such that the movement, storage, and exchange of surface and subsurface fluids will be modified. Thaw-activated groundwater flow will create new transport pathways for contaminants such as LNAPLs, which will increase risks to both human and ecosystem health. Understanding LNAPL behaviours in current and future permafrost terrain is essential for protecting the environment in a changing climate.

Most laboratory experiments to date focused on the isolated effects of pore ice and low temperatures on LNAPL migration. Those experiments were performed in homogeneous porous media with respect to both sand grain distribution and water or ice contents. The effects of geological and water distribution heterogeneity on LNAPL migration in temperate soils are well known, however, there is a lack of experiments investigating those effects in frozen soils. In addition, permafrost terrains offer unique features and complex dynamics which need to be investigated at high spatial resolution. To address the needs to investigate LNAPL migration in frozen heterogeneous porous media at high spatial resolution, a series of experiments were conducted in an intermediate scale 2D flow cell using the light transmission method.

The LTM has been traditionally used in unfrozen soils, however, the method was adapted for use in frozen soils experiments to quantify ice and track LNAPL spills progression in sand packs with different degrees of heterogeneity. Results showed that:

- Ice can be quantified using the LTM. Known and calculated ice volumes were within 2 % over a range of different ice saturations in the cell, which means that the LTM can be used in future experiments to investigate saturated and unsaturated flow phenomena in frozen soils (Chapter 2).

- A single fit parameter can be used to calibrate data and quantify water and ice in unfrozen and frozen conditions respectively, which means that the calibration process can be performed during unfrozen experiments and then be applied to frozen experiments. This allows the calibration process to be completed in a matter of hours, rather than days (Chapter 2).

- Using the LTM, frozen sand packs showed more light attenuation than unfrozen sand packs, which is attributed to the creation of entrapped air bubbles (in ice) as ice forms from pure water. Fresnel's Law states that light can be refracted and absorbed as it passes through interfaces so an increase in interfaces caused by newly created air bubbles result in more light attenuation (Chapter 2).

- LNAPL's response to heterogeneity in frozen soils differ from unfrozen soils. Heterogeneity effects can be enhanced in frozen conditions in zones of high ice

saturations such that even heterogeneity barely visible to the naked eye can influence LNAPL migration in frozen soils. In CB3040F, LNAPL migrated in the direction of the cross-beds once it hit the top of the frozen capillary fringe, an absent behaviour in unfrozen conditions (CB3040U). In unfrozen soils, buoyancy and capillary forces are dominant when it comes to LNAPL migration, however, viscous forces need to be considered in frozen soils due to an increase in the LNAPL viscosity with a decrease of temperature. Viscous forces compete with capillary forces, which can change LNAPL's response to geological heterogeneity (i.e., cross-beds) and cause more lateral spreading as LNAPL migrates down. Nevertheless, heterogeneity in grain size and distribution as well as ice contents remains a critical component for accurate predictions of LNAPL migration in frozen soils. For example, thin layers of fine-grained soils at high ice saturation can be impermeable and prevent further vertical LNAPL migration. Such small layers are important since they could easily be missed in the field, but their effect on LNAPL migration can be significant (Chapter 3).

- LNAPL spills in unfrozen conditions can migrate to greater depths than spills in frozen conditions. In unfrozen conditions, LNAPL can partially invade the top of the capillary fringe and even induce water drainage, however, once the capillary fringe turns to ice, no invasion or drainage occurs, supporting LNAPL at higher elevations (Chapter 3).

- LNAPL penetration rates decrease in frozen conditions due to both an increase in the LNAPL viscosity and restriction of pore space by ice (Chapter 3).

- LNAPL spills in frozen conditions can migrate as wider masses due to both partial blockage of pore space by ice and an increase in the LNAPL viscosity, however, this study demonstrated that it does not mean that the LNAPL spill will result in a larger footprint (total width) (Chapter 3).

- Mild heterogeneity (i.e., CB3040 packs) may not have a significant effect on LNAPL migration in unfrozen conditions at residual water saturation, however, it does once LNAPL reaches the top of the capillary fringe. In these experiments, LNAPL pooled in partially drained coarse sand layers restricting lateral movement. This is proof that water distribution in soil is just as important as geological heterogeneity when it comes to LNAPL migration (Chapter 3).

4.2 Recommendations

The method employed in this study was adapted from previous investigations performed on unfrozen soils. Future work should consider improving the experimental set-up and/or the methodology such that:

- The cell is not completely filled when packing and a space is left for the increase in volume when water turns to ice. This would allow a frozen I_s image to be obtained without compromising the tracking of water mass during drainage and without additional image cropping, which reduces visibility in the sand pack.

- Light reflection is reduced in the cell (in zones of unsaturated saturations). The camera should be pushed as far away from the cell as possible (while still fitting in the freezer) to see if light reflection occurs on the camera lens. A different curtain fabric should be tried as well (use more absorbing layers rather than one black-out curtain). A reduction in light reflection would result in a lower fitting parameter, which would increase the water saturation detection limit. Further, minimizing light reflection in the cell might provide some insights as to why the attenuation of light was more significant at residual saturation than 100 % saturation in frozen conditions. Packing dry and using degassed water might be helpful. Those changes might reveal if the inconsistent darkening process is due to light pollution in zones of low water saturations.

- Future research should concentrate efforts to investigate the halo effects observed in frozen spill images and then look into further enhancing contrast between LNAPL and the sand pack by either changing the camera settings to reduce the captured redness in sand pack images prior to the spill or make use of a blue dye.

The work performed in this study helped to gain a better understanding of LNAPL migration in frozen heterogeneous porous media using the LTM. Additional insight could be gained from the following future work:

- Results from this experiment highlighted the impact of thin fine-grained soil layers at high ice saturation on LNAPL migration and the importance to be careful when soil sampling not to miss them. Future research might consider investigating the efficiency of using such thin layers as LNAPL containment barriers in frozen soils (i.e., fuel farms). It would also be worth investigating the ice saturation threshold above which LNAPL penetration is blocked in various types of fine sands.

- Findings from this paper also suggested that the effects of mild heterogeneity might be enhanced in frozen conditions at high ice saturation only, however, future research should consider investigating it further to see if this observation is consistent in different ice saturation conditions. Future work should also investigate the formation of ice in different sand pack configurations and see if the shape taken by the increase in volume as water turns to ice is influenced by the geological heterogeneity, which, in turn, would influence LNAPL migration.

- LNAPL was not as responsive to the cross-beds heterogeneity in frozen soils as it was in unfrozen soils due to viscous forces competing with buoyancy and capillary forces. Future research should further investigate the effects of competing forces and the conditions where viscous forces increase in importance.

- Results/data from this study should be used to test and calibrate numerical models to simulate LNAPL migration in frozen soils. Additional experiments following the same procedure can also be performed to evaluate multiple scenarios (i.e., study the effects of active layer expansion to mimic a spill occurring in the active layer, study the effects

of surface features such as various degrees of ice saturation to mimic a spill at the ground surface etc.), which would provide useful data to further improve the conceptual model proposed in this study.

- The LTM proved to be a good tool to track LNAPL spill progressions in the cell. Future work should consider performing a quantitative study on LNAPL migration in frozen soils such that saturation maps and profiles are generated, which would validate the use of the LTM for LNAPL migration studies in frozen soils. Most of the recommended future work outlined in the previous lines could also be completed using the LTM.

The results presented in this study act as a good reminder that permafrost table does not necessarily mean impermeable. Even though permafrost soils generally have low hydraulic conductivities, the permafrost table should not be automatically associated to high ice saturation since it describes the thermal behaviour of the ground only and not the freeze-thaw state of water. Any depth in each frozen pack used in this study (Chapter 3) could represent the permafrost table conditions in the field. While the penetration rate may diminish in frozen conditions, only layers of high ice saturation may completely block LNAPL vertical migration provided that there are no cracks formed by thermal contraction. Finally, the observations made in this study reinforce the importance of proper soil characterization (including soil geology and water/ice distribution) in order to accurately predict LNAPL migration, in both unfrozen and frozen conditions.

APPENDICES

Appendix A:

A.1 Precision / Resolution Analysis

Prior to the water saturation analysis in Chapter 2, images were upscaled/discretized to one-mm^2 blocks so that each new pixel dimensions captured the size of a sand grain, while also reducing noise. All intensity values in a given one-mm^2 block were averaged to form a new pixel block, for which its chosen size is the result of a precision / resolution analysis. Standard deviations in a known fully saturated area were computed for various block sizes, and it was observed that the bigger the block, the smaller standard deviation, resulting in an increase in precision in the analysis (Figure A.1).

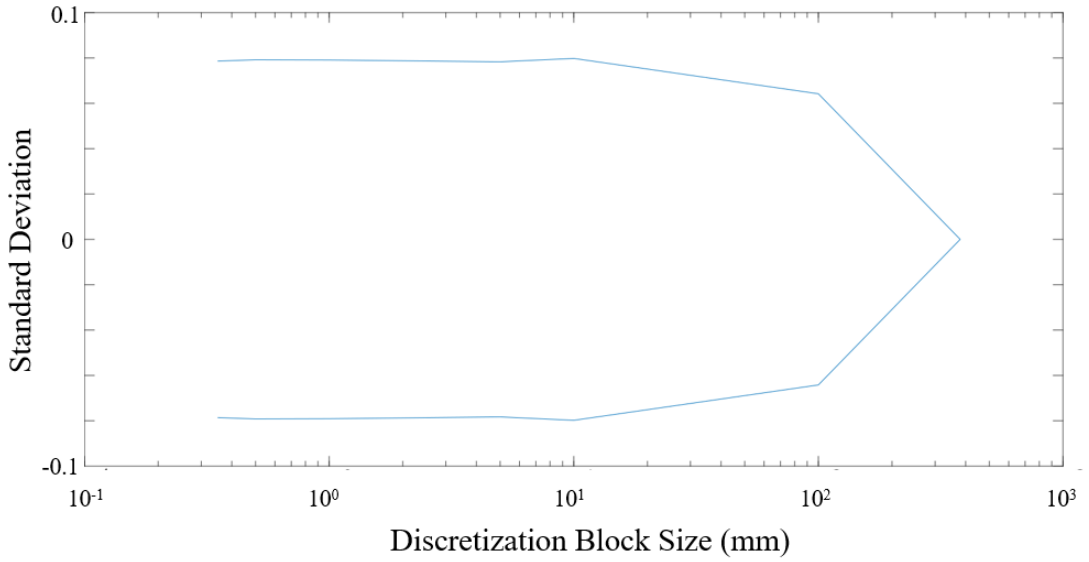

FIGURE A.1: Standard deviation versus block size.

Figure A.2 shows the resulting resolutions for four different block sizes (0.35 mm, 1 mm, 5 mm, 10 mm).

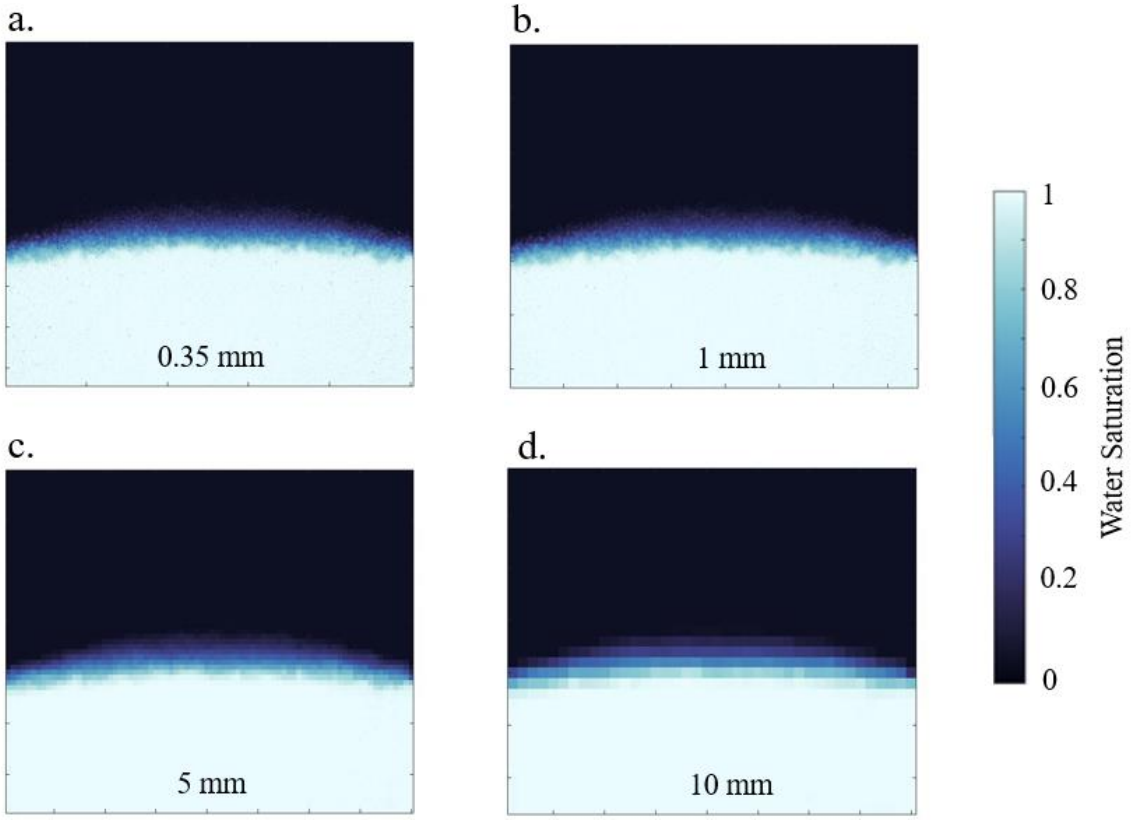

FIGURE A.2: Resolution resulting from the four following different block sizes (a) 0.35 mm, (b) 1 mm (c) 5 mm, and (d) 10 mm.

As seen in Figure A.1, the standard deviation is very small for all block sizes used. Further, the precision starts increasing once block sizes increase passed 10 mm. The precision does not change for any size below 10 mm. When looking at the resulting resolutions in Figure A.2, one can observe that there is not a significant difference between 0.35 mm and 1 mm. Despite the improvement in precision as the block size increases, the resolution seen in Figure A.2 for the 5 mm and 10 mm block sizes is decreased. The best compromise between precision and resolution is then found to be a block size of 1 mm (1 mm x 1 mm), which is what was used for the analysis described in this paper.

Appendix B

A complete set of images for each test performed in Chapter 2 is shown in Figures B.1-8.

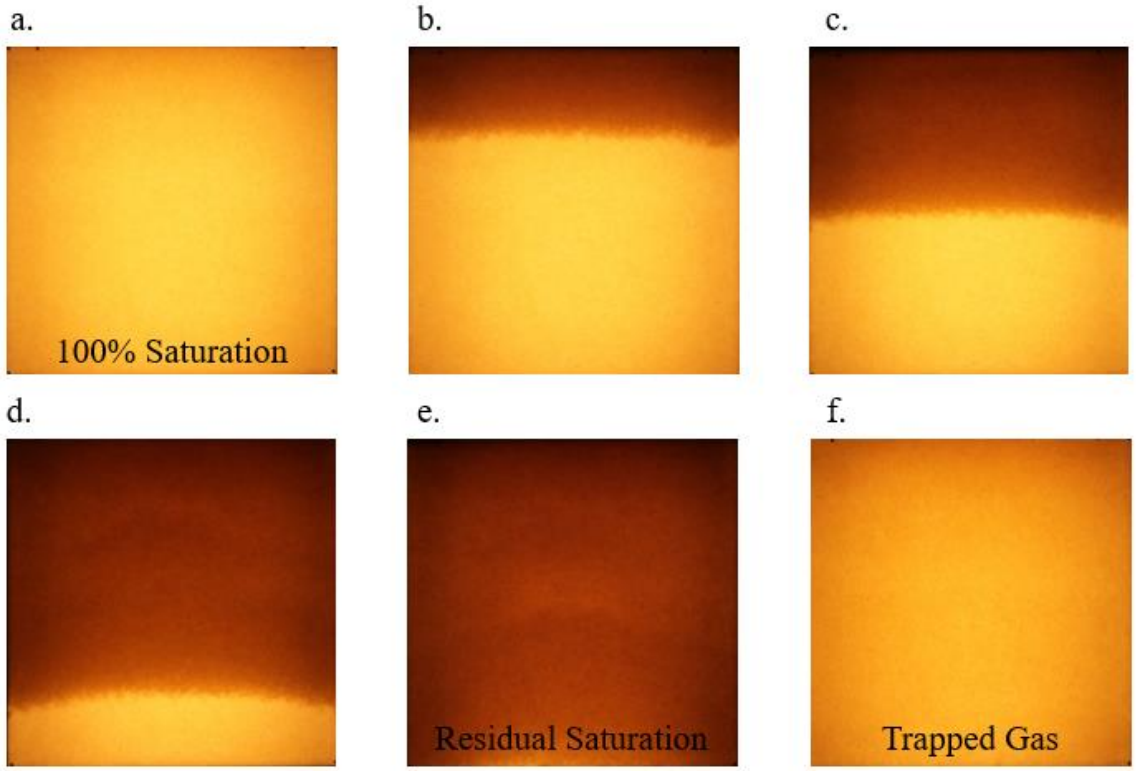

FIGURE B.1: Example of light transmission images from test U1 prior to image processing showing (a) saturated conditions followed by unsaturated conditions with water positions at approximately (b) 75 %, (c) 50 %, and (d) 25 % of the cell height, as well as (e) residual saturation and (f) following water imbibition to create trapped gas.

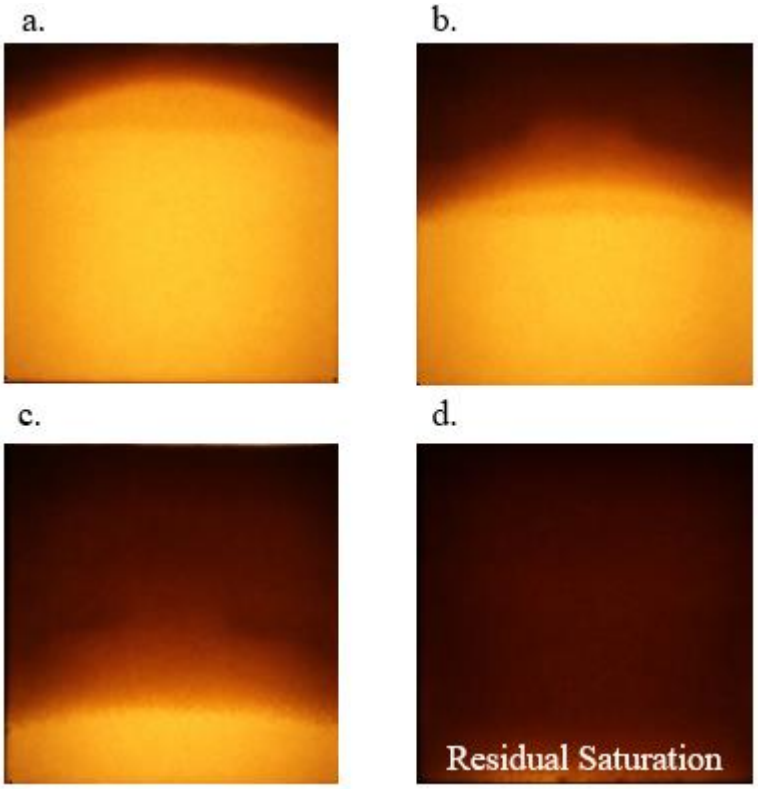

FIGURE B.2: Example of light transmission images from test F1 prior to image processing showing unsaturated conditions with water positions at approximately (a) 75 %, (b) 50 %, and (c) 25 % of the cell height, as well as (d) residual saturation.

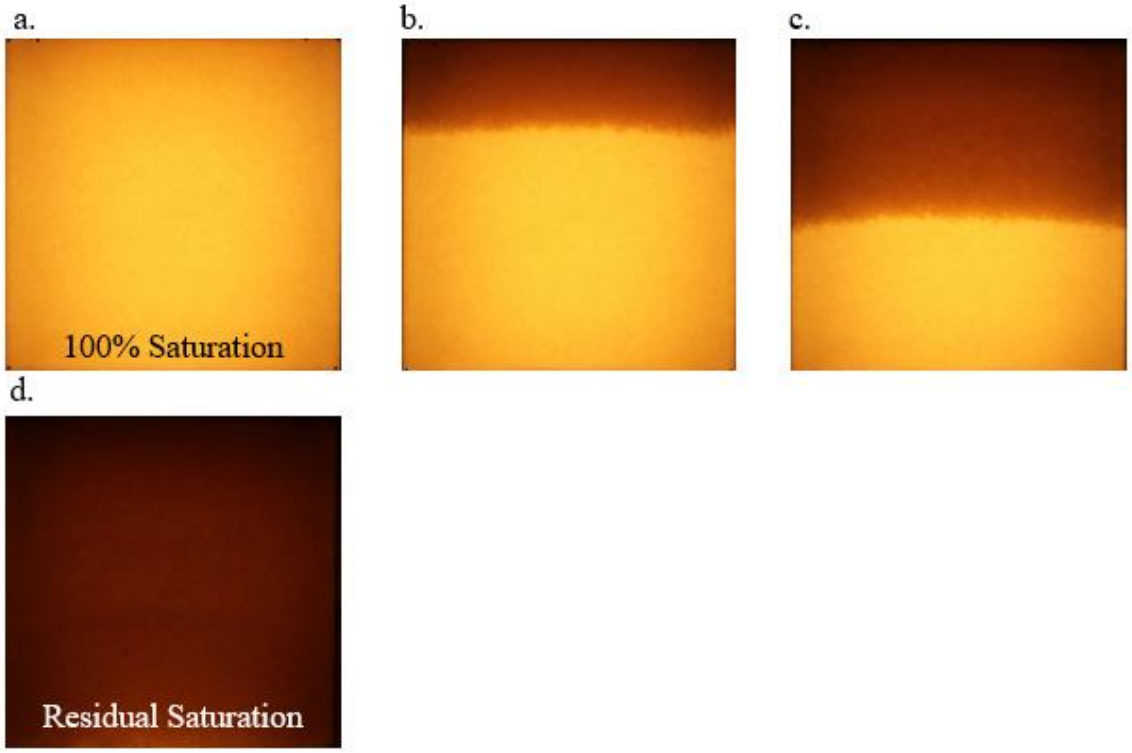

FIGURE B.3: Example of light transmission images from test U2 prior to image processing showing (a) saturated conditions followed by unsaturated conditions with water positions at approximately (b) 75 %, and (c) 50 % of the cell height, as well as (d) residual saturation.

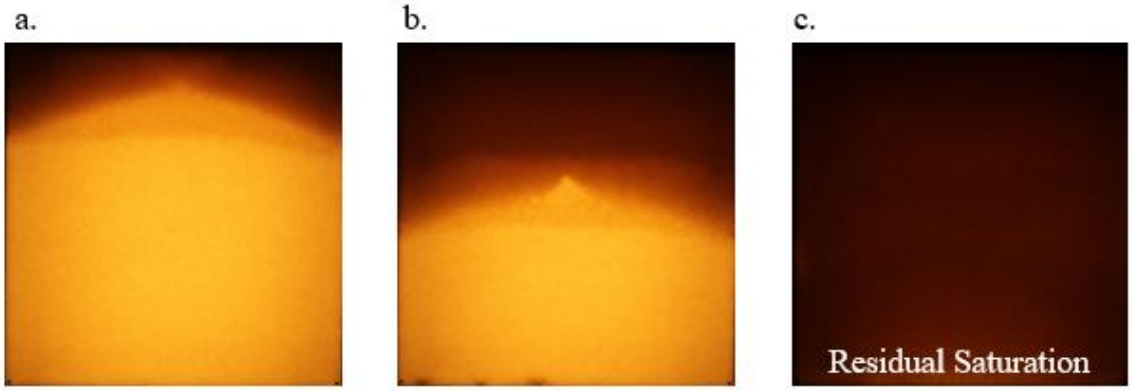

FIGURE B.4: Example of light transmission images from test F2 prior to image processing showing unsaturated conditions with water positions at approximately (a) 75 %, and (b) 50 % of the cell height, as well as (c) residual saturation.

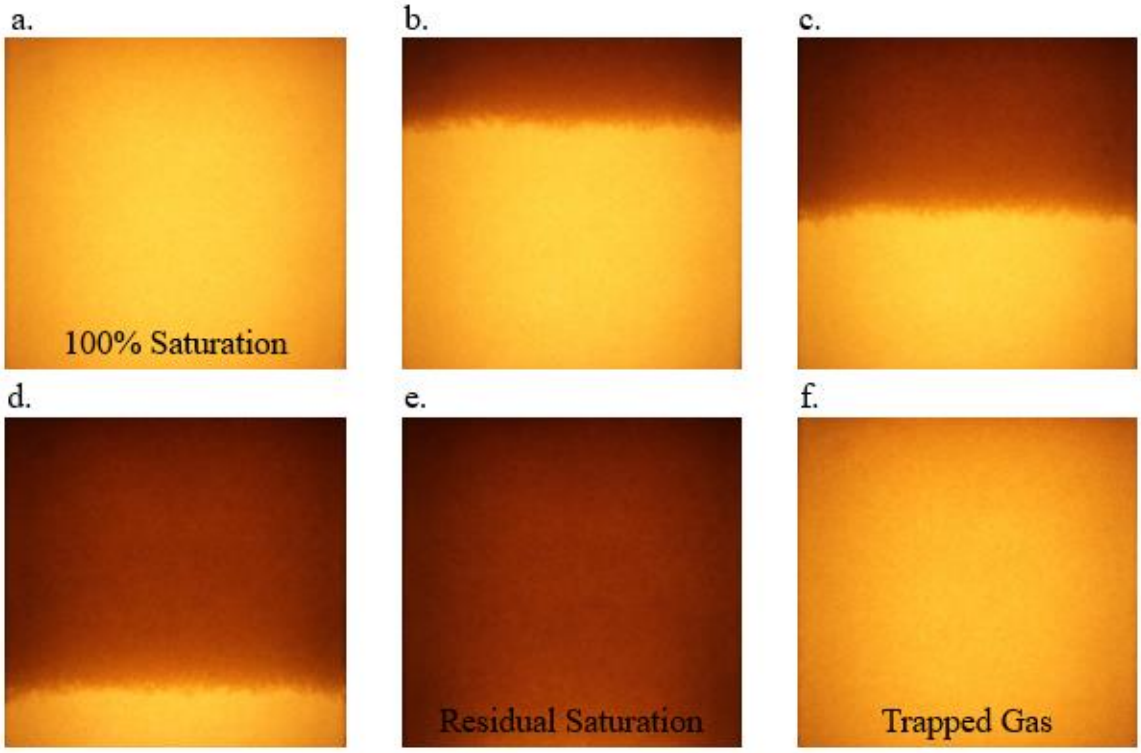

FIGURE B.5: Example of light transmission images from test U3 prior to image processing showing (a) saturated conditions followed by unsaturated conditions with water positions at approximately (b) 75 %, (c) 50 %, and (d) 25 % of the cell height, as well as (e) residual saturation and (f) following water imbibition to create trapped gas.

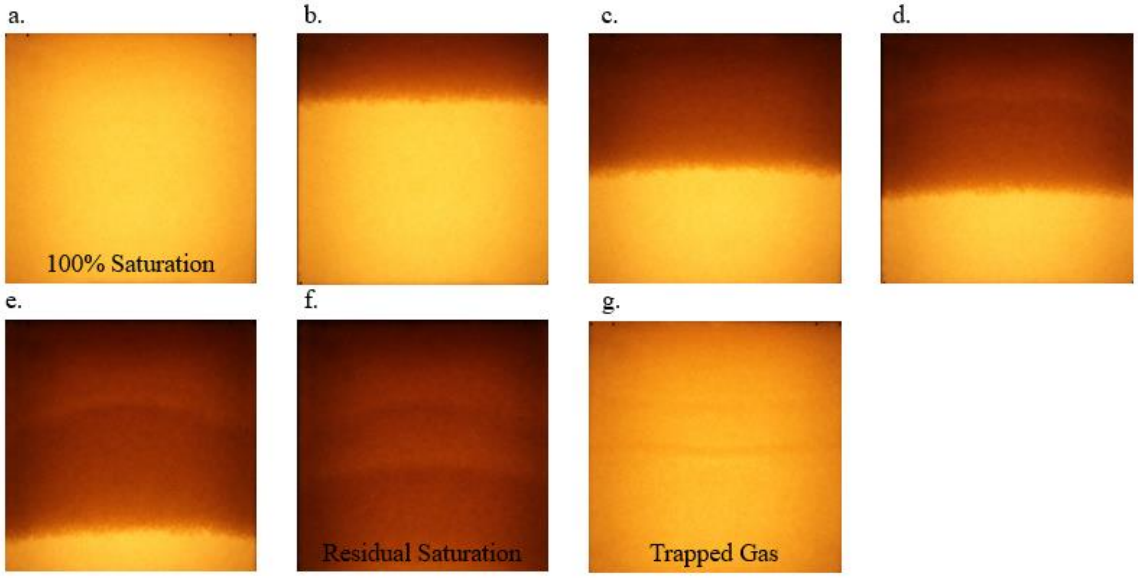

FIGURE B.6: Example of light transmission images from test U4 prior to image processing showing (a) saturated conditions followed by unsaturated conditions with water positions at approximately (b) 75 %, (c) 50 %, (d) 40 %, and (e) 25 % of the cell height, as well as (f) residual saturation and (g) following water imbibition to create trapped gas.

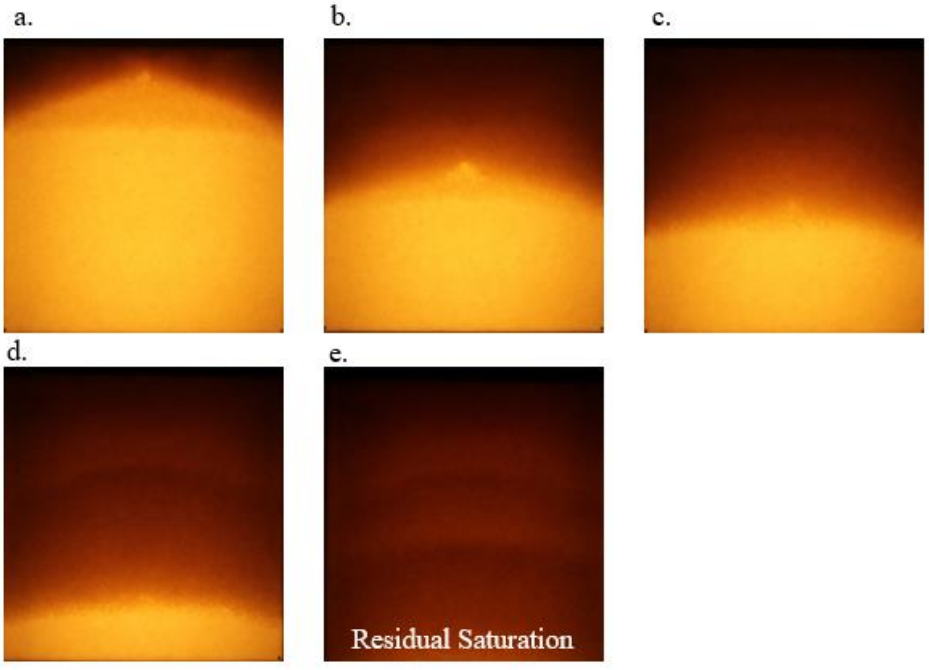

FIGURE B.7: Example of light transmission images from test F4 prior to image processing showing unsaturated conditions with water positions at approximately (a) 75 %, (b) 50 %, (c) 40 %, and (d) 25 % of the cell height, as well as (e) residual saturation.

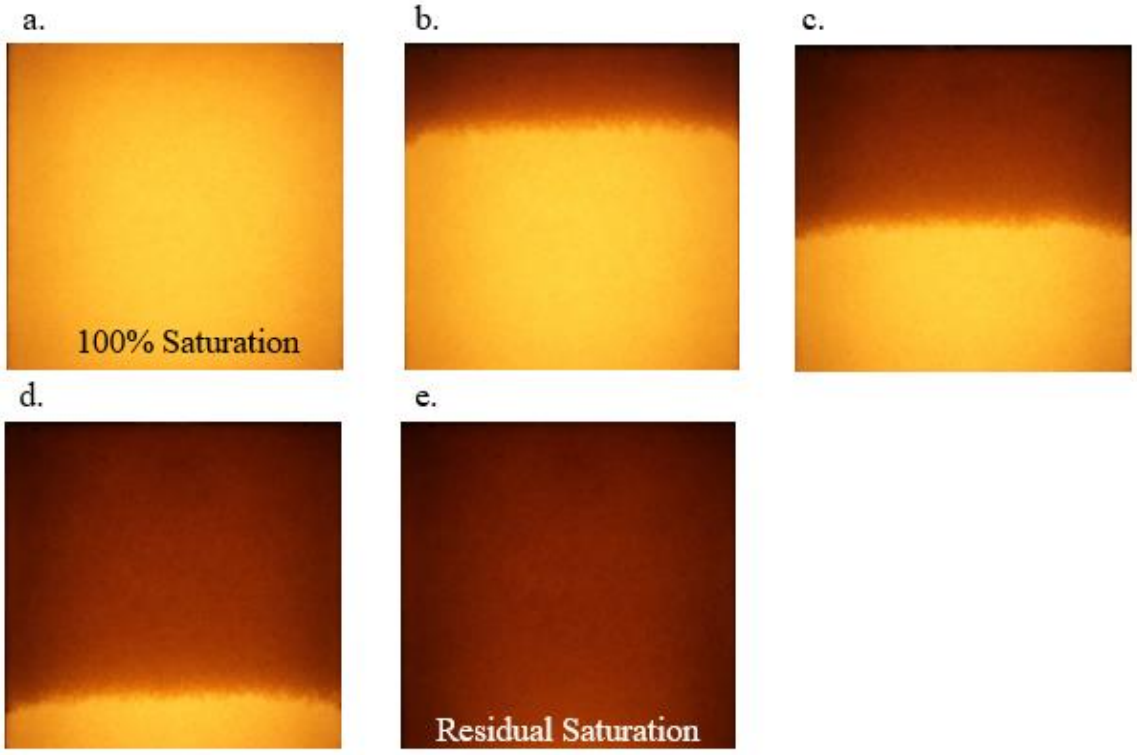

FIGURE B.8: Example of light transmission images from test U5 prior to image processing showing (a) saturated conditions followed by unsaturated conditions with water positions at approximately (b) 75 %, (c) 50 %, and (d) 25 % of the cell height, as well as (e) residual saturation.

Appendix C

Known and calculated water volumes in the cell for each Chapter 2 test is shown in Tables C1-8.

TABLE C.1: Test U1 known and calculated water volumes in the cell.

Water Position in the Cell	Known Water Volume (ml)	Calculated Water Volume (ml)
Sr	29.65	29.95
25 %	164.59	166.10
50 %	341.45	344.93
75 %	496.85	491.07
100 %	644.7	646.48
TG	535.81	526.60

TABLE C.2: Test U2 known and calculated water volumes in the cell.

Water Position in the Cell	Known Water Volume (ml)	Calculated Water Volume (ml)
Sr	29.67	29.75
50 %	331.70	333.41
75 %	494.70	494.78
100 %	645.09	646.70

TABLE C.3: Test U3 known and calculated water volumes in the cell.

Water Position in the Cell	Known Water Volume (ml)	Calculated Water Volume (ml)
Sr	30.04	30.12
25 %	157.62	157.57
50 %	334.95	337.28
75 %	500.23	495.29
100 %	652.97	654.69
TG	581.61	572.95

TABLE C.4: Test U4 known and calculated water volumes in the cell.

Water Position in the Cell	Known Water Volume (ml)	Calculated Water Volume (ml)
Sr	30.09	30.12
25 %	141.10	142.42
40 %	263.14	265.45
50 %	323.39	327.80
75 %	496.28	492.99
100 %	654.14	654.58
TG	544.52	546.05

TABLE C.5: Test U5 known and calculated water volumes in the cell.

Water Position in the Cell	Known Water Volume (ml)	Calculated Water Volume (ml)
Sr	29.48	29.53
25 %	150.36	153.84
50 %	332.34	330.02
75 %	509.18	500.73
100 %	640.85	641.88

TABLE C.6: Test F1 known and calculated ice volumes in the cell.

Water Position in the Cell	Known Water Volume (ml)	Calculated Water Volume (ml)
Sr	32.32	32.33
25 %	179.40	179.57
50 %	372.18	374.30
75 %	644.70	644.86

TABLE C.7: Test F2 known and calculated ice volumes in the cell.

Water Position in the Cell	Known Water Volume (ml)	Calculated Water Volume (ml)
Sr	32.34	32.47
50 %	361.55	363.73
75 %	645.09	647.65

TABLE C.8: Test F4 known and calculated ice volumes in the cell.

Water Position in the Cell	Known Water Volume (ml)	Calculated Water Volume (ml)
Sr	32.80	32.93
25 %	153.80	150.98
40 %	286.82	286.73
50 %	352.50	356.84
75 %	654.14	656.81

Appendix D

The set of images shown in figure D.1 display the freezing front in a freezing cell, which can be tracked due to low intensities of light passing through frozen porous media.

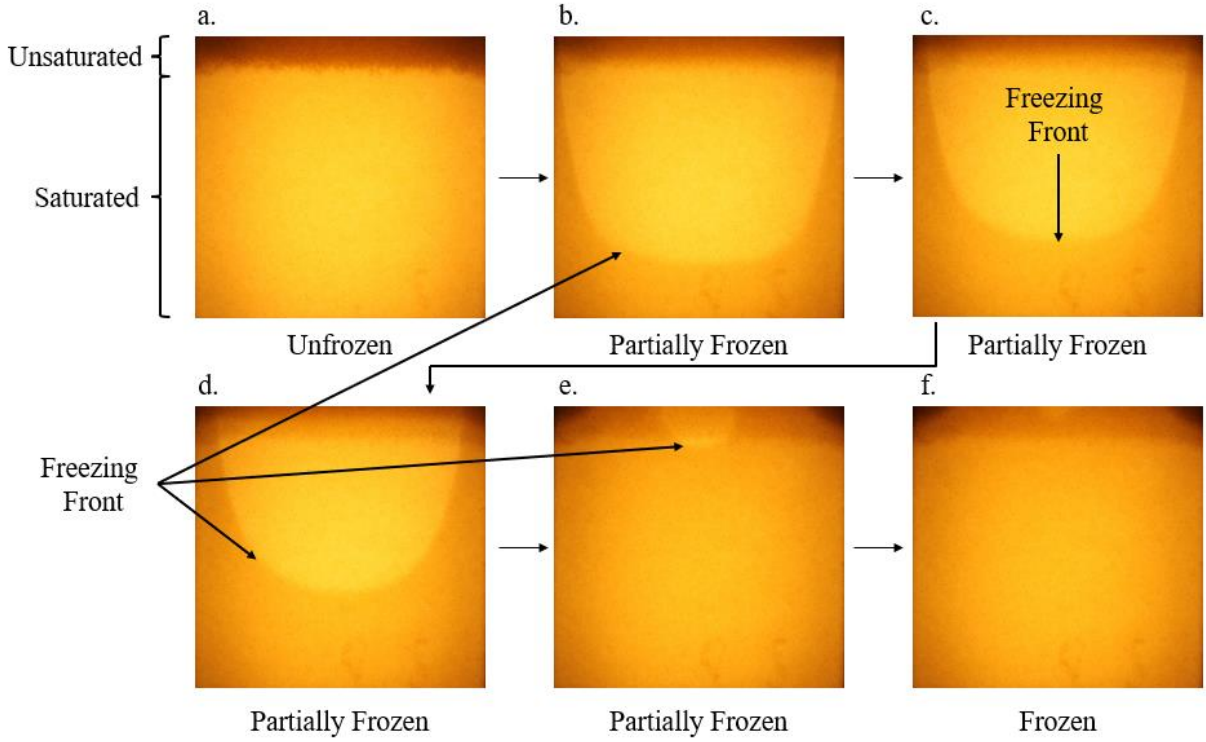

FIGURE D.1: Freezing cell images in the following conditions (a) unfrozen, (b) partially frozen, (c) partially frozen, (d) partially frozen, (e) partially frozen, and (f) frozen.

Appendix E

According to Van De Ven et al. (2020) fitting I_r/I_s, rather than using a measured I_r/I_s, may be required because gas-filled pore spaces adjacent to water-filled pore spaces may result in higher intensities due to the refraction of light from the adjacent water-saturated sand. This additional lighting by refraction creates brighter I_r images than those captured under stable drainage conditions. In Van De Ven et al. (2020) this occurred during unstable gas injection that created gas fingers. However, this could also cause the gas-filled pore spaces above the capillary fringe to be lit from the light source as well as the refracted light in the unfrozen experiments conducted here. As described by Van De Ven et al. (2020) this would result in a brighter transition zone between 100 % saturation and residual saturations, hence why the ratio of I_r/I_s may need to be increased to correct for the higher intensities recorded. The data obtained from both unfrozen and frozen tests presented in this paper supports this hypothesis since the calculated water volumes in the cell before calibration (i.e., using measured I_r/I_s values) were consistently higher than the known volumes of water, which an increase in intensities would cause. In addition, when looking at uncalibrated results of saturations (Figure E.1), it appears that light reflection may have been a potential source of error in the intensities recorded in the images. Although not visible to the naked eye, residual saturation areas in images of higher overall saturations were consistently observed to be brighter when compared to images at residual saturation, leading to believe that the high amount of light passing through full saturation zones might have been sufficient to either light up the curtain enclosure and/or reflect back from the camera lens to the cell, either way increasing intensities in regions of residual saturations. Figure E.1 illustrates *z* vs *I* and *z* vs *Sw* for test U4.

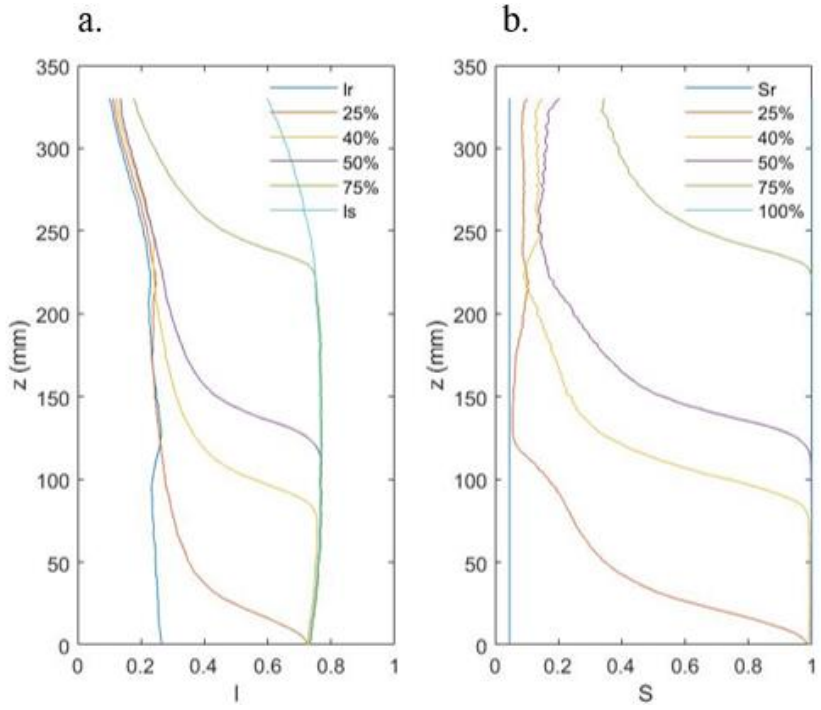

FIGURE E.1: (a) z vs I and (b) z vs S profiles using measured I_r/I_s for test U4.

Appendix F

The saturation profiles for all test performed in Chapter 2 (using the fit parameter) are shown in Figure F.1-8.

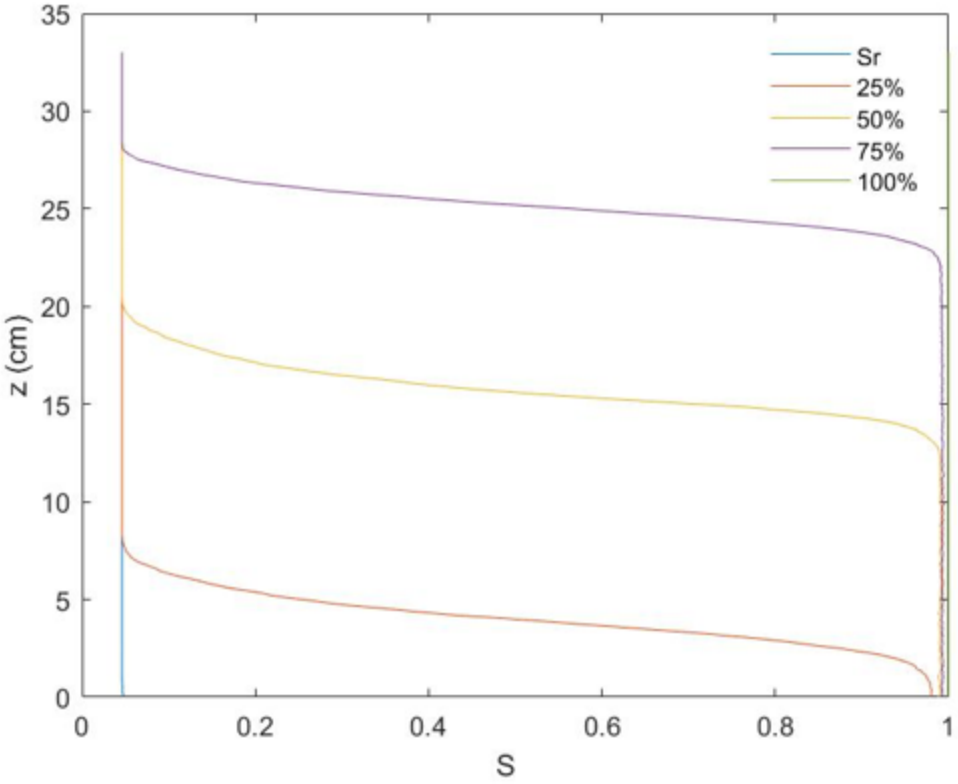

FIGURE F.1: Saturation profile versus height for test U1.

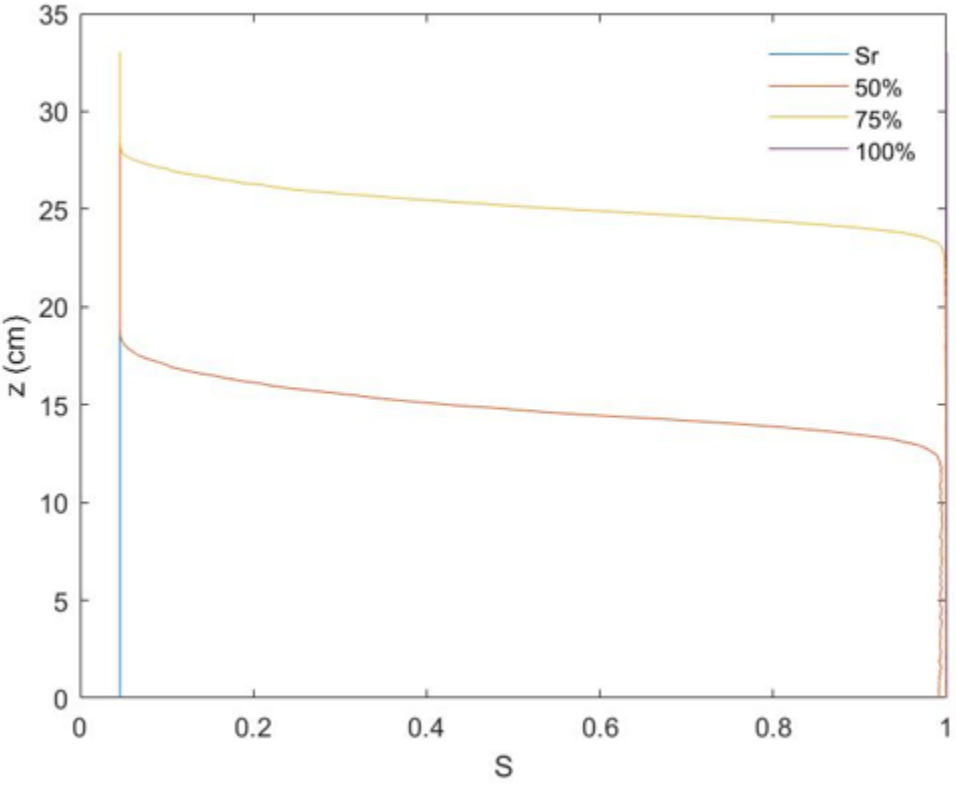

FIGURE F.2: Saturation profile versus height for test U2.

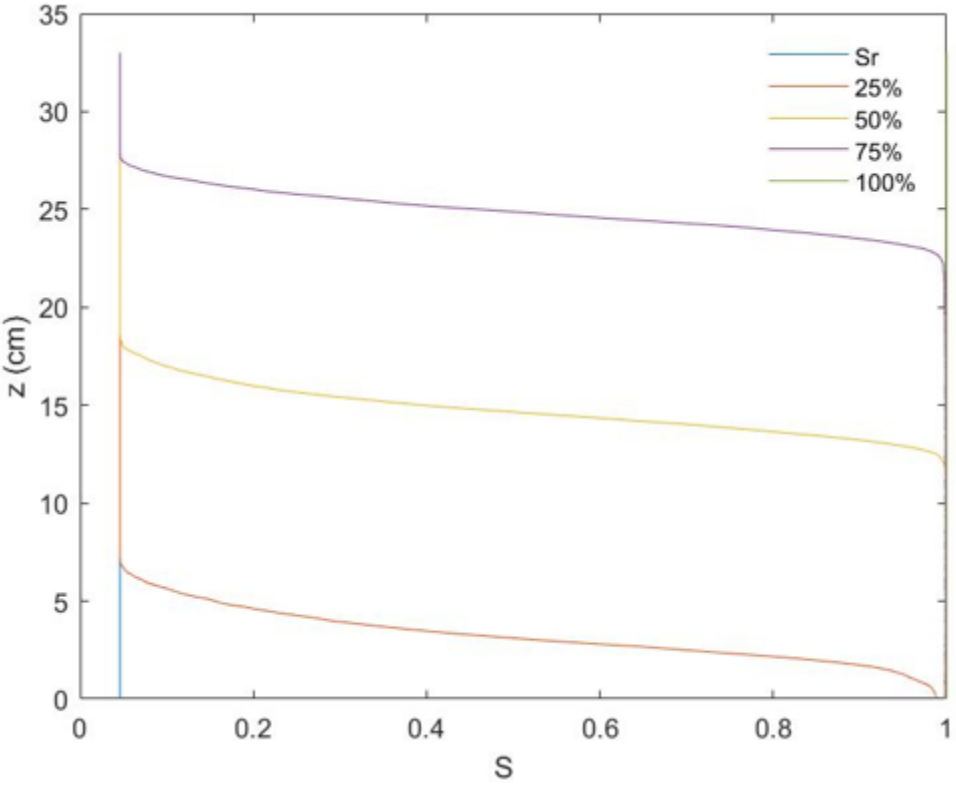

FIGURE F.3: Saturation profile versus height for test U3.

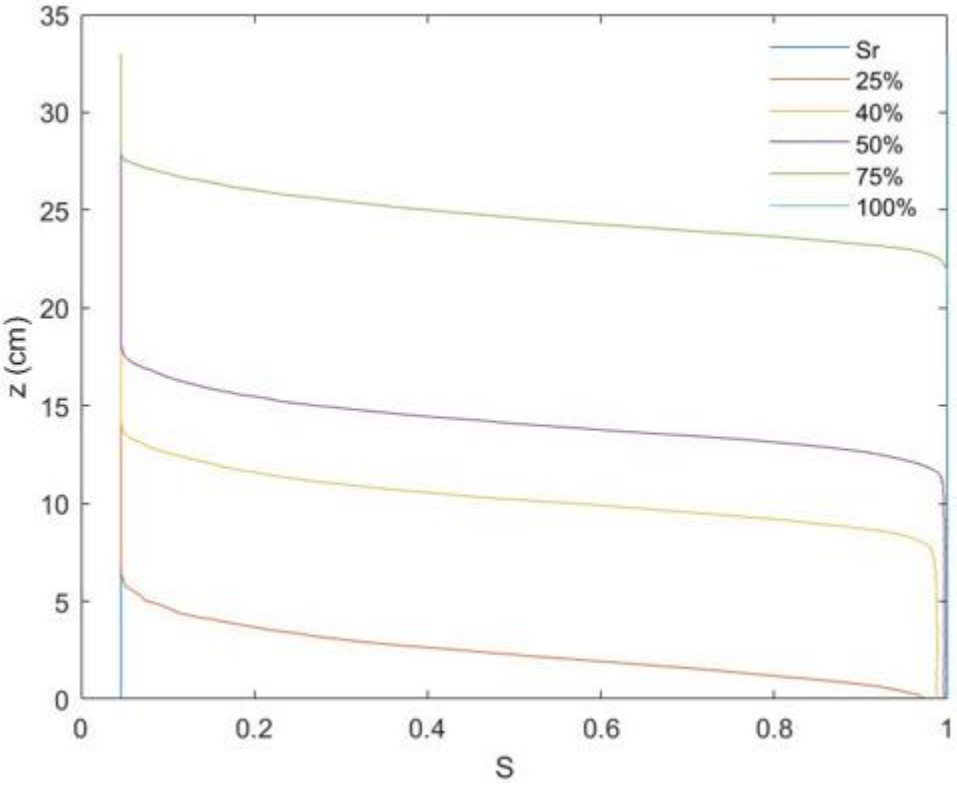

FIGURE F.4: Saturation profile versus height for test U4.

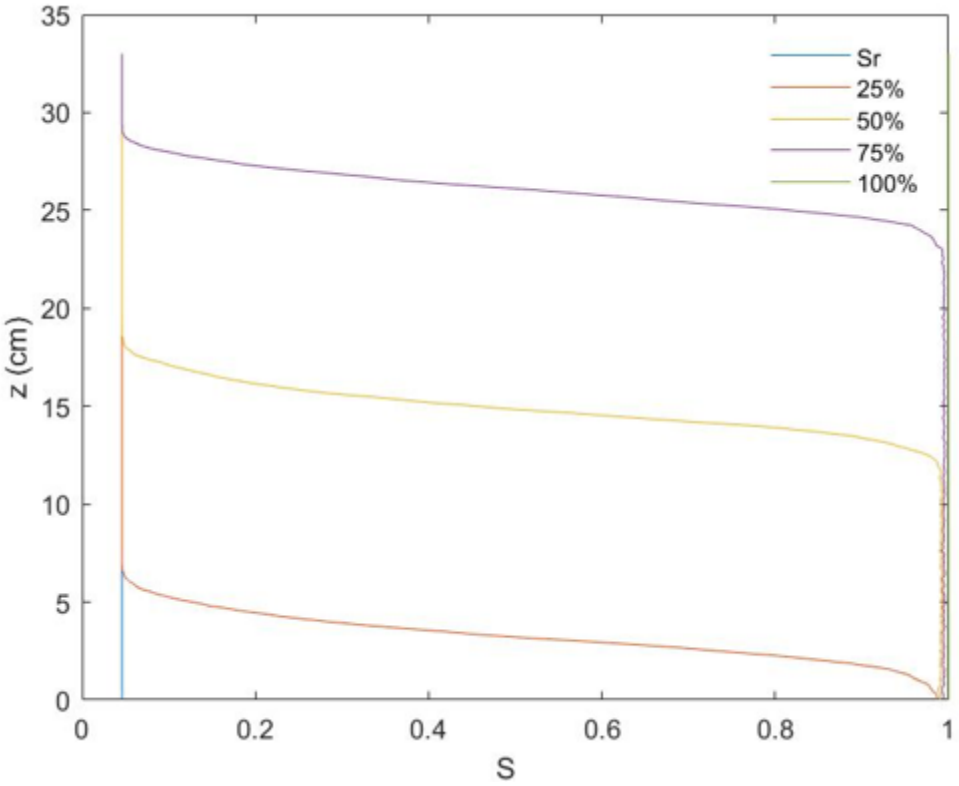

FIGURE F.5: Saturation profile versus height for test U5.

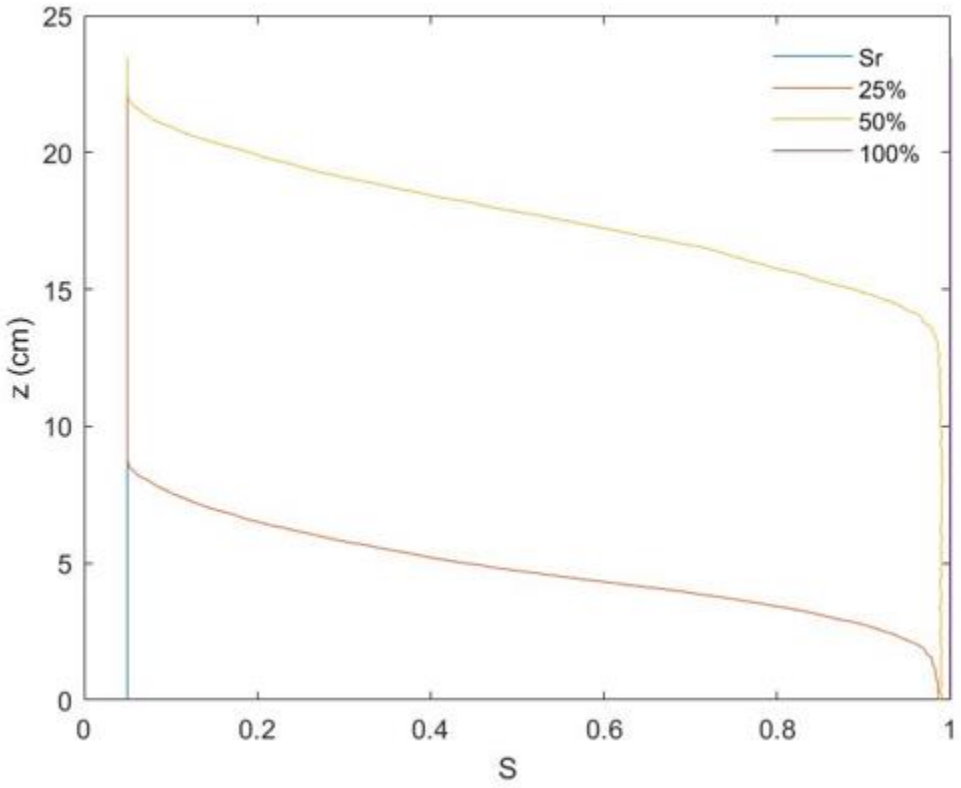

FIGURE F.6: Saturation profile versus height for test F1.

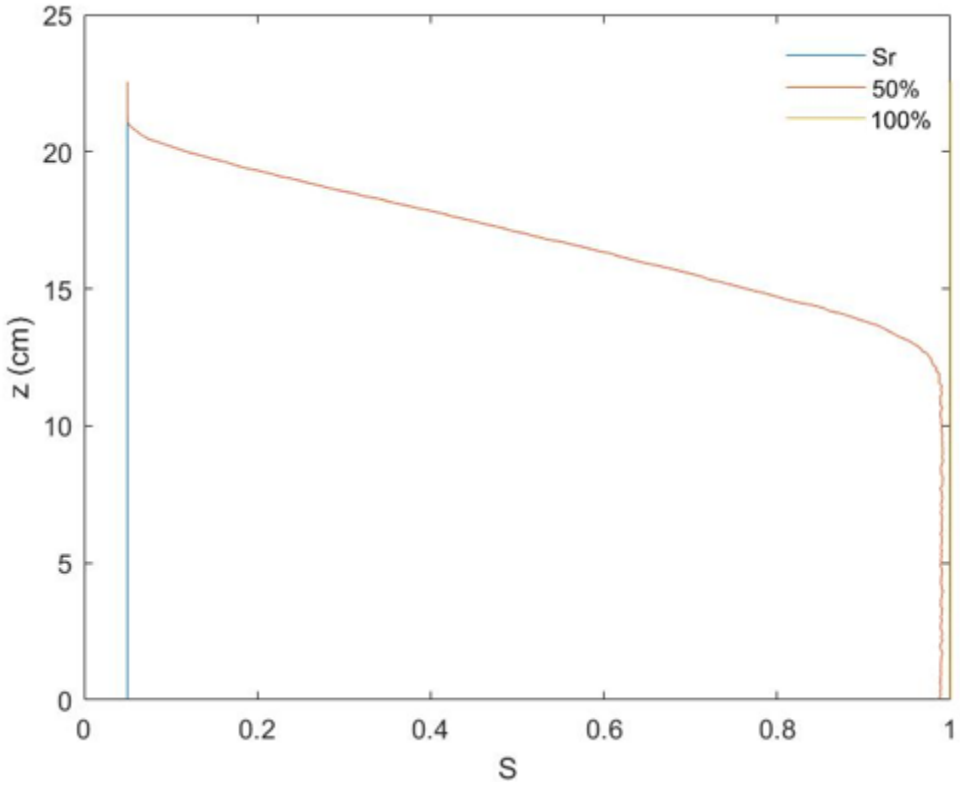

FIGURE F.7: Saturation profile versus height for test F2.

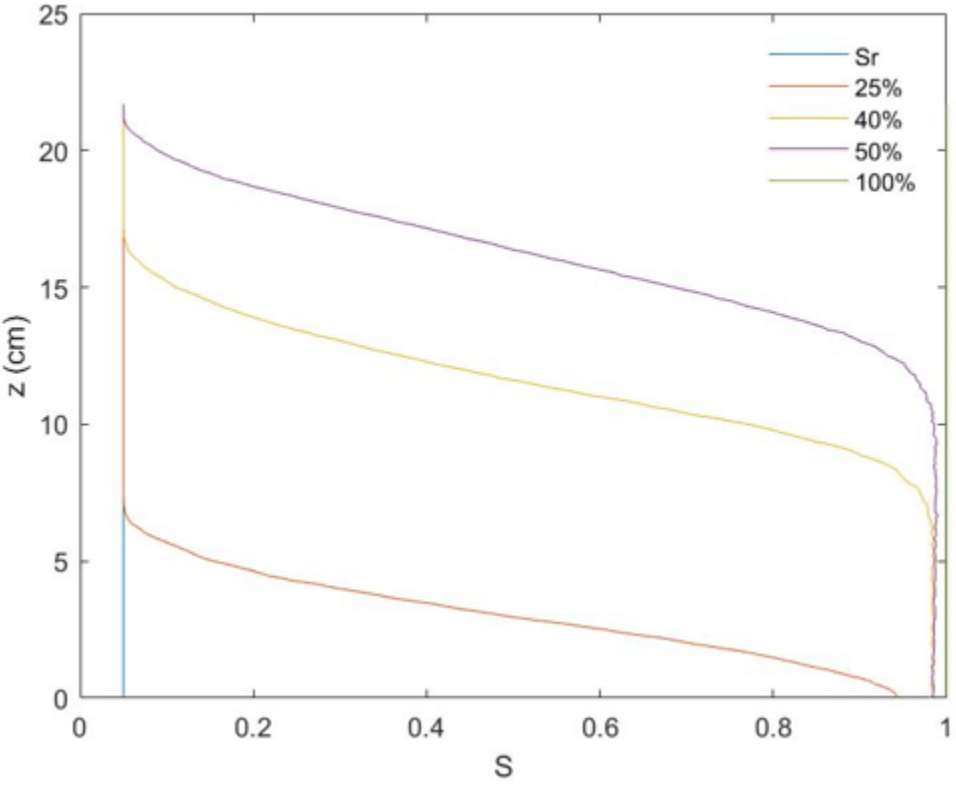

FIGURE F.8: Saturation profile versus height for test F4.

Appendix G

The LNAPL migration image sets for each test in Chapter 3 are shown in Figures G.1-6 .

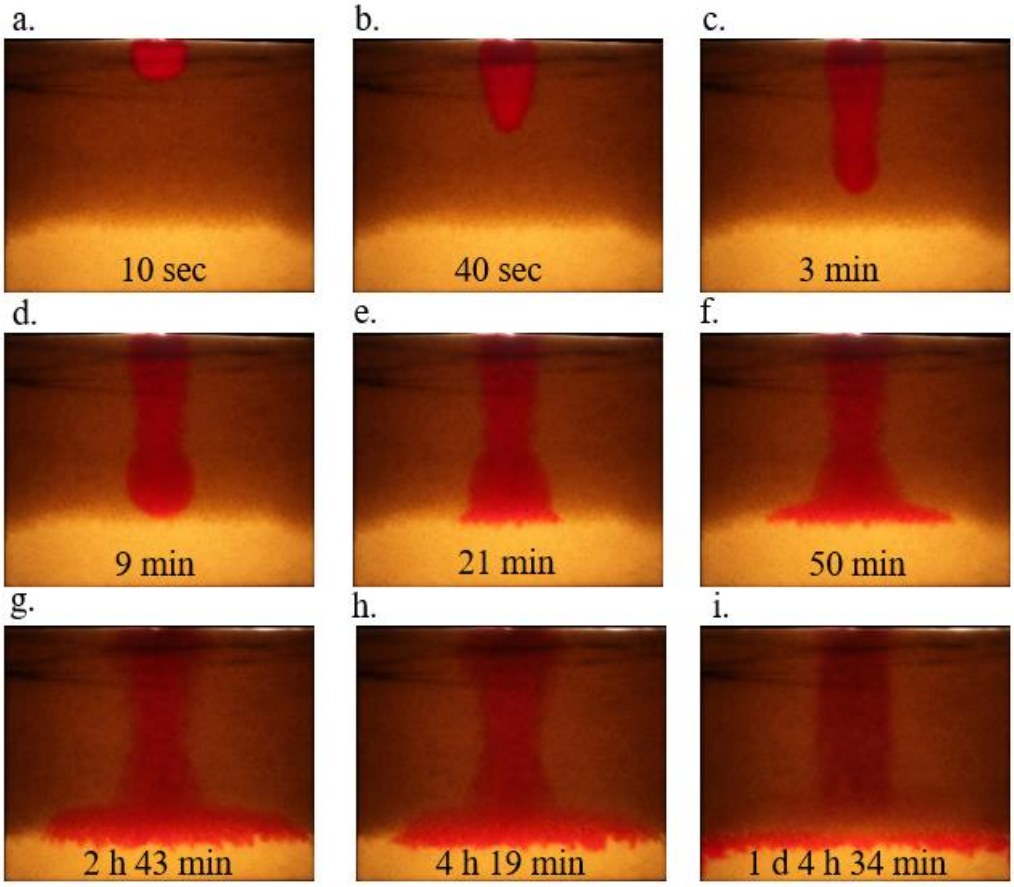

FIGURE G.1: H3040U spill progression in space at (a) 10 sec, (b) 40 sec, (c) 3 min, (d) 9 min, (e) 21 min, (f) 50 min, (g) 2 h 43 min, (h) 4 h 19 min and (i) 1 d 4 h 34 min.

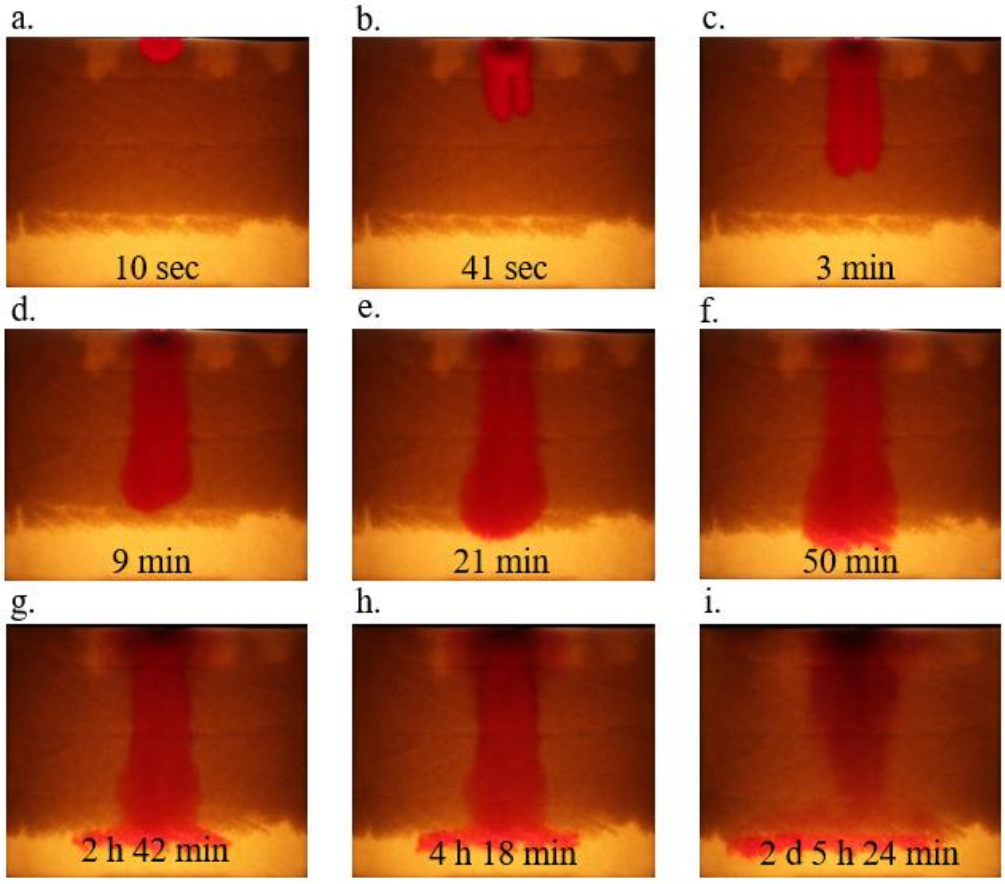

FIGURE G.2: CB3040U spill progression in space at (a) 10 sec, (b) 41 sec, (c) 3 min, (d) 9 min, (e) 21 min, (f) 50 min, (g) 2 h 42 min, (h) 4 h 18 min and (i) 2 d 5 h 24 min.

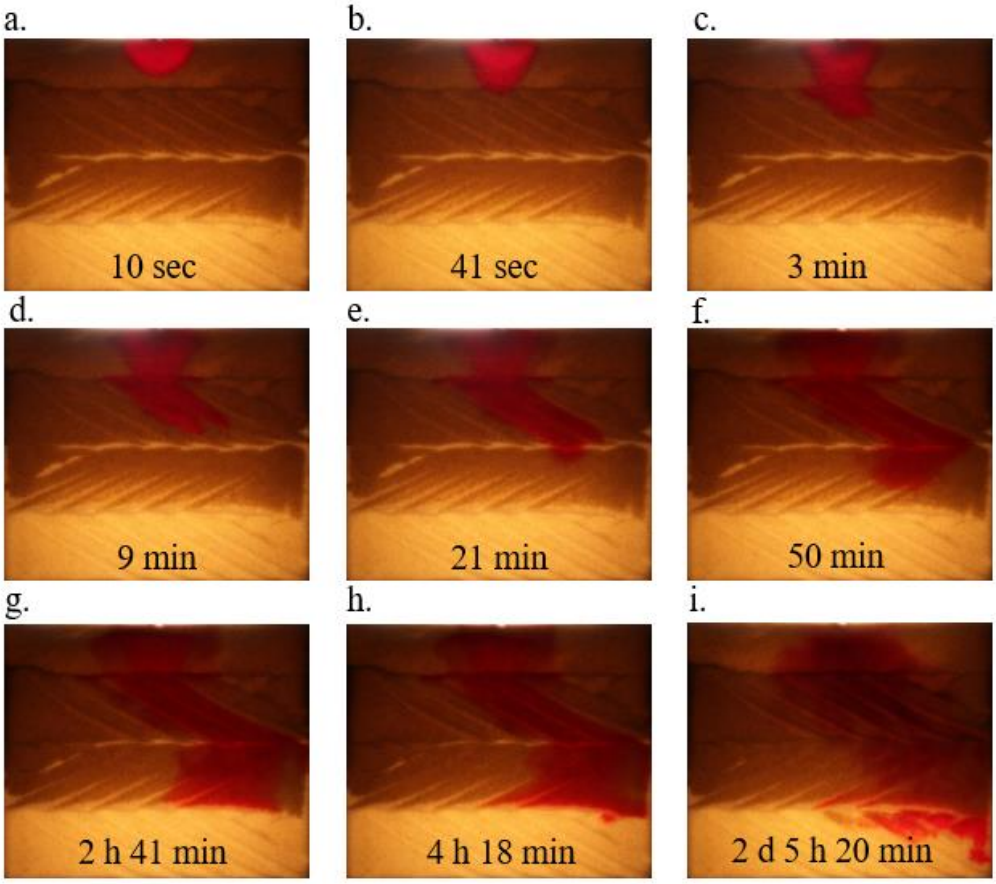

FIGURE G.3: CB4070U spill progression in space at (a) 10 sec, (b) 41 sec, (c) 3 min, (d) 9 min, (e) 21 min, (f) 50 min, (g) 2 h 41 min, (h) 4 h 18 min and (i) 2 d 5 h 20 min.

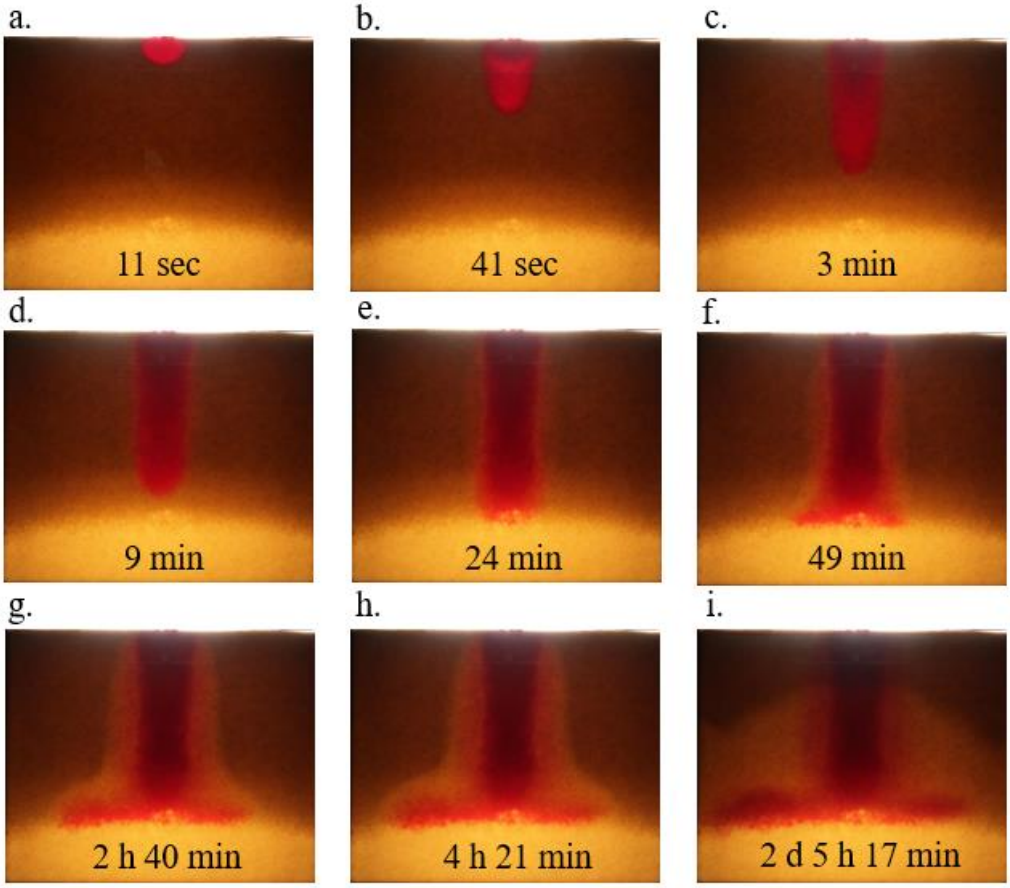

FIGURE G.4: H3040F spill progression in space at (a) 11 sec, (b) 41 sec, (c) 3 min, (d) 9 min, (e) 24 min, (f) 49 min, (g) 2 h 40 min, (h) 4 h 21 min and (i) 2 d 5 h 17 min.

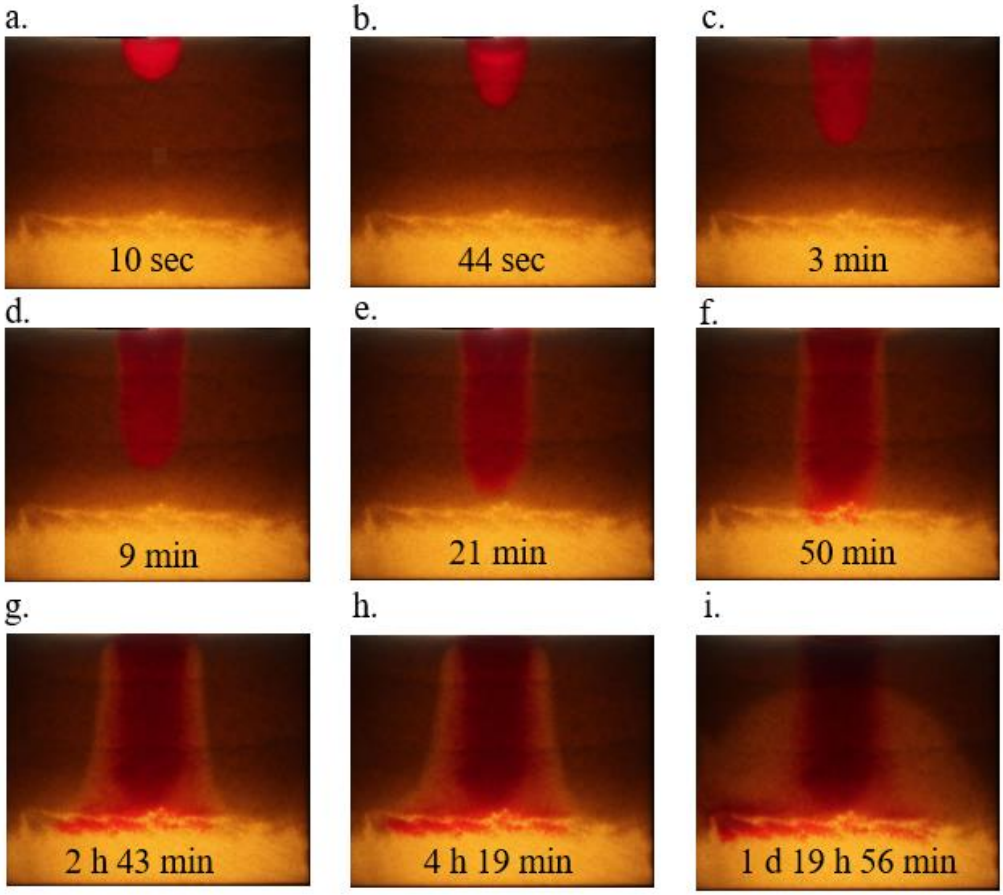

FIGURE G.5: CB3040F spill progression in space at (a) 10 sec, (b) 44 sec, (c) 3 min, (d) 9 min, (e) 21 min, (f) 50 min, (g) 2 h 43 min, (h) 4 h 19 min and (i) 1 d 19 h 56 min.

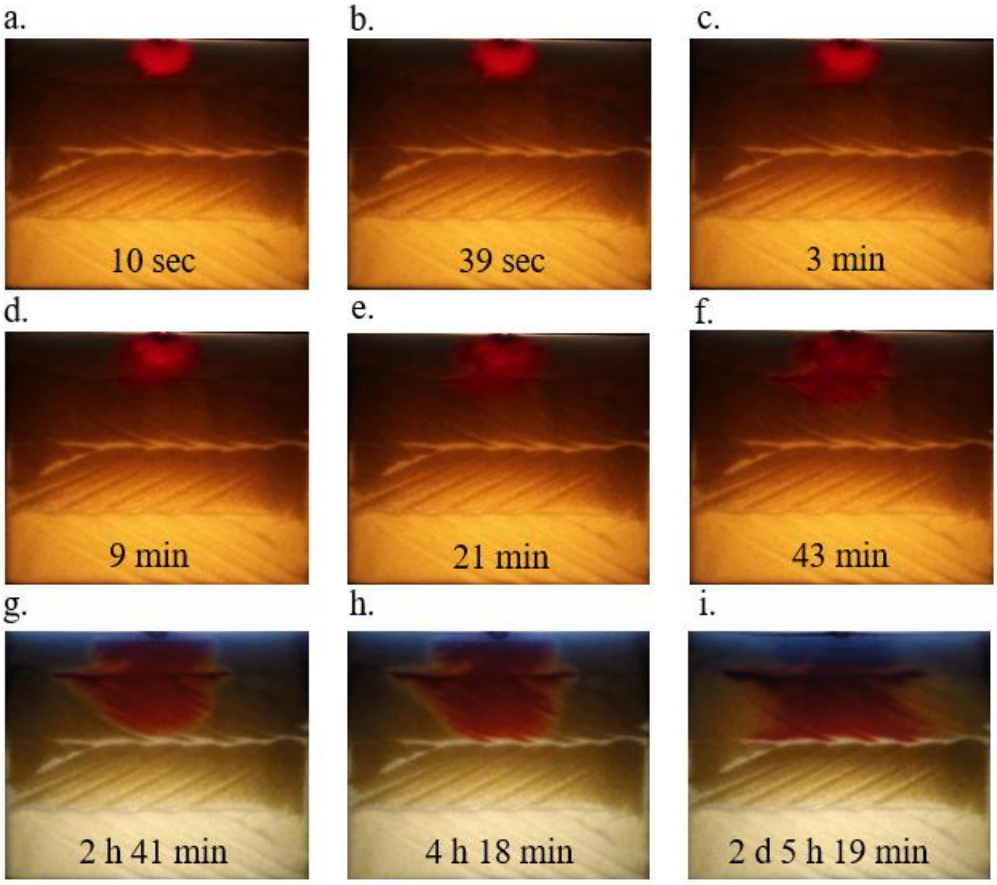

FIGURE G.6: CB4070F spill progression in space at (a) 10 sec, (b) 39 sec, (c) 3 min, (d) 9 min, (e) 21 min, (f) 43 min, (g) 2 h 41 min, (h) 4 h 18 min and (i) 2 d 5 h 19 min.

Appendix H

The halo effect that appeared in three frozen spill tests is shown in Figure H.1.

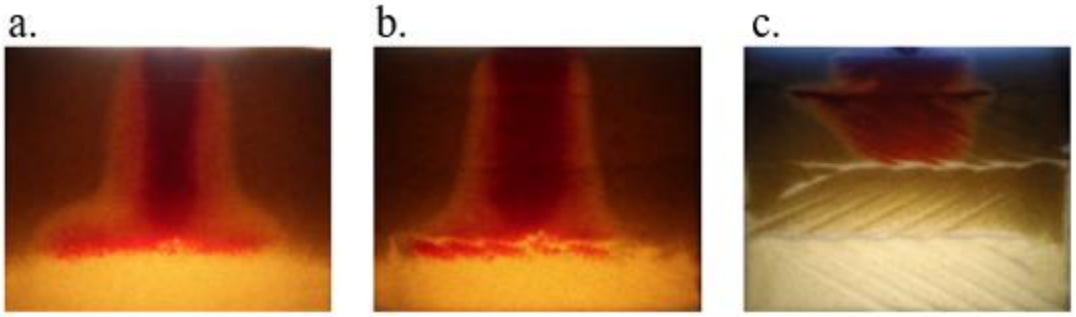

FIGURE H.1: Halo in frozen spills for packs (a) H3040F, (b) CB3040F and (c) CB4070F respectively.

Figure H.2 shows the intensity variations between the unfrozen conditions (pre-spill), frozen conditions (pre-spill), frozen conditions (during spill) and unfrozen conditions (post-spill).

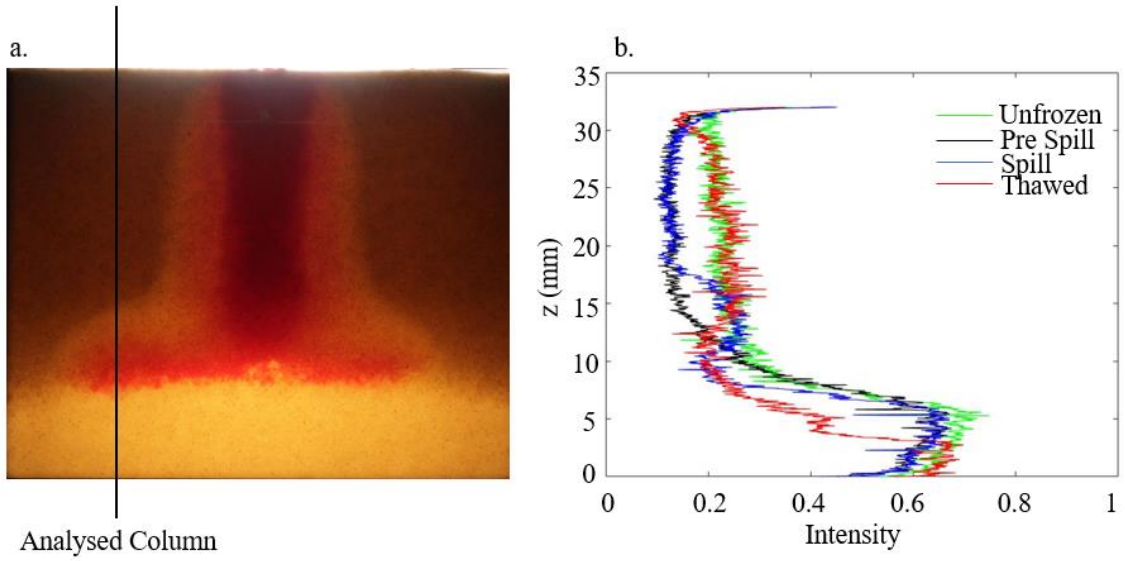

FIGURE H.2: Example of a spill image in H3040F where (a) a column was selected for an intensity analysis in (b) unfrozen conditions pre-spill, frozen conditions pre-spill, frozen conditions during the spill and in thawed conditions post spill.

Appendix I

Figure I.1 is the saturation condition before the spill for every test in Chapter 3. These images were taken before the water table was dropped to 55 mm below the cell bottom, which was the water table height prior to the test commencing.

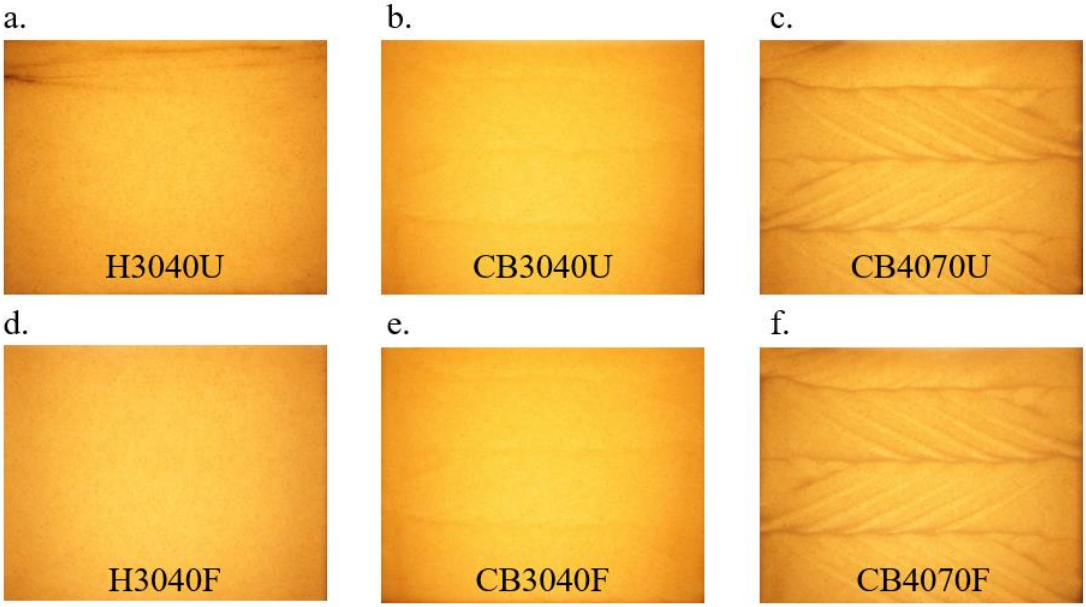

FIGURE I.1: Fully saturated packs before water drainage (pre-spill) for test in the a) H3040U, (b) CB3040U, (c) CB4070U, (d) H3040F, (e) CB3040F and (f) CB4070F pack.

Appendix J

Water imbibition after each spill in Chapter 3 is shown in Figure J.1. All LNAPL was contained in the cell during water imbibition, which means that there is about 6 g of colored heptane in each picture.

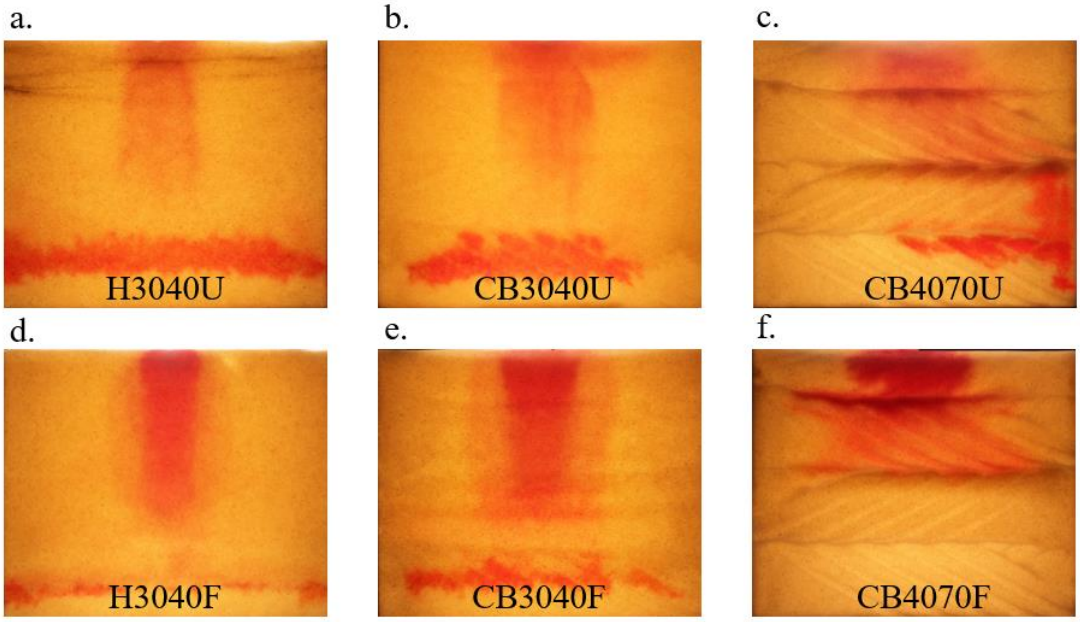

FIGURE J.1: Water imbibition post spills in the a) H3040U, (b) CB3040U, (c) CB4070U, (d) H3040F, (e) CB3040F and (f) CB4070F pack.

Appendix K

Figure K.1-3 shows cell locations in macro view for 3 tests, highlighting the different degrees of heterogeneity.

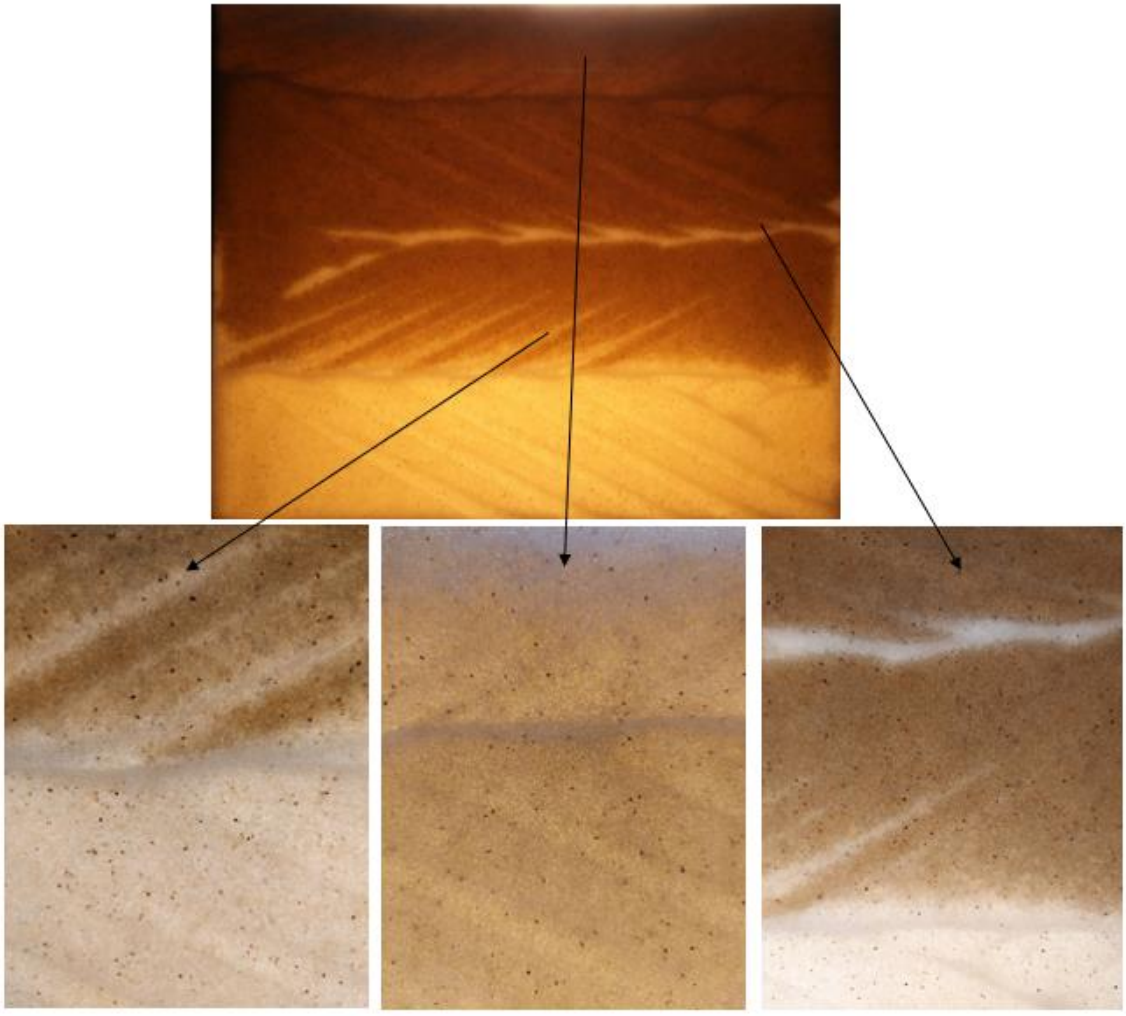

FIGURE K.1: Macro pictures showing various zones with different degrees of heterogeneity in grain size and water content.

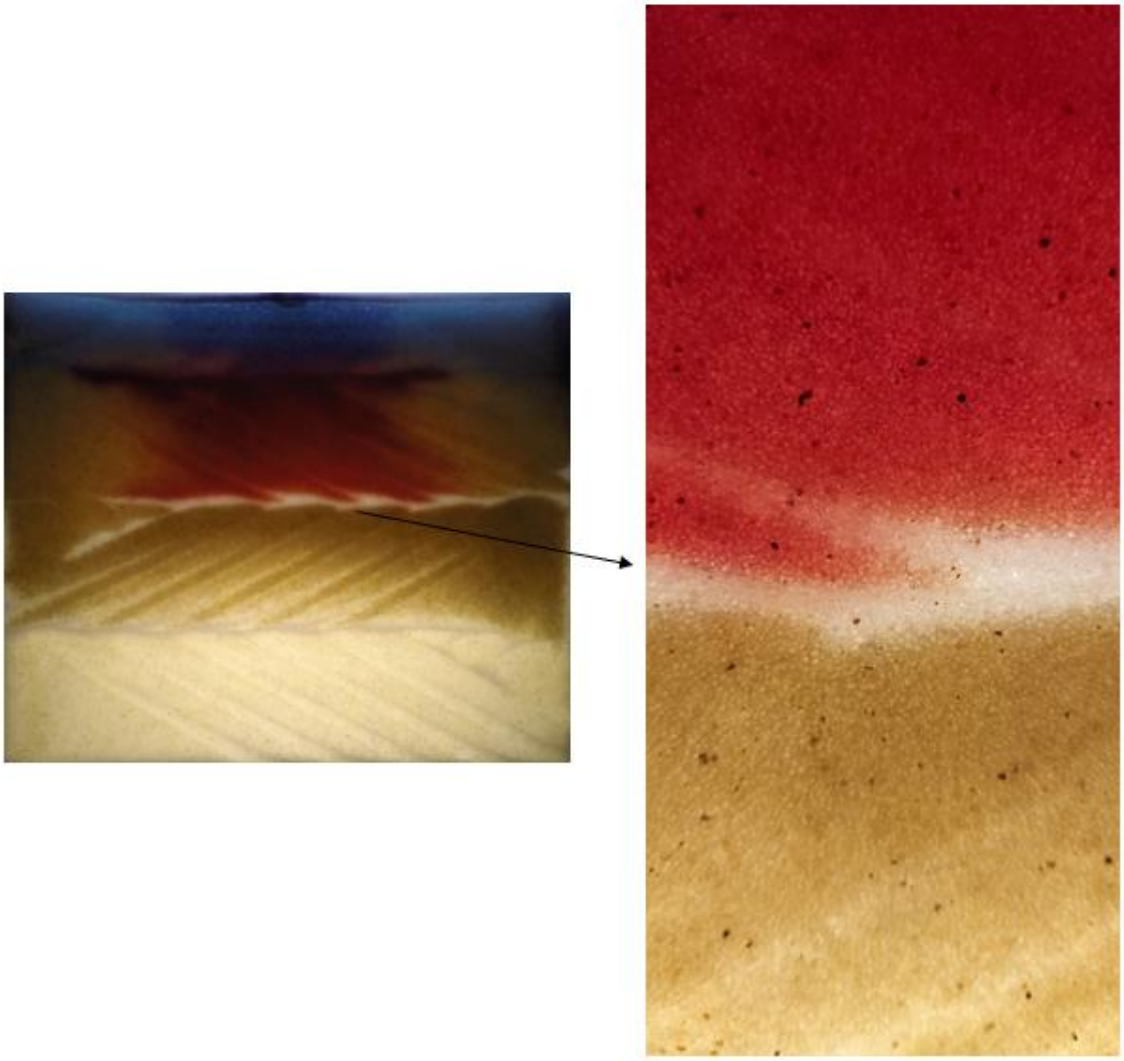

FIGURE K.2: Macro picture of LNAPL spill in CB4070F.

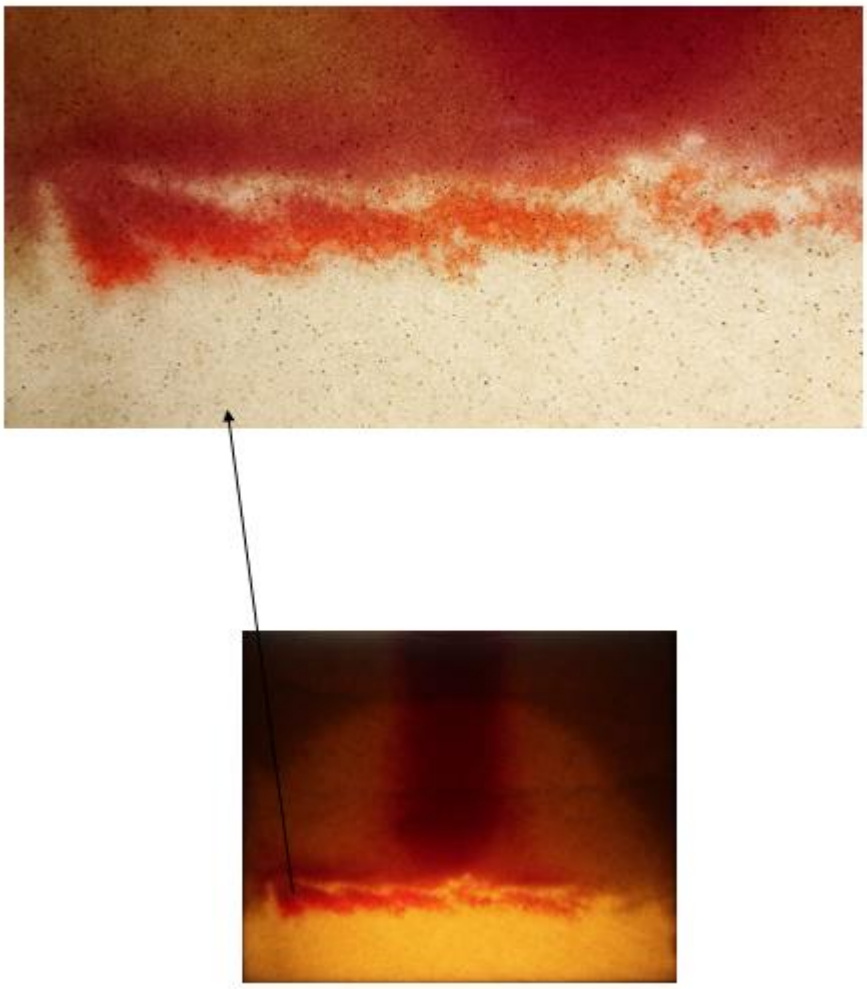

FIGURE K.3: Macro pictures showing LNAPL spill in CB3040F.

Appendix L

Figures L.1-4 are images of the experimental set-up and the equipment.

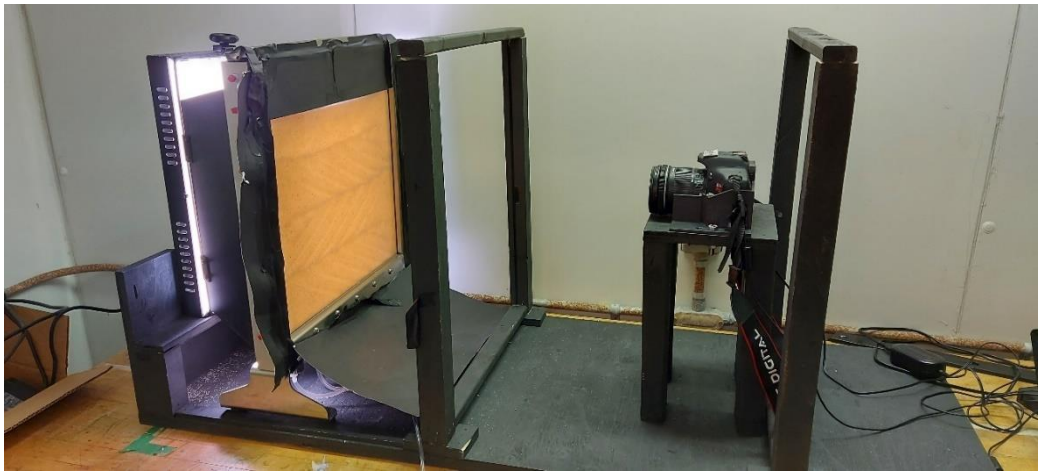

FIGURE L.1: Experimental set-up outside the freezer without the covering curtains.

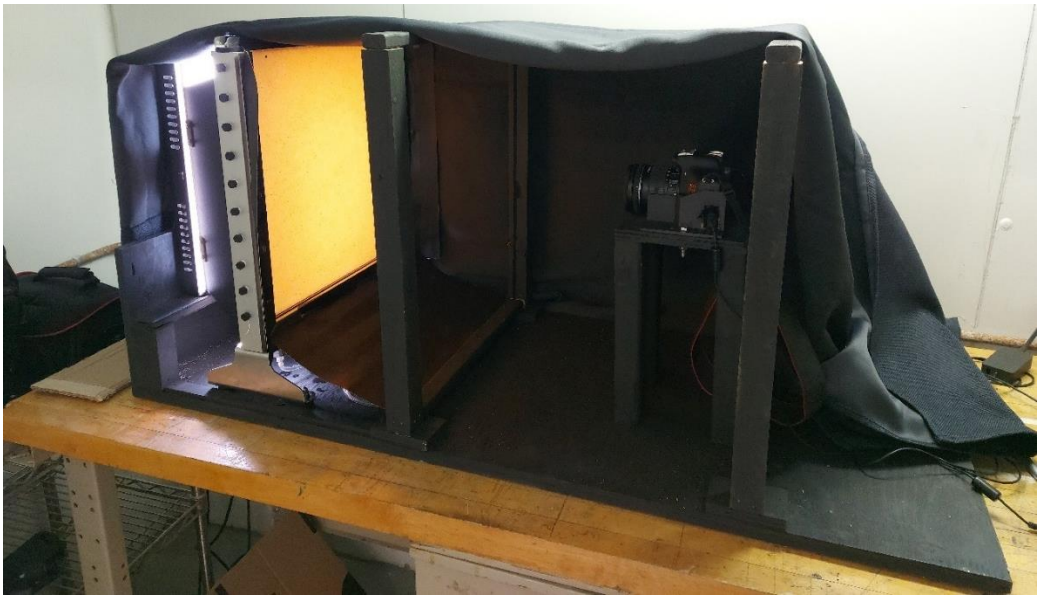

FIGURE L.2: Experimental set-up placed outside of the freezer with the covering curtains.

FIGURE L.3: Experimental set-up placed inside the freezer.

FIGURE L.4: Freezer used for the experiments.